FINAL TECHNICAL REPORT

Award #06HQGR0132

BROADBAND GROUND MOTION SIMULATIONS FOR THE SAN FRANCISCO BAY REGION

Robert Graves
URS Group Inc.
566 El Dorado Street, 2nd Floor
Pasadena, CA 91101

Tel: 626-449-7650
Fax: 626-449-3536
Email: Robert_graves@urscorp.com

FINAL TECHNICAL REPORT

Award #06HQGR0132

BROADBAND GROUND MOTION SIMULATIONS FOR THE SAN FRANCISCO BAY REGION

Robert Graves
URS Group Inc.
566 El Dorado Street, 2nd Floor
Pasadena, CA 91101

Tel: 626-449-7650
Fax: 626-449-3536
Email: Robert_graves@urscorp.com

Abstract

The 2002 Working Group on California Earthquake Probabilities has recently determined there is a 62% probability of a M_w 6.7 or greater earthquake occurring in the greater San Francisco Bay region during the 30 year period 2002-2031. Of the main faults in this region, the Hayward-Rogers Creek system (27%) and the San Andreas fault (21%) have the highest individual probabilities. These faults are predominantly strike-slip and run through or adjacent to the major urban areas of the San Francisco Bay region.

Currently, the 1989 M_w 6.9 Loma Prieta earthquake provides the most relevant insight into the types of ground motion effects that may be expected in the San Francisco Bay region during rupture of these other faults. These effects include strong rupture directivity, trapping and amplification of basin waves, and amplification due to critical Moho reflections. However, rupture during the Loma Prieta earthquake was confined primarily to depths greater than about 5-10 km, and thus, this event may have different ground motion characteristics than those expected for surface rupturing faults. In particular Kagawa et al. (2004) have shown that ground motions from surface rupturing earthquakes, on average, are about 30% lower than those observed for buried ruptures at periods between 0.3 to 3 seconds.

The objective of this project is to provide quantitative estimates of the ground motions expected from large earthquakes on the major strike-slip faults of the San Francisco Bay region. Using broadband ground motion simulation procedures, we will quantify the ground motions that could be generated by different earthquake scenarios occurring on these faults, taking account of several important ground motion features. These include the effects of forward rupture directivity, which will be strongly dependent on epicenter location; the effects of basin trapped waves, which may have a significant impact on motions in the Santa Clara Valley; and the characteristics of ground motions from shallow rupture, which appear to be weaker than those of buried faulting events.

We have extensive experience in the characterization and modeling of these effects in past earthquakes. This includes the analysis of rupture directivity effects from numerous earthquakes and the development of an empirical model of these effects. We have performed detailed

analyses of the strong motion records from shallow and buried rupturing events and have documented the differences in ground motions between these classes of earthquakes. We have also studied rupture characteristics of shallow and buried faults using both theoretical analyses and by examining published rupture models of past earthquakes. These studies suggest that the observed ground motion differences are related to lower slip velocities on shallow fault ruptures compared to those inferred for deeper fault ruptures.

Furthermore, we have recently developed an enhanced broadband time history simulation procedure that combines deterministic aspects at low frequencies ($f < 1$ Hz) with stochastic aspects at high frequencies ($f > 1$ Hz) (Graves and Pitarka, 2004). The method uses a kinematic description of fault rupture, incorporating spatial heterogeneity in slip and rupture velocity by discretizing an extended finite-fault into a number of smaller subfaults. Differences in slip velocity between deep and shallow portions of the rupture are explicitly included in the parameterization. The stochastic approach sums the response for each subfault assuming a random phase, an omega-squared source spectrum and generic ray-path Green' functions (extension of Boore, 1983). We use the convolution operator of Frankel (1995) to ensure that the stochastic summation is not dependent on the choice of subfault dimensions. The deterministic approach sums the response for many point sources distributed across each subfault. Wave propagation at frequencies below 1 Hz is modeled using a 3D viscoelastic finite difference algorithm. This methodology has been successfully tested through the modeling of ground motion data from a number of recent earthquakes including the 1989 Loma Prieta earthquake, giving us confidence in the predictive capabilities of this approach in the San Francisco Bay region.

Our project compliments USGS efforts to estimate the ground motions that might occur for a repeat of the 1906 San Francisco earthquake. Mary Lou Zoback, Tom Brocher and Brad Aagaard of the Menlo Park USGS office coordinated these efforts, which involve construction of a 3D velocity model for northern California, testing of the model using observation from the 1989 Loma Prieta earthquake, and characterization of 1906 rupture scenarios and ground motions.

Products for Earthquake Loss Reduction

The goal of our project is to use rigorous seismological modeling of broadband strong ground motions for scenario ruptures of the San Andreas fault in the San Francisco Bay region to help assess and quantify the expected ground shaking hazard for such events. Direct products for earthquake loss reduction in northern California from this work include:

- Scenario maps of ground motions from large earthquakes in the San Francisco Bay region for use in emergency planning and loss estimation.
- Broadband ground motion time histories and response spectra from large earthquakes in the San Francisco Bay region for use in the design and retrofit of structures.

All of the broadband time histories and maps generated in this project will be archived and made freely available to other researchers and investigators.

Publications

The work performed during this project has been published in 2 papers in the Bulletin of the Seismological Society of America:

Aagaard, B. T., T. M. Brocher, D. Dolenc, D. Dreger, R. W. Graves, S. Harmsen, S. Hartzell, S. Larsen, and M. L. Zoback (2008). Ground-motion modeling of the 1906 San Francisco earthquake, Part I: validation using the 1989 Loma Prieta earthquake, *Bull. Seism. Soc. Am.*, 98, 989-1011.

Aagaard, B. T., T. M. Brocher, D. Dolenc, D. Dreger, R. W. Graves, S. Harmsen, S. Hartzell, S. Larsen, Kathleen McCandless, Stefan Nilsson, N. Anders Petersson, Arthur Rodgers, Björn Sjögreen, and M. L. Zoback (2008). Ground-motion modeling of the 1906 San Francisco earthquake, Part II: Ground-Motion Estimates for the 1906 Earthquake and Scenario Events, *Bull. Seism. Soc. Am.*, 98, 1012-1046.

Copies of these papers are appended to this final report.

Bulletin of the Seismological Society of America, Vol. 98, No. 2, pp. 989–1011, April 2008, doi: 10.1785/0120060409

Ⓔ

Ground-Motion Modeling of the 1906 San Francisco Earthquake, Part I: Validation Using the 1989 Loma Prieta Earthquake

by Brad T. Aagaard, Thomas M. Brocher, David Dolenc,* Douglas Dreger, Robert W. Graves, Stephen Harmsen, Stephen Hartzell, Shawn Larsen, and Mary Lou Zoback

Abstract We compute ground motions for the Beroza (1991) and Wald *et al.* (1991) source models of the 1989 magnitude 6.9 Loma Prieta earthquake using four different wave-propagation codes and recently developed 3D geologic and seismic velocity models. In preparation for modeling the 1906 San Francisco earthquake, we use this well-recorded earthquake to characterize how well our ground-motion simulations reproduce the observed shaking intensities and amplitude and durations of recorded motions throughout the San Francisco Bay Area. All of the simulations generate ground motions consistent with the large-scale spatial variations in shaking associated with rupture directivity and the geologic structure. We attribute the small variations among the synthetics to the minimum shear-wave speed permitted in the simulations and how they accommodate topography. Our long-period simulations, on average, under predict shaking intensities by about one-half modified Mercalli intensity (MMI) units (25%–35% in peak velocity), while our broadband simulations, on average, under predict the shaking intensities by one-fourth MMI units (16% in peak velocity). Discrepancies with observations arise due to errors in the source models and geologic structure. The consistency in the synthetic waveforms across the wave-propagation codes for a given source model suggests the uncertainty in the source parameters tends to exceed the uncertainty in the seismic velocity structure. In agreement with earlier studies, we find that a source model with slip more evenly distributed northwest and southeast of the hypocenter would be preferable to both the Beroza and Wald source models. Although the new 3D seismic velocity model improves upon previous velocity models, we identify two areas needing improvement. Nevertheless, we find that the seismic velocity model and the wave-propagation codes are suitable for modeling the 1906 earthquake and scenario events in the San Francisco Bay Area.

Online Material: Modified Mercalli intensities and velocity waveforms, and a movie of simulated wave propagation.

Introduction

The centennial of the 18 April 1906 magnitude 7.9 San Francisco, California, earthquake inspired a 2-yr collaborative effort to estimate the strong ground motions produced by the event using up-to-date information and constraints with modern computational tools (see Aagaard *et al.* (2008)). Before attempting to model the 1906 earthquake, we first modeled the 17 October 1989 magnitude 6.9 Loma Prieta earthquake in order to gauge the accuracy of modeling strong ground motions in the San Francisco Bay Area. The Loma Prieta earthquake was the largest earthquake in the San Francisco Bay Area since the 1906 earthquake and was well recorded throughout the region on modern seismic instruments (see, e.g., U.S. Geological Survey Staff, 1990; Bakun and Prescott, 1994; Holzer, 1994).

The Loma Prieta earthquake ruptured a fault segment in the Santa Cruz Mountains about 40-km long and ranging in 1 depth from 7 to 20 km, with a maximum slip of about 5 m (Beroza, 1991; Wald *et al.*, 1991). The earthquake generated modified Mercalli intensities (MMI) of VI or more over much of the southern San Francisco Bay Area (Fig. 1). Total losses to buildings, lifelines, highways, and other structures were

*Present address: Large Lakes Observatory, University of Minnesota, Duluth 109 RLB, 2205 E. 5th Street, Duluth, Minnesota 55812.

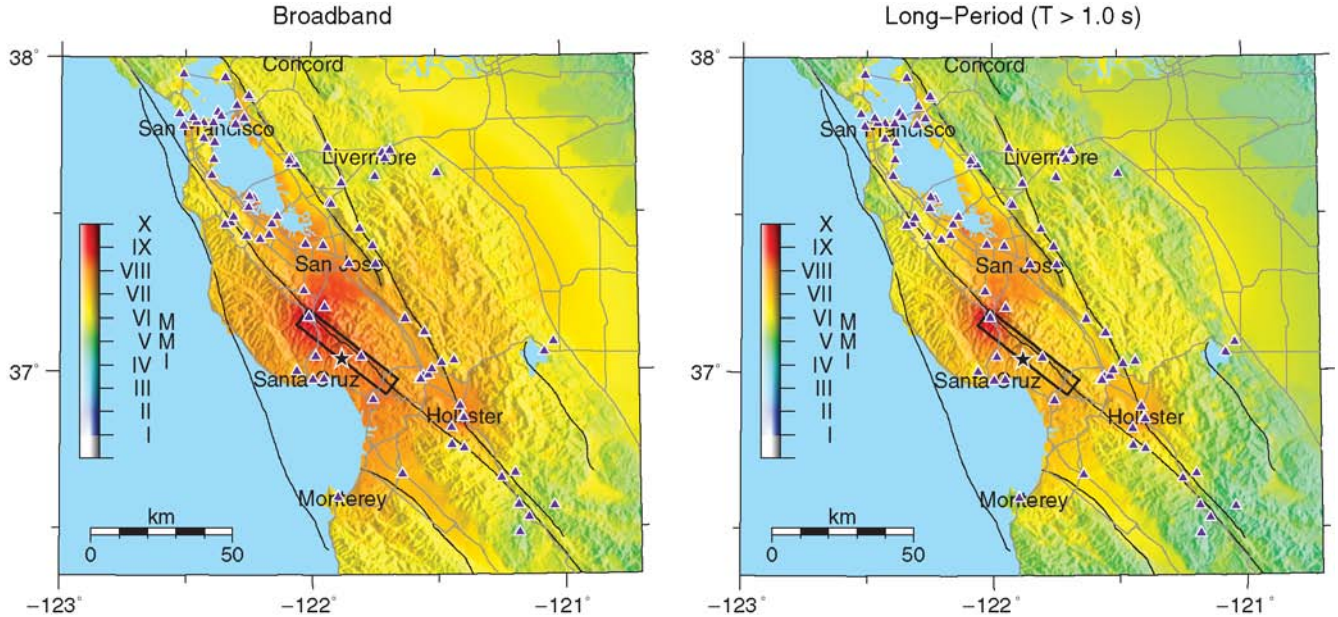

Figure 1. Broadband (left) and long-period (right) instrumental ShakeMaps for the 1989 Loma Prieta earthquake. The star identifies the epicenter, the thick black lines delineate the projection of the fault plane in the Wald source model, and the triangles show locations of the stations used in the construction of the ShakeMap. We constructed the long-period ($T > 1.0$ sec) ShakeMap to be compatible with our long-period simulations (see text).

approximately $6 billion in 1989 dollars (U.S. Geological Survey Staff, 1990). The collapse of the upper story of the Cypress freeway in Oakland caused 42 of the 63 fatalities associated with the earthquake. Thinning of the crust to the north and a large amplitude reflection from the Moho were proposed to explain the amplified seismic arrivals in San Francisco and Oakland (Somerville and Yoshimura, 1990; Campbell, 1991; Catchings and Kohler, 1996).

Several previous studies have examined the strong ground motions in the Loma Prieta earthquake using 3D numerical models (e.g., Frankel and Vidale, 1992; Stidham *et al.*, 1999; Hartzell *et al.*, 2006). Unfortunately, the geologic and seismic velocity models used in these studies were either limited in extent (e.g., the Santa Clara Valley models used by Frankel and Vidale [1992] and Hartzell *et al.* [2006]) or had limited detail and resolution over much of the study area (e.g., the simple polygon based model used by Stidham *et al.* [1999]). The importance of geologic structure in determining spatial variations in shaking was recognized following the 1906 earthquake (Lawson, 1908) and has been an area of active research for much of the last 50 yr. Significant progress in modeling wave propagation through complex 3D geologic structure has accelerated in the last decade following the construction of new 3D seismic velocity models such as the Southern California Earthquake Center community velocity model (Magistrale *et al.*, 1996). That model has been used in numerous studies exploring wave propagation and variations in the duration and amplitude of shaking in and around the Los Angeles, San Bernadino, and San Fernando basins. For example, Olsen and Archuleta (1996) demonstrated that for magnitude 6.7 events on a few different faults in the Los Angeles area, in addition to strong shaking in the epicentral area, the largest peak velocities tended to occur over the deepest parts of the Los Angeles basin and near the steepest edges of the basin. Wald and Graves (1998) evaluated ground-motions estimates for the 1992 magnitude 7.3 Landers earthquake using three different 3D velocity models (Graves, 1996a; Magistrale *et al.*, 1996; Hauksson and Haase, 1997) and found that although all of the models reproduced the general characteristics of the motions, the fit was sensitive to the geometry of the basin structures and the seismic velocities of the basin fill.

In contrast to the Los Angeles area, which is dominated by large, deep sedimentary basins, the San Francisco Bay region contains many small, relatively shallow sedimentary basins, such as the Cupertino basin southwest of San Jose, the Evergreen basin east of San Jose, the Cotati and Windsor basins underneath Santa Rosa, the basin under San Pablo Bay, the San Leandro basin south of Oakland, and the Livermore basin (California Division of Oil and Gas, 1982; Stanley, 1985; McCulloch, 1987; Meltzer *et al.*, 1987; Wentworth *et al.*, 1995; Parsons *et al.*, 2003; Catchings *et al.*, 2004; Brocher, 2005b; Catchings *et al.*, 2006; McPhee *et al.*, 2007). Figure 2 shows the locations of the basins. Jachens *et al.* (2006) assembled a variety of datasets to construct a comprehensive 3D geologic model that includes these structures. Based on this geologic model and regression relations between material properties and lithology and depth (Brocher, 2005a; Brocher, 2008), the U.S. Geological Survey generated a 3D seismic velocity model, U.S. Geological Survey

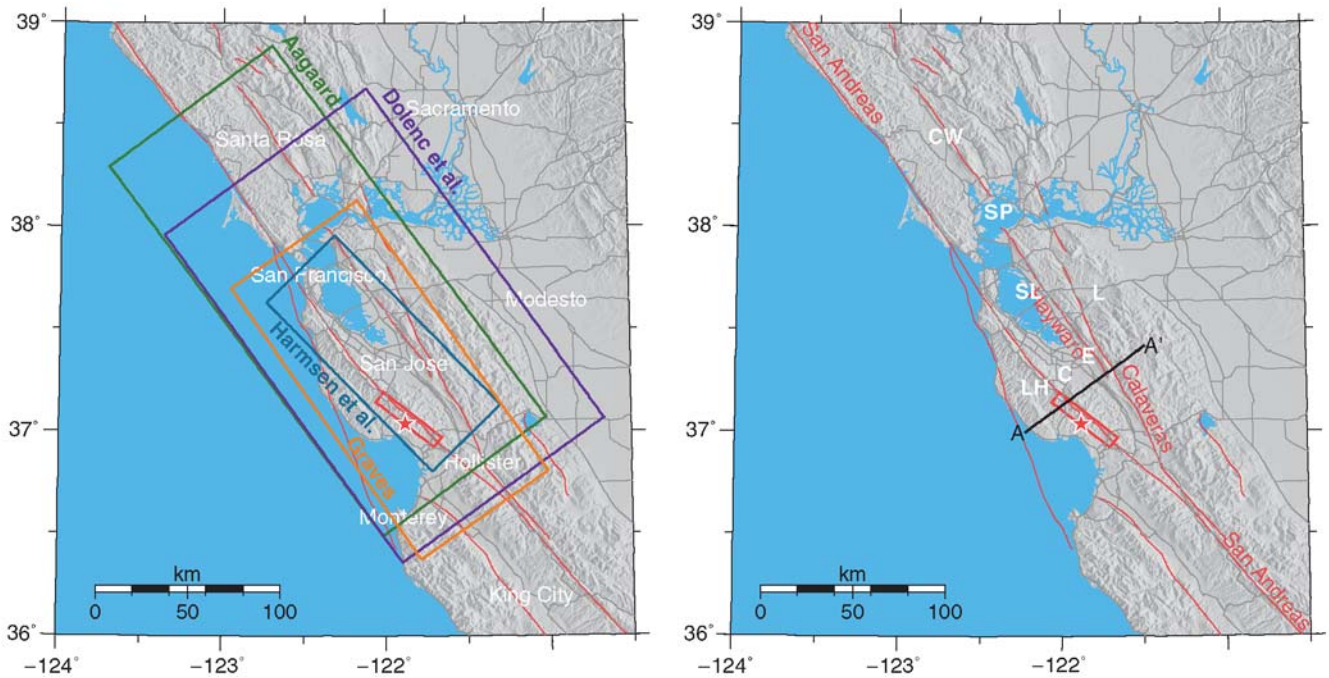

Figure 2. Bounding boxes of the domains used by the four ground-motion modeling groups (left) and the locations of the major sedimentary basins (right). The thick red line shows the projection of the fault plane in the Wald source model, the white star identifies the epicenter, and the thin red lines delineate the surface traces of the major faults in the region. The basin abbreviations are Cupertino Basin, C; Cotati and Windsor Basins, CW; Evergreen Basin, E; Livermore Basin, L; La Honda Basin, LH; San Leandro Basin, SL; San Pablo Bay, SP. Figure 4 shows the shear-wave speed on cross section *AA′*.

(USGS) Bay Area Velocity Model 05.1.0 (Brocher *et al.*, 2006), with significantly more detail than any of the previous models covering the San Francisco Bay Area for use in this and other future studies. As a result, we expect to capture the effects of these complex 3D basin structures on strong ground motions. Furthermore, modeling the ground motions from the Loma Prieta earthquake serves as a test of the geologic and seismic velocity models by identifying areas where the models provide reasonable fits to the observations, areas where the models need improvement, and what features in the models appear to have the strongest affect on the spatial distribution of the shaking.

Methodology

The ground-motion simulations use two different kinematic source models and four different wave-propagation codes, yielding a total of eight realizations of the ground motions for the Loma Prieta earthquake. All four wave-propagation codes use the same kinematic source parameters (distribution of slip, slip time history, and rise time). By comparing the motions computed from each of the codes with recorded motions, we are able to assess how well we can reproduce the recorded shaking relative to the uncertainty in the earthquake source. Similarly, the four different wave-propagation codes allow examination of the relative accuracy and the importance of features included or excluded in the simulations relative to the uncertainty in the seismic source. Ideally, all four wave-propagation codes should produce equivalent waveforms for the same source model, allowing us to clearly differentiate the waveforms from the two source models.

Source Models

We selected two kinematic source models, which we will refer to as the Beroza model (Beroza, 1991) and the Wald model (Wald *et al.*, 1991). These two models employ significantly different representations of the source (see Fig. 3) and are based on slightly different datasets. The Beroza model represents the seismic source using a spatially continuous slip field and is constrained by local stations with relatively few stations northwest of the epicenter, whereas the Wald model represents the seismic source using a piecewise uniform slip field and is constrained by both teleseismic and local stations with slightly more uniform azimuthal coverage. Both models approximate the rupture surface using a single plane dipping at 70° to the southwest; the planes strike 130° and 128° east of north in the Beroza and Wald models, respectively. Northwest and updip from the hypocenter, both models have an area with large slip; southeast and updip from the hypocenter, however, slip in the Beroza model is significantly larger than that in the Wald model. The rupture

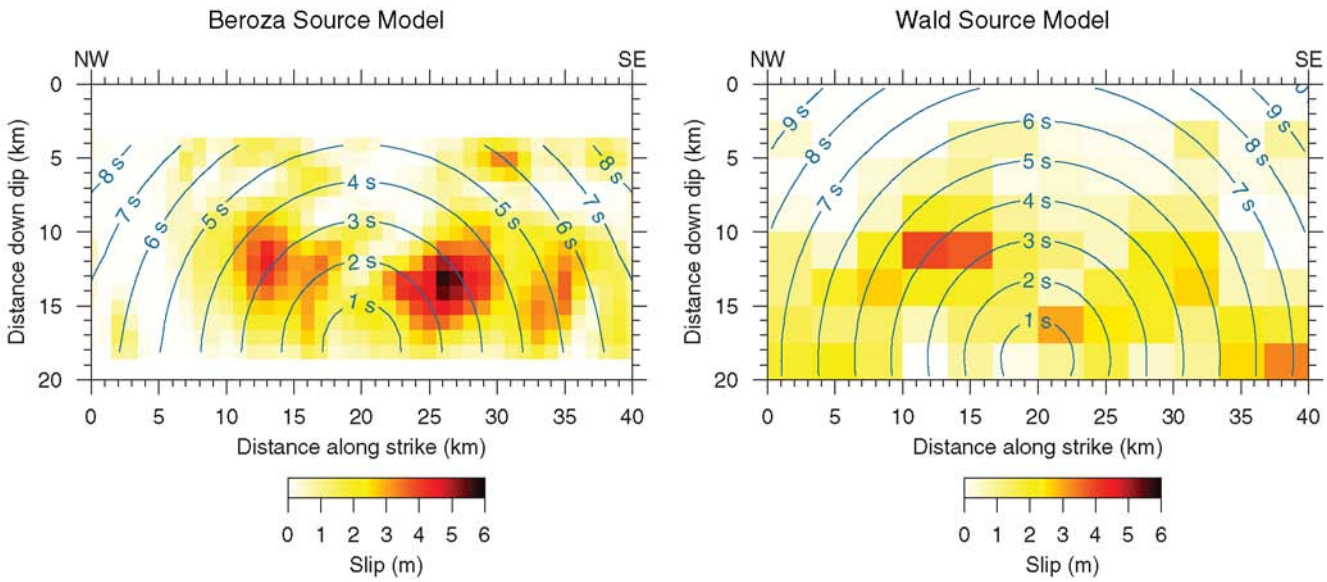

Figure 3. Slip (shading) and slip initiation time (contours) for the Beroza (left) and Wald (right) source models. The downdip coordinates of the Beroza source have been aligned with those of the Wald source model. Both source models have a region of large slip northwest of the hypocenter, but the Beroza source model contains greater slip than the Wald model southeast of the hypocenter.

speeds imposed in the models are quite similar; in the Beroza model, the rupture is 80% of the local shear-wave speed, and in the Wald model, the rupture speed is 2.7 km/sec (which is about 75% of the rupture speed in the primary source regions).

We adopted the Wald source model with two minor modifications. First, as suggested by Hartzell *et al.* (2006), we reduce the slip on the northwestern asperity by 1 m and increase the slip on the southeastern asperity by 1 m, making the two regions of high slip more equal in moment release. Hartzell *et al.* (2006) found that this slip distribution gave a better fit to station LEX when using a 3D velocity model. Liu and Archuleta (2004), in comparing source inversions based on 1D and 3D velocity models, reached a similar conclusion. Second, for the slip time function, we use the integral of Brune's far-field time function (Brune, 1970):

$$D(t) = D_{\text{final}}\left[1 - e^{-t/t_0}\left(1 + \frac{t}{t_0}\right)\right], \tag{1}$$

$$t_0 = \frac{D_{\text{final}}}{eV_{\max}}, \tag{2}$$

$$V_{\max}[m/s] = 1.5\sqrt{D_{\text{final}}[m]}, \tag{3}$$

where $D(t)$ is the slip as a function of time, D_{final} is the final slip at a point, t_0 is a time constant, and $V_{\max}$ is the peak slip rate. We chose this slip time function because we use it in our modeling of the 1906 earthquake (a case in which source inversions cannot constrain the slip time function), and its asymmetric shape is compatible with slip time histories produced by spontaneous rupture models with slip-weakening friction (Piatanesi *et al.*, 2004). Adopting this slip time history with a uniform rupture speed means we do not have the local variations in rupture speed that are permitted in the inversion, which uses multiple time windows.

The rise time (the time it takes for 95% of the slip to occur, t_{95}), which is given by

$$t_{95} = 1.745\frac{D_{\text{final}}}{V_{\max}}, \tag{4}$$

where

$$D(t_{95}) = 0.95D_{\text{final}} \tag{5}$$

is in the range of 1–2 sec for slip in the range of 1–3 m, which closely follows the rise times in the original Beroza and Wald models. Varying the peak slip rate with the square root of the final slip (equation 3) blends two common approaches for dealing with inadequate constraints on slip rise time and peak slip rate. The most common approach assumes a uniform rise time in a given event with the value based on an empirical relationship, such as the one developed by Somerville *et al.* (1999). In this approach, the rise time usually depends on the magnitude of the event, and peak slip rates within an event are proportional to slip. This implies that the rise time at each location depends on the final size of the event. A second approach assumes a uniform peak slip rate, which gives rise times within an event that are proportional to slip (Aagaard

et al., 2001; Aagaard *et al.*, 2004; Aagaard and Heaton, 2004). In this approach, rise time only depends on the local slip and is independent of the size of the event. Clearly, across a spectrum of event sizes, rise times should exhibit features present in both approaches. Our approach of varying the peak slip rate (rise time) with the square root of the final slip maintains a rise time independent of event size (as in the second approach) while incorporating a correlation between peak slip rate and slip (as in the first approach).

These small changes to the source models mean the ground motions in our simulations will not match those generated in the source inversion. In addition, we generate ground motions using the recently developed USGS Bay Area velocity model, not the simple velocity models employed in the inversions. However, we will find that these small adjustments do not appear to compromise our ability to match the observed shaking intensities and velocity waveforms.

Wave-Propagation Codes

Four simulation groups, (1) Aagaard, (2) Dolenc *et al.* (consisting of Dolenc, Dreger, and Larsen), (3) Graves, and (4) Harmsen, *et al.* (consisting of Harmsen and Hartzell), participated in the modeling effort, each with a different wave-propagation code. All of the codes solve the elastic wave equation in 3D heterogeneous media, and Table 1 summarizes their major features. Each group selected a domain (see Fig. 2) based on the computational resources available to it, the efficiency of the wave-propagation code being used, and the area of interest. The code used by Aagaard (Aagaard *et al.*, 2001) employs a finite-element discretization scheme with second order spatial and temporal accuracy, whereas the ones used by Dolenc *et al.* (Larsen and Schultz, 1995), Graves (Graves, 1996b; Day and Bradley, 2001; Graves, 2008), and Harmsen *et al.* (Liu and Archuleta, 2002; Liu and Archuleta, 2006) all employ staggered-grid finite-difference discretization schemes with fourth-order spatial accuracy and second order temporal accuracy. The unstructured finite-element implementation (four-node tetrahedral elements) in Aagaard's simulations allows arbitrary, albeit smooth (to prevent elements with poor aspect ratios) spatial variations in discretization size. In this study, the element size is equal to about one tenth of the local wavelength of shear waves with a period of 2.0 sec. This reduces the number of degrees of freedom in the system and permits a larger timestep compared with a uniform discretization size. Dolenc *et al.* and Graves both use uniform discretization sizes, whereas Harmsen *et al.* use a discretization size of 50 m in the top 700 m with a horizontal grid size of 150 m at depths greater than 700 m; the vertical grid size is 50 m down to a depth of 950 m, which then increases linearly to 150 m at a depth of 1500 m, and then to 250 m at a depth of 30 km.

Table 1
Wave-Propagation Codes and Modeling Domains

	Aagaard	Dolenc *et al.*	Graves	Harmsen *et al.*
Domain				
Length	250 km	220 km	180 km	128 km
Width	110 km	135 km	84 km	52 km
Maximum depth	40 km	50 km	45 km	31 km
Northwest corner	−123.7083, 38.2832	−123.3610, 37.9610	−122.9500, 37.7000	−122.7313, 37.6313
Northeast corner	−122.7002, 38.8944	−122.1150, 38.6800	−122.1748, 38.1326	−122.3116, 37.9610
Southeast corner	−121.0208, 37.0716	−120.6670, 37.0640	−121.0106, 36.8075	−121.2978, 37.1331
Southwest corner	−122.0180, 36.4894	−121.9000, 36.3600	−121.7858, 36.3749	−121.7173, 36.8069
Projection	None (3D Earth)	Ellipsoidal transverse Mercator	Spheroidal	Ellipsoidal transverse Mercator
Discretization	Unstructured FE	Staggered-grid FD	Staggered-grid FD	Staggered-grid FD
Space	Second order	Fourth order	Fourth order	Fourth order
Time	Second order	Second order	Second order	Second order
Resolution	Variable	125 m	150 m	50 m, 150 m
Bandwidth	T > 2.0 sec	T > 1.25 sec	T > 1.0 sec	T > 1.0 sec
Minimum V_s	700 m/sec	500 m/sec	760 m/sec	330 m/sec
Features				
Topography	Yes	Bulldozed	Bulldozed	Squashed
Water	Air filled	Included	Sediment filled	Excluded
Material properties	USGS 05.1.0	USGS 05.1.0	USGS 05.1.0	USGS 05.1.0
Attenuation	No	No	Graves	USGS 05.1.0 (Beroza) Graves (Wald)
Earthquake source	Offset in mesh	Point sources	Point sources	Point sources
Number of point sources	N/A	34020 (Beroza) 47424 (Wald)	1215 (Beroza) 2400 (Wald)	1099 (Beroza) 316
Fault surface	3D geologic model	Plane	Plane	Plane

The corners of the bounding boxes of each domain are given in longitude and latitude (World Geodetic System [WGS84] horizontal datum).

The 3D geologic model and the USGS Bay Area Velocity Model 05.1.0 both include topography and bathymetry. As a result, the ground-motion simulations must account for topography and bathymetry when querying the seismic velocity model for material properties. Free surfaces are natural boundary conditions in finite-element implementations, so it is easy to deform the top surface of the model to conform to topography, bathymetry, and the curvature of the Earth. Consequently, the top surface in Aagaard's simulations conforms to topography and bathymetry (water is not included), where the Earth Gravity Model 1996 (Lemoine *et al.*, 1998) provides the vertical reference for mean sea level in order to account for the curvature of the Earth. The topography and bathymetry are smoothed with two passes of the Laplacian smoothing filter built into LaGriT (Los Alamos National Laboratory, 2005), the software used to construct the finite-element mesh.

The three finite-difference implementations use different methods for accounting for topography and bathymetry. Because finite-difference grids do not readily accommodate curvature in domain boundaries, each of the three finite-difference implementations employs a projected coordinate system with a flat top surface. Dolenc *et al.* and Harmsen *et al.* use ellipsoidal transverse Mercator projections, whereas Graves uses a spheroidal projection. For the sizes of the domains in this study, the differences in geometry arising from how the finite-difference implementations handle topography are much more significant than the differences between the projections. Two general approaches for making the irregular topography and bathymetry of the Earth a horizontal plane include (1) bulldozing the surface of the Earth by stripping away any material above some elevation (usually sea level) and filling in any voids below this elevation with some generic material, and (2) squashing the surface of the Earth by deforming the near-surface material in the vertical direction so that the free surface is flat and aligned at some elevation. Figure 4 illustrates the resulting velocity structure for each of these methods. The bulldozing method tends to remove shallow low-velocity layers but does not distort the geometry of the geologic units, whereas squashing retains shallow low-velocity layers but tends to distort the geometry of the geologic units. Dolenc *et al.* employ the bulldozing approach but include water ($V_s = 0$ m/sec) in their model, thereby eliminating the need to fill the Pacific Ocean with a generic material. Graves applies a similar approach, but fills areas below sea level with a generic sediment ($V_p = 2200$ m/sec, $V_s = 760$ m/sec, density $= 2100$ kg/m^3). Harmsen *et al.*, on the other hand, rely on the squashing method wherein the top 1 km of the Earth is deformed to flatten the Earth's surface; this maintains the presence of low-velocity material and only distorts the geometry of the geologic units in the top 1 km.

Simulations of the Loma Prieta earthquake by Hartzell *et al.* (2006) suggest that the attenuation provided by the USGS Bay Area Velocity Model 05.1.0, which uses relations between wave speed and Q from Olsen *et al.* (2003), provides too much attenuation in the Santa Clara Valley. As a result, some of the simulations use a simple attenuation model developed by Graves 2008, where

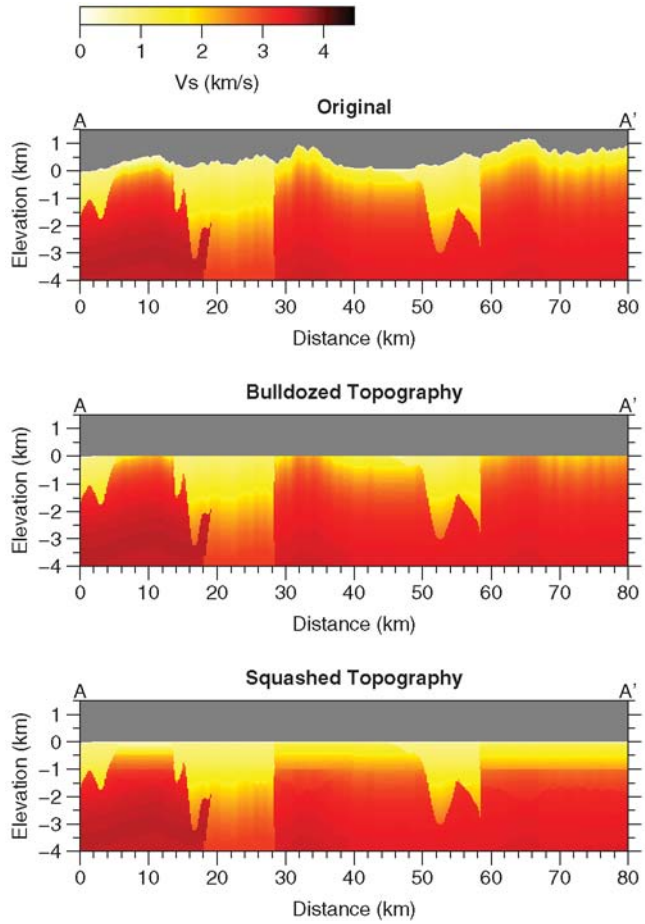

Figure 4. Cross section of shear-wave speed (V_s) along profile AA' (see Fig. 2) at 4× vertical exaggeration with topography (top), with topography bulldozed (middle), and with topography squashed in the top 1 km (bottom).

$$Q_s = a[v_s(\text{km/sec})]^b, \tag{6}$$

and

$$v_s < 0.9 \text{ km/sec}; \qquad a = 50, \quad b = 1.0, \tag{7}$$

$$0.9 \text{ km/sec} \le v_s < 3.4 \text{ km/sec}; \qquad a = 60, \quad b = 1.5, \tag{8}$$

$$v_s \ge 3.4 \text{ km/sec}; \qquad a = 500, \quad b = 0.0, \tag{9}$$

rather than the one included in the USGS Bay Area velocity model. This simple attenuation model has worked well in previous studies of earthquake simulations in the Los Angeles basin region (Graves and Pitarka, 2004; Graves, 2008).

Satoh (2006) found similar Q_s values at periods around 1.0 sec in a study of frequency-dependent shear-wave attenuation in the Sendai basin in Japan. Neither Aagaard nor Dolenc *et al.* include attenuation in their simulations.

The wave-propagation codes also use different techniques for generating earthquake ruptures using the Beroza and Wald source models discussed earlier. Aagaard incorporates the fault geometry into the finite-element model as a surface in the interior of the domain, thereby permitting an earthquake source to be implemented with double nodes, where slip is associated with an offset in the finite-element mesh across a fault surface (Aagaard *et al.*, 2001). Additionally, the fault surface is not the planar geometry from the original Wald and Beroza source models but the nonplanar geometry of the San Andreas fault from the 3D geologic model; the San Andreas fault was constructed to pass through the Loma Prieta aftershocks (Jachens *et al.*, 2006). The same smoothing applied to the topography, and bathymetry was also applied to the fault surface. The source parameters from the planar models are projected onto the nonplanar surface; this creates some small deviations in strike and dip from the original Beroza and Wald source models. Dolenc *et al.*, Graves, and Harmsen *et al.* all use evenly distributed point sources to generate the finite-fault earthquake source with the same fault geometry as the original source models. We will discuss the ramifications of using these different fault geometries later when analyzing the synthetic waveforms.

Including Short-Period Energy

Graves extended his simulations to shorter periods using the hybrid procedure described in Graves and Pitarka (2004). This simulation technique combines a stochastic approach at short periods (0.1 sec $< T <$ 1 sec) with the 3D deterministic approach described earlier at long periods ($T >$ 1 sec) to produce broadband ground-motion synthetics.

The short-period simulation methodology sums the response for each subfault assuming a random phase, an omega-squared source spectrum, and simplified Green's functions. The methodology follows from Boore (1983) with the extension to finite faults given by Frankel (1995) and Hartzell *et al.* (1999). Each subfault ruptures with a moment proportional to the final slip of the subfault given by the original source model, and the values are scaled uniformly so that the moment matches that of the original source model. The subfault corner frequency is defined by

$$f_c = s_z s_t \frac{v_r}{\pi d}, \tag{10}$$

where v_r is the rupture speed, d is the subfault dimension, s_z scales the corner frequency with depth, and s_t relates the corner frequency to the rise time of the subfault source. We use a uniform value of $s_t = 1.6$. The scaling of the corner frequency with depth follows

$$s_z = \begin{cases} 1.0 & \text{if } h < h_0, \\ 1.0 + 0.4\frac{h-h_0}{h_1-h_0} & \text{if } h_0 \le h < h_1, \\ 1.4 & \text{if } h > h_1, \end{cases} \tag{11}$$

where h_0 is 5 km, h_1 is 10 km, and h is the depth of the center of the subfault in kilometers. Calibration experiments were used to determine the constant factor of 0.4. This parameterization follows from the observation in crustal earthquakes that slip rate is relatively low for shallow ruptures and increases with rupture depth (Kagawa *et al.*, 2004). Because corner frequency scales with slip rate, this formulation replicates the trend of the observations. We note that although this formulation reduces the number of free parameters, it is not unique and probably has tradeoffs with other parameters in the stochastic model. In particular, allowing the subfault stress parameters to vary across the fault would accommodate a similar slip rate scaling. Instead, we fix the stress parameter to a uniform value of 50 in our simulations. The convolution operator of Frankel (1995) scales the subevent rise time to the target rise time. Additionally, this operator ensures that the result does not strongly depend on the choice of the subfault dimensions.

The formulation requires the specification of a 1D layered velocity model in calculating simplified Green's functions and impedance effects. In this study, we create a 1D velocity model (given in Table 2) that roughly follows the average depth variations in the 3D structure, and we include both direct and Moho-reflected rays, which are attenuated by $1/R_p$, where R_p is the total path length traveled by the particular ray. For each ray, we compute a radiation pattern coefficient by averaging over a range of slip mechanisms and takeoff angles. Anelasticity is incorporated via a travel-time-weighted average of the Q values for each of the material layers and a generic rock site spectral decay operator, $\kappa = 0.05$

Table 2
1D Seismic Velocity Model for Short-Period Simulations

Layer Thickness (m)	V_p (m/sec)	V_s (m/sec)	Density (kg/m^3)
2	1700	350	2000
4	1800	550	2100
6	1800	800	2100
8	1900	900	2100
10	2000	1000	2200
70	2400	1100	2300
100	2600	1200	2400
300	3000	1400	2450
500	3600	1950	2500
500	4200	2300	2550
1000	4800	2800	2600
500	5250	3000	2620
2000	5600	3250	2650
2000	5900	3410	2700
2000	6150	3550	2750
8000	6350	3620	2850
8000	7000	4100	3000
999999	8000	4500	3300

(Anderson and Hough, 1984). Finally, gross impedance effects are included using quarter wavelength theory (Boore and Joyner, 1997) to derive amplification functions that are consistent with the specified 1D velocity structure.

In both the deterministic and stochastic calculations, Graves restricts the minimum shear-wave speed to 760 m/sec. To account for site-specific geologic conditions in the Graves simulations, we apply period-dependent, nonlinear amplification functions to the simulated time histories. These functions were derived empirically by Borcherdt (1994) and have the general form

$$F_x = \left(\frac{v_{\text{site}}}{v_{\text{ref}}}\right)^{m_x}, \tag{12}$$

where v_{site} denotes the 30 m travel-time-averaged shear-wave speed (V_s30) at the site of interest, v_{ref} corresponds to the V_s30 where the ground response is known, and m_x denotes an empirically determined factor that depends on both period and ground-motion level. These factors range from -0.05 at short periods and high-reference PGA values to 0.65 at long periods and low-reference PGA values. This dependence on both period and ground-motion level approximates the effects of nonlinear site response. For each location in the simulation grid, we obtain the site-specific V_s30 (v_{site}) from the map of Wills *et al.* (2000), and v_{ref} is set to the shear-wave speed from the 3D velocity model for that location (with values are constrained to be 760 m/sec and faster). An amplification function for a given site is derived by first determining the short- and midperiod factors from equation (12) using the tabulated m_x values in Borcherdt (1994) and the reference PGA from the stochastic response. Next, we construct a smoothly varying function in the frequency domain by applying a simple taper to interpolate the factors between the short- and midperiod bands. Finally, we combine the individual stochastic and deterministic responses into a single broadband time history using a set of matched Butterworth filters (Hartzell *et al.*, 1999).

Results

To assess how well the ground-motion simulations estimate the shaking intensity over the San Francisco Bay Area, we compare MMI using ShakeMaps and velocity waveforms at stations that recorded the earthquake. We also examine the consistency in shaking intensities and waveforms across the four wave-propagation codes and two source models.

Shaking Intensity

Instrumental ShakeMaps, which use empirical attenuation relationships to guide interpolation of recorded peak motions onto a dense uniform grid, provide a useful tool with which to quantify agreement between observations and ground-motion simulations over a region using many more data points than station locations alone. Examining the shaking intensities at this finer resolution facilitates identifying any areas with systematic discrepancies in shaking intensity between the synthetics and observations, and associating the areas with geologic structures, such as particular geologic units or with source characteristics, such as rupture directivity. This does limit the analysis to the peak motions because ShakeMap (Wald *et al.*, 2005) focuses only on the shaking intensity via peak horizontal velocities and accelerations. However, in our ground-motion modeling of the 1906 earthquake (Aagaard *et al.*, 2008), the ShakeMap compiled by Boatwright and Bundock (2005) provides the primary independent constraint on the ground motions. Comparing our synthetics with the instrumental ShakeMap for the Loma Prieta earthquake demonstrates the usefulness of this analysis technique. We will consider the duration and other details of the motions later, when we examine the velocity waveforms.

ShakeMap adds false stations in areas with sparse station coverage, computing the peak velocities and accelerations from regional attenuation relationships (Boatwright *et al.*, 2003). These attenuation relationships do not include directivity effects. ShakeMap interpolates the peak velocities and accelerations onto a uniform grid, giving equal weight to the real and false stations. Peak horizontal ground velocity (PGV) and peak horizontal ground acceleration (PGA) values are converted to MMI by applying an empirical relation between PGV and PGA and MMI (Wald *et al.*, 2005). For the broadband simulations and instrumental ShakeMap,

$$\text{MMI} = \begin{cases} \text{MMI}_{\text{PGA}} & \text{if MMI} < \text{V}, \\ \frac{1}{2}[(\text{VII} - \text{MMI}_{\text{PGA}})\text{MMI}_{\text{PGA}} \\ \quad + (\text{MMI}_{\text{PGA}} - \text{V})\text{MMI}_{\text{PGV}}] & \text{if V} \le \text{MMI} < \text{VII}, \\ \text{MMI}_{\text{PGV}} & \text{if MMI} \ge \text{VII}, \end{cases} \tag{13}$$

$$\text{MMI}_{\text{PGA}} = \begin{cases} 2.20\log(\text{PGA}) + 1.00 & \text{if MMI} < \text{V}, \\ 3.66\log(\text{PGA}) - 1.66 & \text{if MMI} \ge \text{V}, \end{cases} \tag{14}$$

$$\text{MMI}_{\text{PGV}} = \begin{cases} 2.10\log(\text{PGV}) + 3.40 & \text{if MMI} < \text{V}, \\ 3.47\log(\text{PGV}) + 2.35 & \text{if MMI} \ge \text{V}, \end{cases} \tag{15}$$

where PGA is in *g*s and PGV is in cm/sec.

The ground motions in our long-period simulations have low PGA values, applying these relations to our long-period simulations gives MMI values that are too small. To remedy this, we use only the PGV-to-MMI relation (equation 15) in computing the MMI values on the dense grid for our long-period simulations. Similarly, we construct a long-period ($T > 1.0$ sec) instrumental ShakeMap by low-pass filtering (corner frequency of 1 Hz) the strong-motion records before

computing the peak ground velocities and using the PGV-to-MMI relation. As a result, the long-period instrumental ShakeMap (Fig. 1) is compatible with our long-period simulations.

Comparing the synthetic intensities from our long-period simulations with the ShakeMap intensities corresponds to comparing the logarithms of the synthetic peak velocities and the ShakeMap peak velocities; using MMI provides consistency with our ground-motion modeling of the 1906 earthquake and facilitates visualization due to the more gradual decay of MMI with distance compared to PGV. Because of discrepancies among how the simulations and the ShakeMap algorithm handle water, we do not include areas covered by water in our analysis.

We first examine the consistency across the wave-propagation codes and two source models and how well they reproduce the long-period ShakeMap before considering how well the broadband Graves simulations reproduce the broadband instrumental ShakeMap. Figures 5–8 show the ShakeMaps for each of the eight ground-motion simulations along with differences with respect to the long-period ($T > 1.0$ sec) ShakeMap given in Figure 1. Ⓔ The electronic edition of *BSSA* contains additional figures displaying the differences in synthetic intensities from different wave-propagation codes. Comparing the intensities across all eight ground-motion simulations, we see that both source models create strong along-strike directivity consistent with the long-period ShakeMap. The Beroza source model radiates more energy to the south, whereas the Wald source model radiates more energy to the north. This results in stronger shaking for the Beroza source model compared with the Wald source model about 30-km inland from the Monterey Bay coastline as well as around Hollister, where strong shaking extends across the Calaveras fault to the east. Within about 20 km of the rupture the two models produce similar distributions of shaking, with both source models causing strong shaking in the Santa Clara Valley basins consistent with the long-period ShakeMap, especially in the Cupertino basin south of San Jose. Further north along the San Francisco peninsula, as well as on the east side of the San Francisco Bay, the Wald source model gives stronger shaking than the Beroza source model, providing a better fit to the long-period ShakeMap.

The misfit in the shaking intensities in the simulations relative to the long-period ShakeMap varies among the modelers and between the source models. The areas with the largest discrepancies include the regions northeast of the rupture, south of the rupture, the north end of the San Francisco peninsula region, and the immediate perimeter of the San Francisco Bay. Amplification from soft near-surface sediments in the northern end of the San Francisco peninsula and in the immediate perimeter of the San Francisco Bay, which are not included in the long-period simulations, explains why the synthetic intensities are lower than the observed intensities in these two areas. The regions to the northeast and to the south of the rupture where the discrepancies between the simulations and observations are the largest are also the regions where the ShakeMap is least constrained as a result of poor station coverage. In these areas, the ShakeMap interpolation relies on false stations, which do not include directivity effects. Directivity effects increase the shaking intensity along the strike of the rupture and decrease the intensity normal to the rupture. As a result, the ShakeMap intensities are too high northeast of the fault (i.e., the synthetics tend to under predict the long-period ShakeMap) and too low along the strike of the rupture (i.e., the synthetics tend to over predict the long-period ShakeMap).

The ground-motion simulations also tend to over predict the shaking intensity east of the Hayward fault in the area between Livermore and Concord. The region where the intensities are over predicted is bound abruptly to the west by the Hayward fault; this area is underlain by the Mesozoic Great Valley Sequence. The consistency in the boundaries of this area of over prediction across all four wave-propagation codes suggests that the shear-wave speeds in the Great Valley Sequence are too slow, and adjusting the rules assigning material properties for this clastic sedimentary sequence accordingly would improve the fit. Likewise, the simulations also tend to over predict the shaking in the La Honda basin in the Santa Cruz mountains west of San Jose, suggesting that the shear-wave speeds for the La Honda basin require similar increases.

The mean misfits range from −0.24 MMI units (15% in PGV) for the Harmsen *et al.* simulation using the Wald source model to −0.70 MMI units (37% in PGV) for the Graves simulation using the Beroza source model, where values less than zero indicate that the simulations, on average, under predict the intensity of shaking. We attribute the negative bias in the misfits to limiting the minimum shear-wave speed in the simulations, which reduces amplification of motions in shallow sediments. Simulations with a lower minimum shear-wave speed tend to have smaller average misfits. Aagaard's simulations are an exception, probably due to the inclusion of topography, which incorporates more soft near-surface sediments compared with implementations that bulldoze all material above sea level (as illustrated in Fig. 4). All four wave-propagation codes produce shaking intensities that agree to within one MMI unit (a factor of 2 in PGV) of each other over nearly the entire area, yielding consistent standard deviations in misfit from the mean for the long-period ShakeMap that range from 0.64 to 0.86 MMI units (52%–77% in PGV).

The Graves broadband simulations, which include frequencies up to 10 Hz, allow direct comparison of the shaking intensities from the simulations with the (broadband) instrumental ShakeMap; we do not need to construct a band-limited ShakeMap in order to compare intensities between the simulations and the observations as we did for the long-period simulations. Figure 9 shows the synthetic ShakeMaps for the broadband simulations with the Beroza and Wald source models and the differences with respect to the instrumental ShakeMap. Including site corrections signifi-

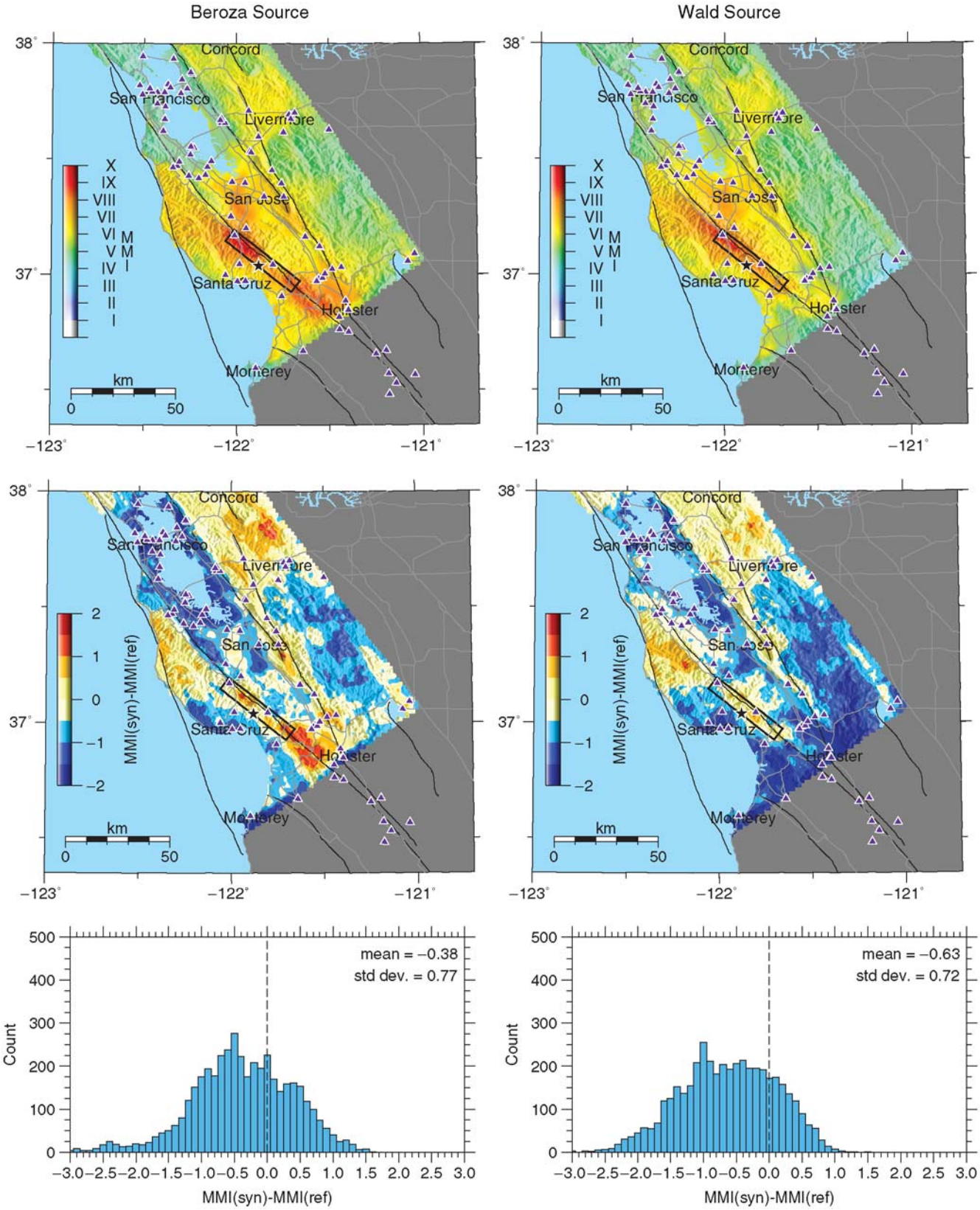

Figure 5. Synthetic ShakeMaps for Aagaard's ($T > 2.0$ sec) simulations of the Loma Prieta earthquake with the Beroza and Wald source models. The middle and bottom panels show the differences between the synthetic ShakeMaps (top panels) and the long-period ($T > 1.0$ sec) ShakeMap. The differences are less than one MMI unit over much of the simulation domain.

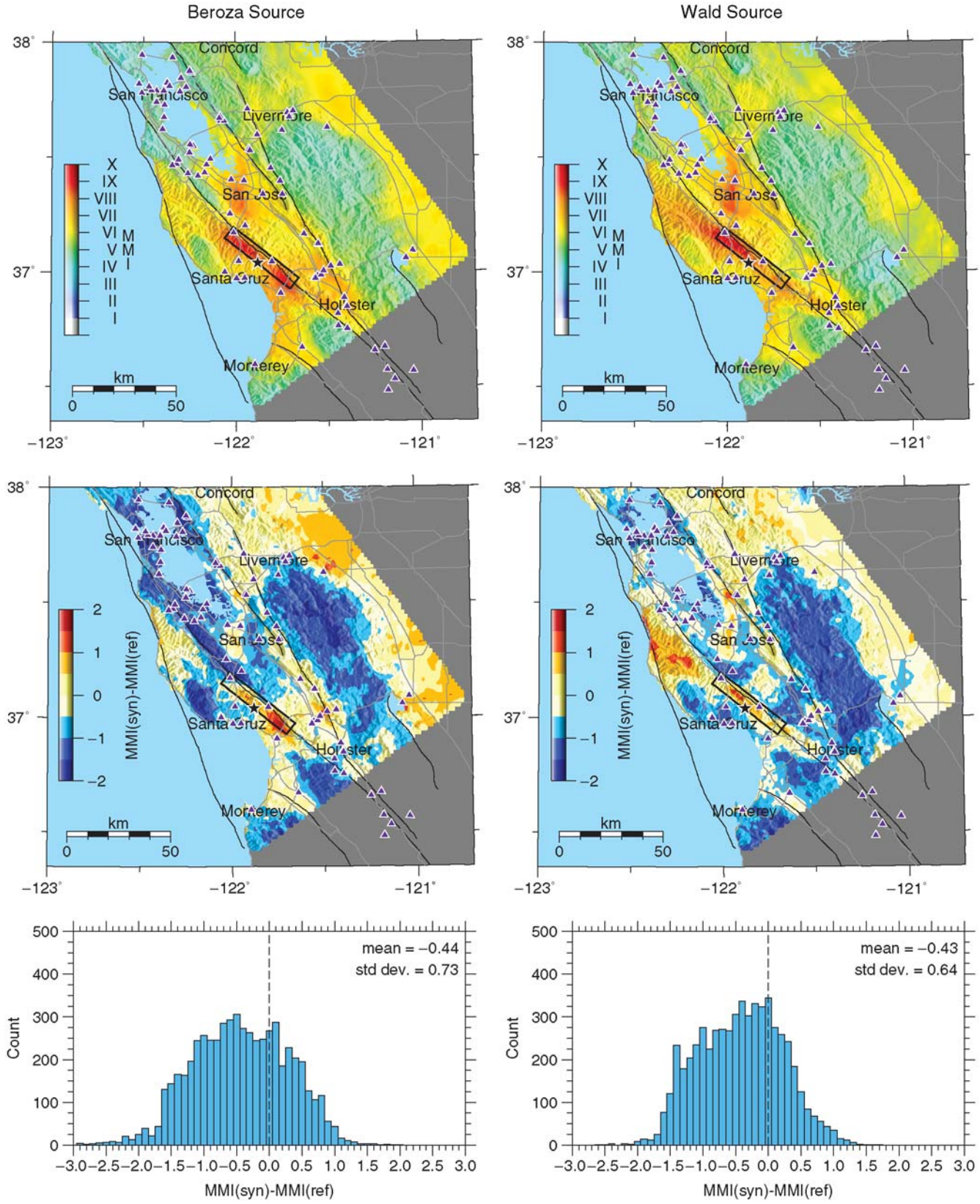

Figure 6. Synthetic ShakeMaps for Dolenc *et al.*'s ($T > 1.25$ sec) simulations of the Loma Prieta earthquake with the Beroza and Wald source models. The middle and bottom panels show the differences between the synthetic ShakeMaps (top panels) and the long-period ($T > 1.0$ sec) ShakeMap. The greatest differences tend to occur in areas with topography where the simulations under predict the shaking due to bulldozing of the sediments above sea level.

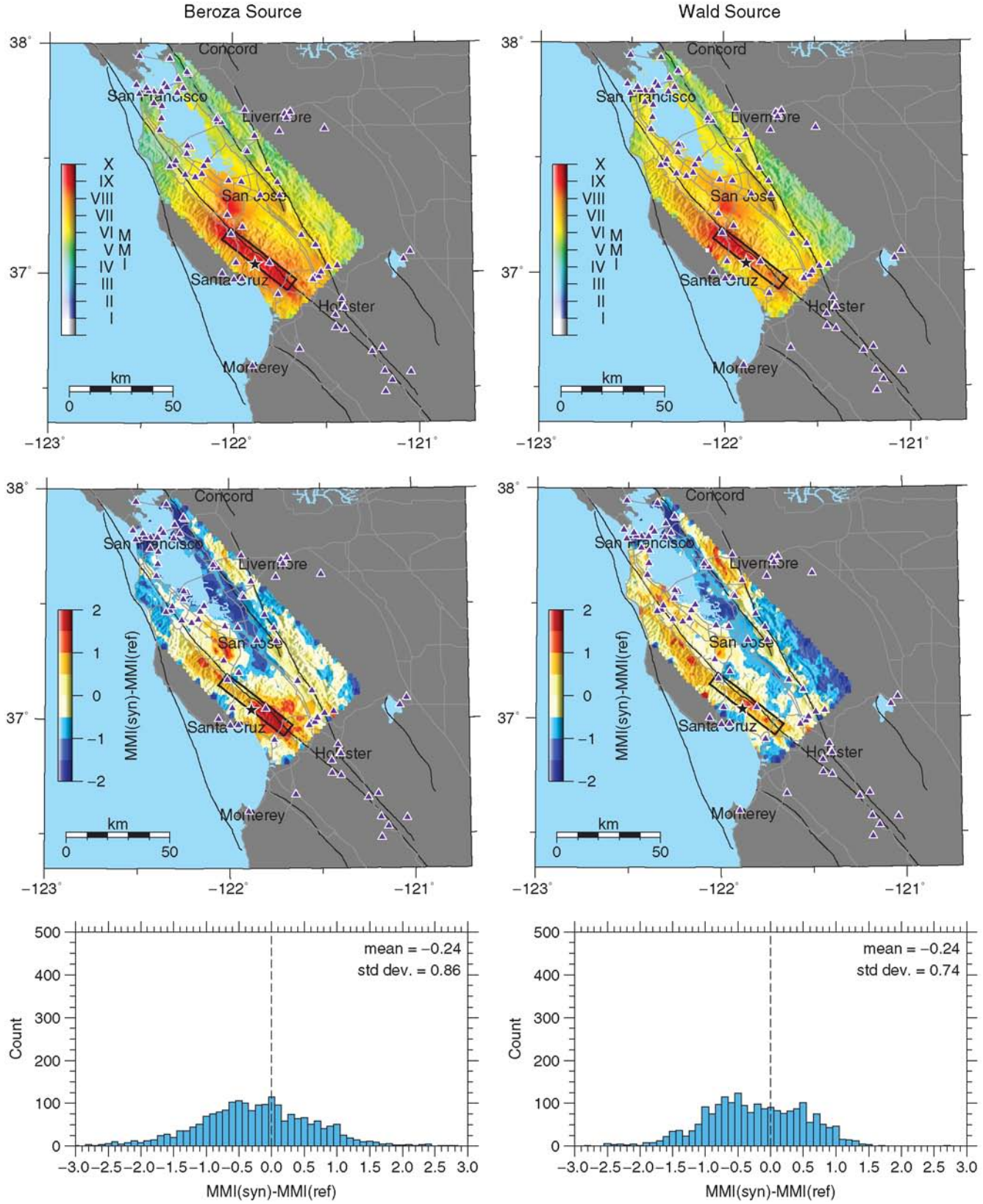

Figure 7. Synthetic ShakeMap for Harmsen *et al.*'s ($T > 1.0$ sec) simulations of the Loma Prieta earthquake with the Beroza and Wald source models. The middle and bottom panels show the differences between the synthetic ShakeMaps (top panels) and the long-period ($T > 1.0$ sec) ShakeMap. Permitting minimum shear-wave speeds down to 330 m/sec results in the smallest mean misfit among the long-period ground-motion simulations.

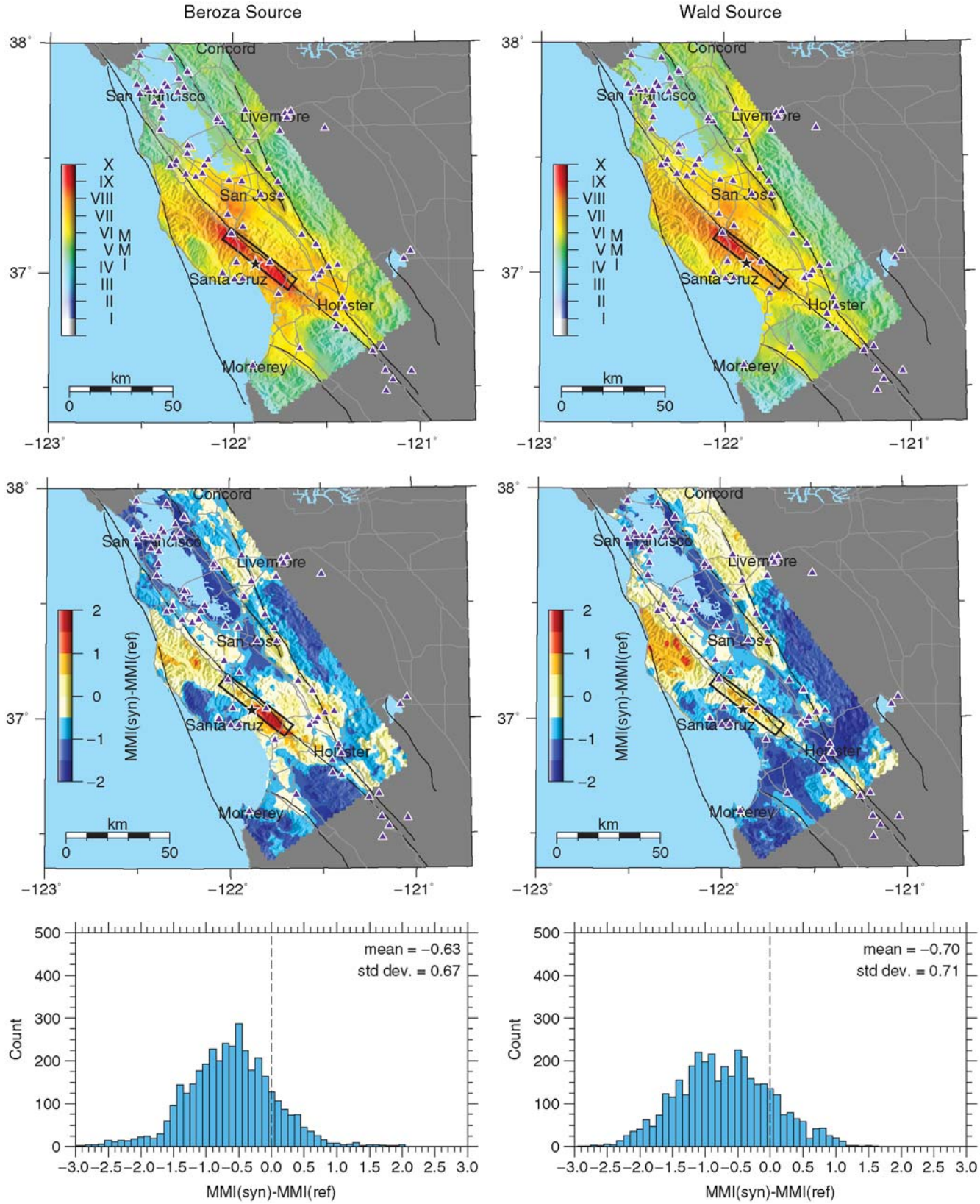

Figure 8. Synthetic ShakeMaps for Graves's ($T > 1.0$ sec) simulations of the Loma Prieta earthquake with the Beroza and Wald source models. The middle and bottom panels show the differences between the synthetic ShakeMaps (top) and the long-period ($T > 1.0$ sec) ShakeMap. The greatest differences tend to occur in areas with topography where the simulations under predict the shaking due to bulldozing of the sediments above sea level.

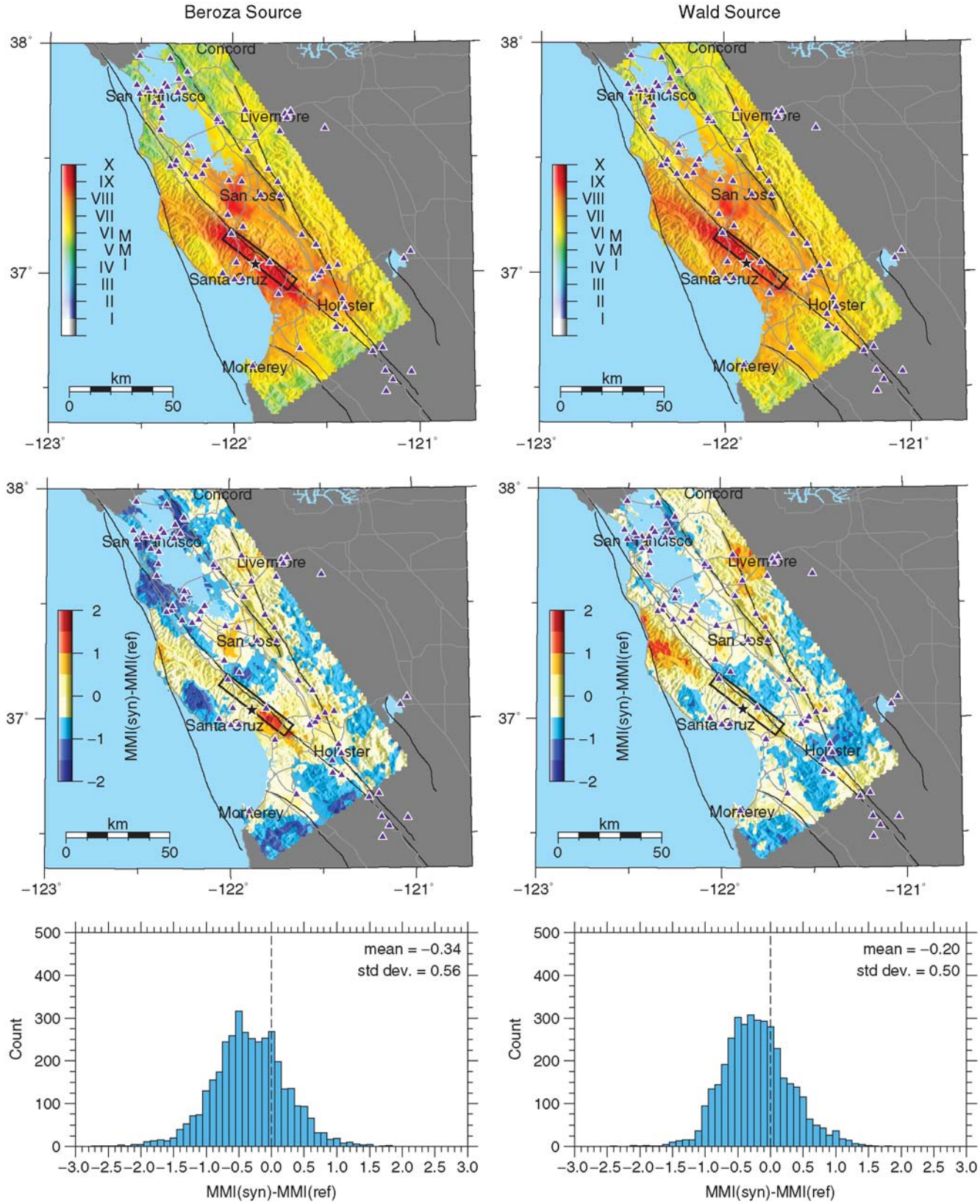

Figure 9. Synthetic ShakeMap for Graves's broadband ($T > 0.1$ sec) simulations for the Loma Prieta earthquake with the Beroza and Wald source models. The middle and bottom panels show the differences between the synthetic ShakeMaps (top panels) and the broadband ShakeMap. Including short-period energy and site effects decreases the standard deviation of the misfit and significantly reduces the mean misfit.

cantly improves the fit to the observed intensities, while maintaining the agreement in areas where the long-period simulations reproduce the instrumental ShakeMap intensities. In the broadband simulations the differences are less than one MMI unit over nearly the entire simulation domain with a mean misfit of −0.34 MMI units (20% in PGV) for the Beroza source model and −0.20 MMI units (12% in PGV) for the Wald source model. The standard deviations also decrease slightly to 0.56 and 0.50 MMI units (about 40%–45% in PGV) for the two source models.

The differences between the Wald and Beroza source models remain evident, however, with the Wald source model providing a better match in the north and the Beroza source model providing a slightly better match in the south. The discrepancies in the area east of the rupture, where all of the long-period simulations under predict the intensities in the long-period ShakeMap by 1–2 MMI units, are reduced to less than one MMI unit in the broadband simulations. The shear-wave velocities at the surface are relatively fast, corresponding to minimal site corrections, so the improvement in this area can be attributed to including radiation at short periods (i.e., $T < 1.0$ sec). We also observed similar improvement within and around the perimeter of the San Francisco Bay, but here the site corrections are the greatest. As one might expect, the broadband ground-motion simulations over predict the shaking intensities in the two regions where the long-period simulations consistently over predict the shaking intensities, the La Honda Basin in the Santa Cruz mountains northwest of the rupture and in the area associated with the Great Valley Sequence geologic unit east of the Hayward fault between Concord and Livermore.

Velocity Waveforms

We now change focus and switch from comparing shaking intensities over a large area to analyzing the synthetic ground motions more closely through examination of velocity waveforms with recorded motions. It is important to realize that there can be much stronger tradeoffs between rupture parameters and the 3D velocity structure in the waveforms compared with the shaking intensities. For example, lower shear-wave velocities in the Tertiary/Quaternary sedimentary fill of Cenozoic basins increases the shaking intensities and shear-wave amplitudes above these basins, which can be difficult to distinguish from larger slip on the fault. Also, velocity contrasts across near-vertical boundaries like faults affect the amount of seismic energy reflected and transmitted from these surfaces resulting in significant changes to the relative amplitudes of phases in the waveforms but little change to the peak amplitude associated with the shaking intensity. Depending on the distribution of seismic stations, it can be difficult to distinguish variations in reflected and transmitted energy from changes in fault slip. Other rupture parameters, notably rupture velocity and slip rise time, can also modify the interpretation of the seismic velocity structure if they are not well known.

Figure 10 displays the locations of 14 stations where we will examine the velocity waveforms. Ⓔ The electronic edition of *BSSA* provides waveforms for these plus 38 additional sites; in one set, we low-pass filter the waveforms to a common bandwidth of $T > 2.0$ sec, and in the other set, we low-pass filter the synthetic waveforms to the bandwidth of the corresponding simulation. Instead of attempting to quantify the consistency across the synthetic waveforms and how well the waveforms agree with the recorded motions using one or more metrics (which may not accurately reflect agreement or disagreement in the features of interest due to the complexity of the waveforms), we evaluate the agreement using careful inspection of the specific features that we want to match, such as absolute and relative amplitudes of various phases, duration of shaking, and basin response.

Figure 11 shows the waveforms at seven stations south of San Jose. The observed motions at stations LGPC and SNJ, which sit northwest and northeast of the epicenter, are dominated by simple velocity pulses associated with rupture directivity and are well predicted by the synthetics from both source models. This close agreement indicates that our adjustment of the slip time function and rise time from the original Beroza and Wald source models has minimal affect on the resulting ground motions. The synthetics for both source models over predict the motions at BRAN in the La Honda basin, with significant differences in relative amplitude of the phases, especially on the east component. The consistency across the two source models in this misfit suggests that the errors are associated with the velocity structure. The over prediction of the shaking intensities in this region

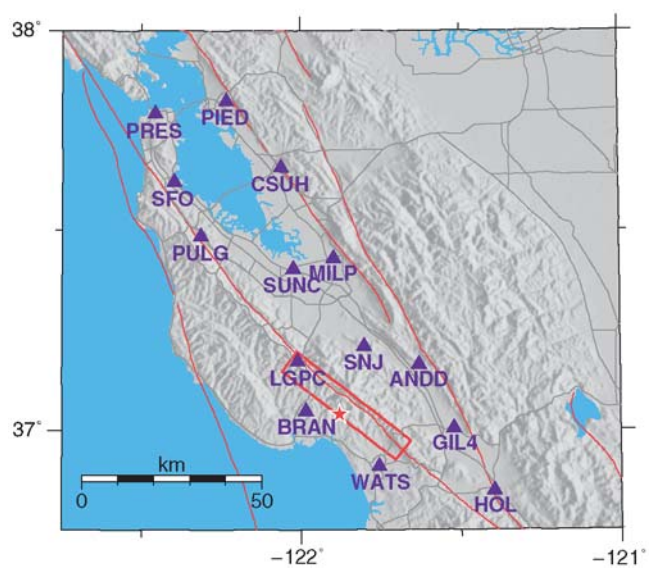

Figure 10. Locations of the 14 stations used in the comparison of velocity waveforms. The locations span a wide range of azimuths and are relatively uniformly distributed. Ⓔ The electronic edition of *BSSA* contains waveforms at 52 sites.

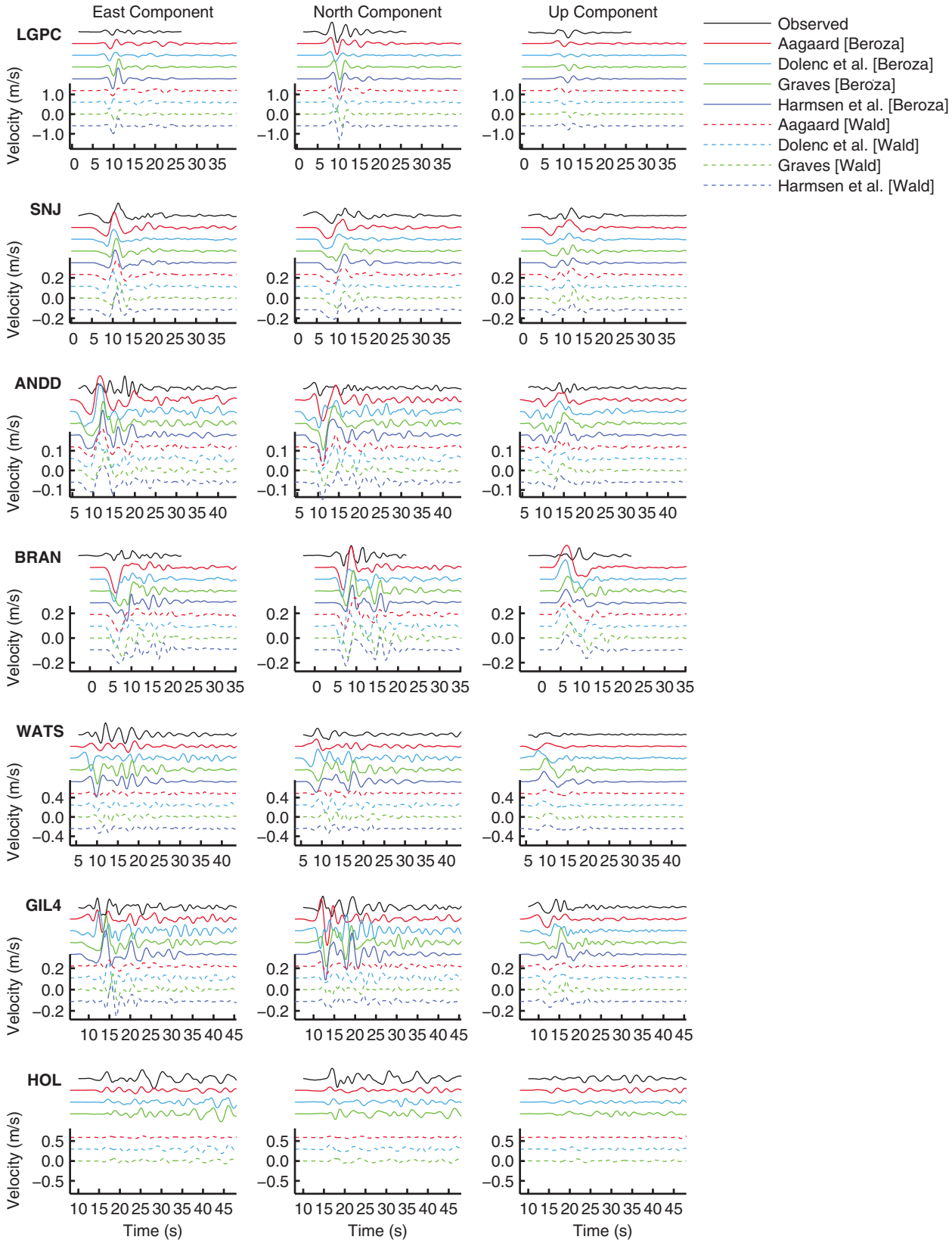

Figure 11. Velocity waveforms for seven southern sites. All waveforms have been low-pass filtered to a bandwidth of $T > 2.0$ sec. The three components for each station are plotted on the same scale, but the scale for each station is independent. At most sites close to the rupture, the synthetic waveforms reproduce the amplitude and duration of the observed motions with consistent waveform shapes across the wave-propagation codes.

noted earlier supports this, and increasing the wave speeds in the seismic velocity model for the La Honda basin on the west side of the San Andreas fault will likely improve the fit. Incorporation of additional data for this region (e.g., Catchings *et al.*, 2004) should also lead to more accurate characterization of the velocity structure.

Stations on the southern side of the rupture clearly demonstrate the differences in rupture between the Wald and Beroza models southeast of the hypocenter. The general trends across the synthetics are that the Beroza source model synthetics have larger amplitudes than the observed motions at stations ANDD, WATS, and GIL4, whereas the Wald source model synthetics are too small, or in some cases, closer to the correct amplitudes. These results suggest that a compromise between the two source models or a more equally weighted bilateral rupture would fit the data better overall. However, close inspection reveals significant differences in waveform polarity and shape across the simulations for some of these sites.

For example, Aagaard's synthetics for the Beroza source model at station GIL4 tend to fit the observed motions quite closely, whereas the synthetics from Graves, Harmsen *et al.*, and Dolenc *et al.* at GIL4 for the Beroza source model all have the incorrect polarity for the first phase. The four wave-propagation codes yield much more consistent results for the Wald source model, although the Aagaard synthetics for the Wald source model do not fit the observed motions as well as they do for the Beroza source model. Consequently, the most likely explanation for the misfit in the three finite-difference implementations for the Beroza source model is the fault strike of 130° east of north in the Beroza source model compared with a strike of 128° in the Wald source model; recall that Aagaard uses the nonplanar fault geometry from the 3D geologic model with both source models, which is more consistent with the strike in the Wald source model. These observations hold for most of the other stations in the Gilroy array (Ⓔ see the electronic edition of *BSSA*) and may also apply to station WATS as well. At WATS the synthetics do a reasonable job of fitting the east component but have difficulty reproducing the north and vertical components. The Aagaard synthetics match the polarity and shape of the north and vertical components better than any of the synthetics from the three other modeling groups.

At Hollister (HOL) the simulations under predict the horizontal motions. This station lies very close to the Calaveras fault and the recorded ground motions may be influenced by the low-velocity fault zone surrounding the fault (Cormier and Spudich, 1984). The seismic velocity model used in the simulations does not include such a low-velocity zone. Incorporation of a low-velocity zone along the fault into the velocity model should result in a better fit to the recorded motions at this site.

Shifting our focus to stations north of the rupture (waveforms are given in Fig. 12), we generally find greater consistency among the synthetic waveforms across the numerical models for a given source model compared to across source models for a given numerical model. This implies that the uncertainty in the source models tends to exceed the uncertainty in the seismic velocity structure. At several stations, such as CSUH and PIED on the east side of the bay, the synthetics from both source models reproduce the amplitude and duration of the observed shaking quite well. We observe greater differences between the recorded motions and the synthetics and between the synthetics for the two source models on the west side of the bay at stations PULG, SFO, and PRES. These stations lie on a generally more complex propagation path brought about by the velocity contrast across the San Andreas fault, intervening topography, and sedimentary basins. At these locations, the Wald source model, with more energy radiated in this direction than the Beroza source model, does a better job of reproducing the amplitude and duration of shaking.

Stations MILP and SUNC recorded propagation paths across the Santa Clara Valley. The synthetics from both source models do a reasonable job of capturing the recorded surface wave excitation at these stations, except for the north component at MILP, which is under predicted. Lowering the velocities of the near-surface basin fill in the Santa Clara Valley may improve this fit. These stations that exhibit strong influence from local geology, in this case amplification from shallow sedimentary basins, are an example of locations where it is difficult to unravel the contributions of misfit arising from errors in the source model and errors in the velocity structure.

Discussion

Our simulations of the Loma Prieta earthquake using four different wave-propagation codes and the Beroza and Wald source models provide a rare opportunity to assess the consistency of different modeling approaches relative to the uncertainty in the seismic source and the geologic structure. Our results show broad consistency across the eight ground-motion simulations for each source model. We find better agreement in the shaking intensities and velocity waveforms among the wave-propagation codes for a given source model than between the two source models for a wave-propagation code. The small differences among the simulations appears to be mainly due to differences in the minimum shear-wave speed permitted in the simulations. Harmsen *et al.* used a fine enough discretization to permit shear-wave speeds down to 330 m/sec and has the smallest mean misfit with respect to the long-period ShakeMap. Conversely, using a coarser discretization and restricting the shear-wave speed to a minimum of 760 m/sec produces the greatest mean misfit to the long-period intensities (e.g., Graves long-period simulations without site corrections).

The reduced misfit with lower minimum shear-wave speed suggests that misfits can be minimized by using fine enough discretization to resolve media having the slowest seismic velocities that contribute to the response in the band-

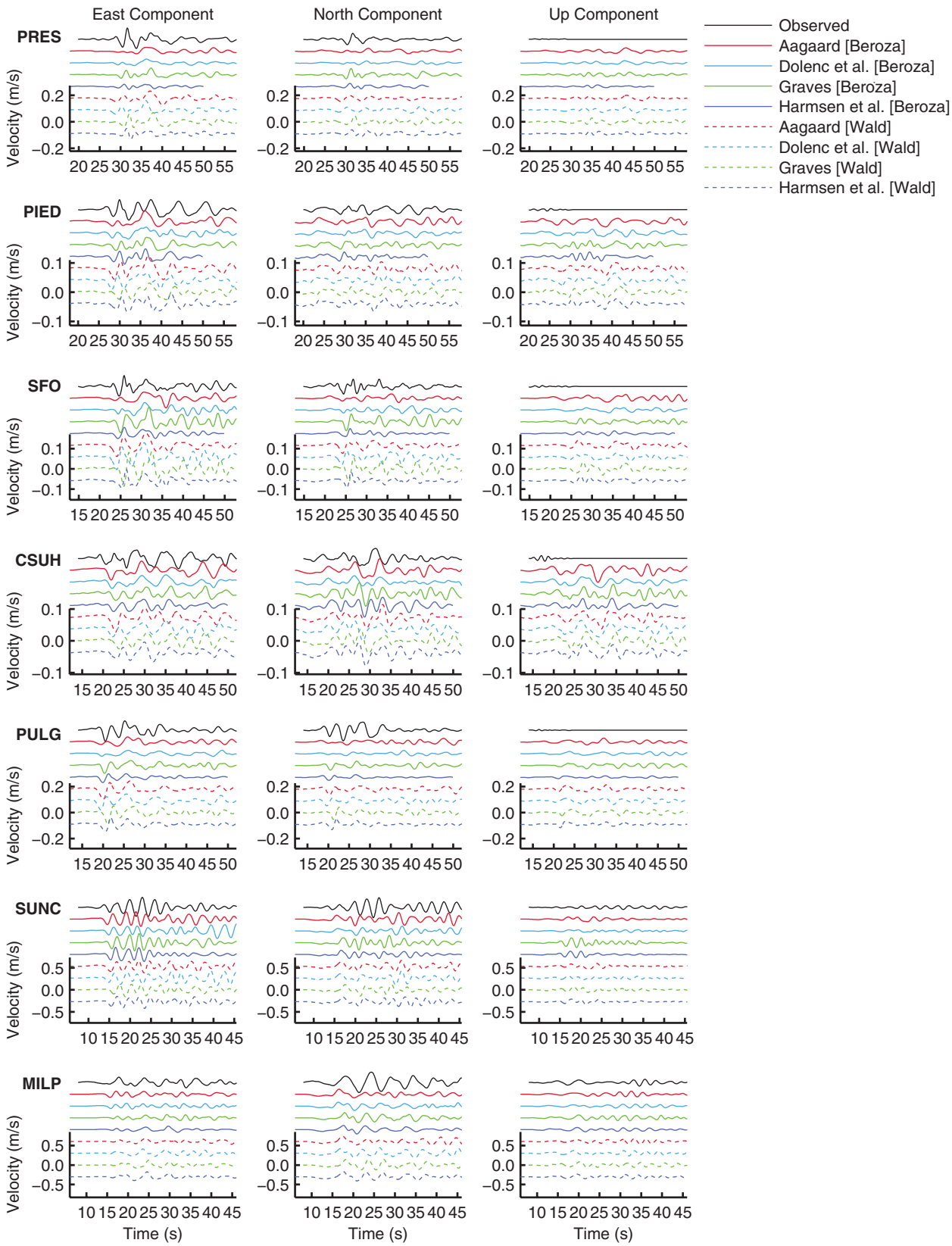

Figure 12. Velocity waveforms for seven northern sites. All waveforms have been low-pass filtered to a bandwidth of $T > 2.0$ sec. The three components for each station are plotted on the same scale, but the scale for each station is independent. The synthetic waveforms do a better job of reproducing the observed motions on the east side of the bay (stations PIED and CSUH) compared to the west side of the bay, where the propagation path is more complex.

width of the simulation (soft sediments much thinner than a wavelength have little influence on the simulated motions). The broadband simulations of Graves use site-correction factors to compensate for the high-minimum shear-wave speed. This approach appears to work quite well for matching waveform amplitudes (and, hence, shaking intensities), as evidence in mean misfits of less than 0.3 MMI units (22% in PGV) for both source models, but it cannot capture the effects on arrival times and waveform shapes resulting from errors in surface wave group velocities and mismatches in constructive and destructive interference.

We also find some minor differences arising from how topography is accommodated. Including topography seems to be the clear preference, as it results in more accurate sampling of the 3D velocity model (which includes topography) without distorting the geometry of the geologic structure. The mean misfit in shaking intensities for Aagaard's simulations (which include topography) are 0.25 and 0.07 MMI units lower than Graves's (which bulldoze all topography above sea level) for the Beroza and Wald source models, respectively, even though the minimum shear-wave speeds are similar and Aagaard's simulations are limited to $T > 2.0$ sec compared with $T > 1.0$ sec for Graves's simulations. Smaller misfits in the mountains east of San Jose in Aagaard's simulations compared with Graves's simulations support this assertion. Similarly, Harmsen *et al.*'s employment of squashing the topography to conform to a flat surface rather than bulldozing likely contributes to the low-mean misfit for their simulations. Thus, if a numerical model implementation requires a planar top surface and cannot include topography, then the squashing approach of deforming near-surface material in the vertical direction so that the Earth's surface becomes flat and aligned at some elevation appears to be preferable to the bulldozing approach of stripping away all material above some elevation and filling voids below this elevation with a generic material.

For our ground-motion simulations with domains on the order of 100–200 km in size and periods greater than 1–2 sec, attenuation is much less important than accurately capturing the source and sampling the seismic velocity structure. We do not find significantly different misfits for the Aagaard and Dolenc *et al.* numerical models, which do not include attenuation, compared with the Graves and Harmsen *et al.* models that do include attenuation. We expect that attenuation is important at higher frequencies and for larger domains or in regions, such as southern California, where the sedimentary basins are much larger and deeper.

The importance of reflections from the Moho in contributing to strong ground motions in the Loma Prieta earthquake has been both suggested in high-frequency empirical studies (Somerville and Yoshimura, 1990; Campbell, 1991; Catchings and Kohler, 1996) and documented in a low-frequency theoretical study (Stidham *et al.*, 1999). We find similar contributions from critical reflections from the Moho, often designated S_MS, in PGA and PGV at distances of about 60–80 km (e.g., San Francisco) from the rupture. In addition to the simulations discussed earlier that include the upper mantle, Graves constructed an additional short-period simulation that does not include phases reflected from the mantle by explicitly excluding the Moho-reflected rays from the calculation. Harmsen *et al.* also constructed an additional long-period simulation in which the numerical model extends down to only 22 km. By cutting off the model above the top of the mantle in the San Francisco Bay Area (22–29 km), reflections from the Moho are eliminated.

Figure 13 shows that Moho reflections increase ground-motion amplitudes at both short periods (PGA from Graves's broadband simulation) and long periods (PGV from Harmsen *et al.*'s long-period simulation). In general, Moho reflections affect amplitudes at shorter periods more than at longer periods, with increases in PGA averaging about 35% for distances of 60–80 km compared with increases in PGV of 15%, consistent with the findings of earlier empirical studies (Somerville and Yoshimura, 1990; Campbell, 1991; Catchings and Kohler, 1996). In addition, our simulations also indicate that Moho reflections can amplify motions at some sites near the source, which we speculate may be due to finite-source effects. However, the spatially averaged likelihood of amplifications at near-field sites is considerably smaller than it is at greater distances where we expect S_MS reflections.

In addition to the two source models used in this study, several other finite-fault inversions have been constructed for the rupture history of the Loma Prieta earthquake. Emolo and Zollo (2005) discuss the similarities and differences of several models which all assume 1D velocity structure. Liu and Archuleta (2004), on the other hand, compare slip distri-

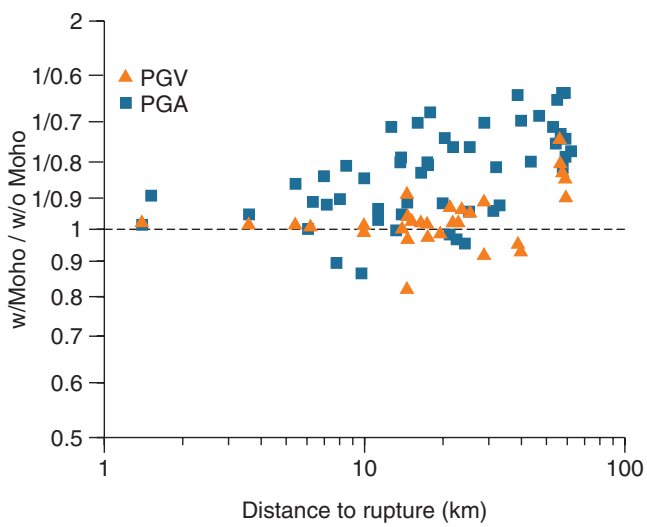

Figure 13. Increase in peak accelerations and peak velocities due to Moho reflections. PGA and PGV ratios are for values from simulations with Moho reflections to values from simulations without Moho reflections. Distance refers to the closest distance to the rupture surface. Moho reflections tend to increase PGA and PGV, especially at distances of about 60–80 km from the rupture.

butions obtained from 1D and 3D velocity structures. They used an earlier version of the USGS Bay Area velocity model (T. M. Brocher, personal comm., 1999). With the 1D structure, they obtained a slip distribution similar to the study of Wald *et al.* (1991), with the northwestern slip patch significantly larger than the one to the southeast of the hypocenter. Using the 3D velocity model, however, they obtained nearly equally weighted slips to the northwest and southeast of the hypocenter. Our analysis of the Loma Prieta earthquake based on ground-motion modeling with the Beroza (1991) and Wald *et al.* (1991) source models embedded in the latest version of the 3D velocity leads to the same conclusion. With further refinement of the seismic velocity model and nonplanar fault geometry from the 3D geologic model, it might be possible to construct a sharper image of the rupture process of this earthquake.

The USGS Bay Area Velocity Model 05.1.0 appears to be a substantial improvement over previous models. Because the model was first constructed as a compressional wave (V_p) model and then converted to a shear-wave (V_s) model, significant effort was expended in the development and testing of empirical relations between V_p and V_s (Brocher, 2005a). A previous USGS 3D seismic velocity model for the Bay Area used a poorly constrained V_p/V_s relationship that yielded shear-wave speeds in the sedimentary basins that were approximately 0.5 km/sec too slow. As a result, that model matched compressional-wave arrival times well but produced shear-wave arrival times that were delayed relative to observations (Fletcher *et al.*, 2003). Forward modeling of ground motions for 12 moderate earthquakes in the Bay Area with the current velocity model generates waveforms with a better match to arrival times and reproduces observed amplitudes, onset times, and waveform shapes significantly better than a 1D seismic velocity model (Rodgers *et al.*, 2008).

In our simulations of the Loma Prieta earthquake, which use the USGS Bay Area Velocity Model 05.1.0, Graves's broadband simulations fit the shaking intensities in the instrumental ShakeMap to within about 1/4 of an MMI unit (18% in PGV) on average with a standard deviation of about 1/2 MMI units (39% in PGV). Our long-period simulations with periods of 1–2 sec and longer reproduce the shaking intensities of the long-period ShakeMap with slightly larger misfits. However, the simulations do provide useful fits in waveform shape and amplitude for periods greater than 2.0 sec at sites across a wide range of azimuths from the source, including GAV, GIL2, LEX, LGPC, SFO, SJIN, and SNJ (Ⓔ see the electronic edition of *BSSA* for waveforms). Thus, periods of 2.0 sec and longer appear to be the bandwidth over which we can generate synthetic waveforms with reasonable matches in amplitude and duration to observations.

Of course, we would like to extend the bandwidth over which we can match recorded waveforms to shorter periods by improving the seismic velocity model. Our results give some clear indications in what regions the model should be improved, including the La Honda basin (especially the area between the Loma Prieta epicenter and Santa Cruz) and the Great Valley Sequence geologic unit in the Livermore–Concord area. The compressional wave speeds for the Great Valley sequence in the current model should be increased in the upper 4 km over that proposed in Brocher (2005a). Data from the San Andreas fault observatory at Depth Main Hole sonic log data support this conclusion with higher compressional wave speeds versus depth than the Brocher (2008) relations. Further detailed analysis using a wide variety of techniques, such as forward modeling of moderately sized local events, construction of finite-frequency Fréchet differential kernels (Zhao *et al.*, 2000; Tromp *et al.*, 2005), and tomographic modeling will help refine the 3D geologic and seismic velocity models. Additionally, our simulations of the Loma Prieta earthquake probe only a portion of the seismic velocity model, so more studies are needed to validate and refine other portions of the model, such as the region north of San Francisco (e.g., Rodgers *et al.*, 2008).

Conclusions

Using kinematic source models of the 1989 magnitude 6.9 Loma Prieta earthquake from Beroza (1991) and Wald *et al.* (1991), our eight ground-motion simulations successfully reproduce the primary spatial variations in shaking intensity associated with rupture directivity and the geologic structure, including sedimentary basins. Our simulations also generate velocity waveforms with reasonable matches to the amplitude and duration of recorded motions at many sites in the period range of 2.0 sec and longer. The four wave-propagation codes give consistent results with the largest differences due to the minimum shear-wave speeds permitted in the simulations and how each group handles topography. For a given period range, finer resolution models with slower shear-wave speeds do a better job of capturing near-surface effects and minimize the misfit in shaking intensities. Similarly, models that honor topography or that retain shallow low-velocity material by squashing topography down to a flat surface outperform models that strip away material by bulldozing material above some given elevation.

We attribute the discrepancies in shaking intensities and waveforms with respect to the observations to errors in the source models and errors in the seismic velocity model (USGS Bay Area Velocity Model 05.1.0). Errors created through interpolation between stations in the ShakeMap may also contribute to the misfit in the intensity values. Consistent with a previous study using an earlier version of the velocity model (Liu and Archuleta, 2004), we find the Beroza source model deficient in energy radiated to the north and the Wald source model deficient in energy radiated to the south. This suggests that a source model with slip distributed relatively equally northwest and southeast of the hypocenter would yield a better fit to the recorded motions. Accounting for the nonplanar geometry of the rupture surface in the source model may also improve the fit to the observed mo-

tions. The 3D velocity model demonstrates significant improvement over previous studies that used simpler velocity models, and our results indicate that fine tuning the velocity structure, especially in the La Honda basin southwest of San Jose and the area east of the Hayward fault associated with the Great Valley Sequence, should improve the ability of ground-motion simulations to fit observed intensities and recorded waveforms in the San Francisco Bay Area. Even with the current version, we can capture shaking intensities, as measured using MMI, to within about $1/2$ of an MMI unit for long-period simulations and about $1/4$ of an MMI unit for broadband simulations. Thus, we find the 3D geologic and seismic velocity models suitable for modeling moderate to large historical and scenario earthquakes in the San Francisco Bay Area.

Acknowledgments

We appreciate David Wald and John Boatwright's many helpful comments and suggestions throughout the course of our modeling effort. Careful reviews by Ralph Archuleta, John Boatwright, Jon Fletcher, and Pencheng Liu led to improvements in the manuscript. We thank Linda Seekins and Howard Bundock for generating the long-period ShakeMap of the Loma Prieta earthquake. Larry Baker provided technical support for Aagaard's simulations using the USGS Menlo Park Beowulf cluster. Aagaard and Harmsen *et al.* were funded by the Earthquake Hazard Program of the U.S. Geological Survey. Dolenc *et al.* acknowledge previous funding support for the Loma Prieta work (USGS Grant Number 1434HQ97GR03091) and for the study of the 3D wave propagation in the Santa Clara Valley (USGS Grant Numbers 99HQGR0057 and 00HQGR0048); both studies laid the foundation for the Dolenc *et al.* ground-motion simulations in this study. Graves was supported by funding from the USGS External Grants Program (06HQGR0132) and the Southern California Earthquake Center (SCEC). The SCEC is funded by National Science Foundation Cooperative Agreement EAR-0106924 and USGS Cooperative Agreement 02HQAG0008. The Graves simulations were run at the University of Southern California Center for High Performance Computing and Communications (www.usc.edu/hpcc, last accessed February 2008). Larsen's work was performed in part under the auspices of the U.S. Department of Energy by University of California, Lawrence Livermore National Laboratory (LLNL) under Contract Number W-7405-Eng-48. This is LLNL contribution UCRL-JRNL-228167. Many of the figures were generated using Generic Mapping Tools (Wessel and Smith, 1998) and the low-pass filtering of the waveforms was performed using SAC2000 (Goldstein *et al.*, 2003).

References

Aagaard, B. T., and T. H. Heaton (2004). Near-source ground motions from simulations of sustained intersonic and supersonic fault rupture, *Bull. Seismol. Soc. Am.* **94,** no. 6, 2064–2078.

Aagaard, B. T., T. M. Brocher, D. Dreger, R. W. Graves, S. Harmsen, S. Hartzell, S. Larsen, K. McCandless, S. Nilsson, N. A. Petersson, A. Rodgers, B. Sjögreen, and M. L. Zoback (2008). Ground-motion modeling of the 1906 San Francisco earthquake, part II: Ground-motion estimates for the 1906 earthquake and scenario events, *Bull. Seismol. Soc. Am.* **98,** no. 2, 1012–1046.

Aagaard, B. T., J. F. Hall, and T. H. Heaton (2001). Characterization of near-source ground motions with earthquake simulations, *Earthq. Spectra* **17,** no. 2, 177–207.

Aagaard, B. T., J. F. Hall, and T. H. Heaton (2004). Effects of fault dip and slip rake angles on near-source ground motions: why rupture directivity was minimal in the 1999 Chi-Chi, Taiwan, earthquake, *Bull. Seismol. Soc. Am.* **94,** no. 1, 155–170.

Anderson, J. G., and S. E. Hough (1984). A model for the shape of the Fourier amplitude spectrum of acceleration at high frequencies, *Bull. Seismol. Soc. Am.* **74,** no. 5, 1969–1993.

Bakun, W. H., and W. H. Prescott (1994). Loma Prieta earthquake professional papers: earthquake occurrence, *U.S. Geol. Surv. Profess. Pap. 1550* (available at http://pubs.usgs.gov/pp/pp1550/, last accessed February 2008).

Beroza, G. C. (1991). Near-source modeling of the Loma Prieta earthquake: evidence for heterogeneous slip and implications for earthquake hazard, *Bull. Seismol. Soc. Am.* **81,** no. 5, 1603–1621.

Boatwright, J., and H. Bundock (2005). Modified Mercalli intensity maps for the 1906 San Francisco earthquake plotted in ShakeMap format, *U.S. Geol. Surv. Open-File Rept. 2005-1135* (available at http://pubs.usgs.gov/of/2005/1135/, last accessed February 2008).

Boatwright, J., H. Bundock, J. Luetgert, L. Seekins, L. Gee, and P. Lombard (2003). The dependence of PGA and PGV on distance and magnitude inferred from northern California ShakeMap data, *Bull. Seismol. Soc. Am.* **93,** no. 5, 2043–2055.

Boore, D. M. (1983). Stochastic simulation of high-frequency ground motions based on seismological models of the radiated spectra, *Bull. Seismol. Soc. Am.* **73,** no. 6A, 1865–1894.

Boore, D. M., and W. B. Joyner (1997). Site amplifications for generic rock sites, *Bull. Seismol. Soc. Am.* **87,** no. 2, 327–341.

Borcherdt, R. D. (1994). Estimates of site-dependent response spectra for design (methodology and justification), *Earthq. Spectra* **10,** no. 4, 617–653.

Brocher, T. M. (2005a). Empirical relations between elastic wavespeeds and density in the Earth's crust, *Bull. Seismol. Soc. Am.* **95,** no. 6, 2081–2092.

Brocher, T. M. (2005b). A regional view of urban sedimentary basins in northern California based on oil industry compressional-wave velocity and density logs, *Bull. Seismol. Soc. Am.* **95,** no. 6, 2093–2114.

Brocher, T. M. (2008). Compressional and shear-wave velocity versus depth relations for common rock types in Northern California, *Bull. Seismol. Soc. Am.* **98,** no. 2, 950–968.

Brocher, T., B. Aagaard, R. Simpson, and R. Jachens (2006). The new USGS 3D seismic velocity model for Northern California (abstract), *Seism. Res. Lett.* **77,** no. 2, 271.

Brune, J. N. (1970). Tectonic stress and spectra of seismic shear waves from earthquakes, *J. Geophys. Res.* **75,** 4997–5009.

California Division of Oil and Gas (1982). Tech. Rept. TR01, Oil and gas prospect wells drilled in California through 1980 (available at www.consrv.ca.gov/DOG/pubs_stats/technical_reports.htm, last accessed February 2008).

Campbell, K. W. (1991). An empirical analysis of peak horizontal acceleration for the Loma Prieta, California, earthquake of 18 October 1989, *Bull. Seismol. Soc. Am.* **81,** no. 5, 1838–1858.

Catchings, R. D., and W. M. Kohler (1996). Reflected seismic waves and their effect on strong shaking during the 1989 Loma Prieta, California, earthquake, *Bull. Seismol. Soc. Am.* **86,** no. 5, 1401–1416.

Catchings, R. D., M. R. Goldman, and G. Gandhok (2006). Structure and velocities of the northeastern Santa Cruz Mountains and the western Santa Clara Valley, California, from the SCSI-LR seismic survey, *U.S. Geol. Surv. Open-File Rept. 2006-1014* (available at http://pubs.usgs.gov/of/2006/1014/, last accessed February 2008).

Catchings, R. D., M. R. Goldman, C. E. Steedman, and G. Gandhok (2004). Velocity models, first-arrival travel times, and geometries of 1991 and 1993 USGS land-based controlled-source seismic investigations in the San Francisco Bay Area, California: in-line shots, *U.S. Geol. Surv. Open-File Rept. 2004-1423* (available at http://pubs.usgs.gov/of/2004/1423/, last accessed February 2008).

Cormier, V. F., and P. Spudich (1984). Amplification of ground motion and waveform complexity in fault zones: examples from the San Andreas and Calaveras fault zones, *Geophy. J. R. Astr. Soc.* **79,** 135–152.

Day, S. M., and C. R. Bradley (2001). Memory-efficient simulation of anelastic wave propagation, *Bull. Seismol. Soc. Am.* **91,** no. 3, 520–531.

Emolo, A., and A. Zollo (2005). Kinematic source parameters for the 1989 Loma Prieta earthquake from the nonlinear inversion of accelerograms, *Bull. Seismol. Soc. Am.* **95,** no. 3, 981–994.

Fletcher, J. B., J. Boatwright, and A. G. Lindh (2003). Wave propagation and site response in the Santa Clara Valley, *Bull. Seismol. Soc. Am.* **93,** no. 1, 480–500.

Frankel, A. (1995). Simulating strong motions of large earthquakes using recordings of small earthquakes: the Loma Prieta mainshock as a test case, *Bull. Seismol. Soc. Am.* **85,** no. 4, 1144–1160.

Frankel, A., and J. Vidale (1992). A three-dimensional simulation of seismic waves in the Santa Clara Valley, California, from a Loma Prieta aftershock, *Bull. Seismol. Soc. Am.* **82,** no. 5, 2045–2074.

Goldstein, P., M. Dodge, D. Firpo, and L. Minner (2003). Signal processing and analysis tools for seismologists and engineers, in *The IASPEI International Handbook of Earthquake and Engineering Seismology*, Academic Press, London.

Graves, R. W. (1996a). Simulating realistic earthquake ground motions in regions of deep sedimentary basins, in *Proceedings of the 11th World Conference on Earthquake Engineering*, Acupulco, Mexico, 23–28 June.

Graves, R. W. (1996b). Simulating seismic-wave propagation in 3-D elastic media using staggered-grid finite-differences, *Bull. Seismol. Soc. Am.* **86,** no. 4, 1091–1106.

Graves, R. W. (2008). The seismic response of the San Bernardino basin region during the 2001 Big Bear Lake earthquake, *Bull. Seismol. Soc. Am.* **98,** no. 1, 241–252.

Graves, R. W., and A. Pitarka (2004). Paper no. 1098, Broadband time history simulation using a hybrid approach, in *13th World Conference on Earthquake Engineering Conference Proceedings*, Vancouver, Canada, 1–6 August.

Hartzell, S., S. Harmsen, A. Frankel, and S. Larsen (1999). Calculation of broadband time histories of ground motion: comparison of methods and validation using strong-ground motion from the 1994 Northridge earthquake, *Bull. Seismol. Soc. Am.* **89,** no. 6, 1484–1504.

Hartzell, S., S. Harmsen, R. A. Williams, D. Carver, A. Frankel, G. Choy, R. C. Jachens, T. M. Brocher, and C. M. Wentworth (2006). Modeling and validation of a 3D velocity structure for the Santa Clara Valley, California, for seismic-wave simulations, *Bull. Seismol. Soc. Am.* **96,** no. 5, 1851–1881.

Hauksson, E., and J. S. Haase (1997). Three-dimensional Vp and Vp/Vs velocity models of the Los Angeles basin and central Transverse Ranges, California, *J. Geophys. Res. Solid Earth* **012,** no. B3, 5423–5454.

Holzer, T. H. (1994). Loma Prieta Earthquake Professional Papers: Strong ground motion and ground failure, *U.S. Geol. Surv. Profess. Pap. 1551* (available at http://pubs.usgs.gov/pp/pp1551/, last accessed February 2008).

Jachens, R., R. Simpson, R. Graymer, C. Wentworth, and T. Brocher (2006). Three-dimensional geologic map of northern and central California: a basin model for supporting earthquake simulations and other predictive modeling (abstract), *Seism. Res. Lett.* **77,** no. 2, 270.

Kagawa, T., K. Irikira, and P. G. Somerville (2004). Differences in ground motion and fault rupture process between the surface and buried rupture earthquakes, *Earth Planets Space* **56,** no. 1, 3–14.

Larsen, S., and C. A. Schultz (1995). Tech. Rept. UCRL-MA-121792, Elas3d: 2D/3D elastic finite-difference wave propagation code, Lawrence Livermore National Laboratory, 19 pp.

Lawson, A. (Editor) (1908). The California earthquake of April 18, 1906, report of the State Earthquake Investigation Commission, Carnegie Institution of Washington, Washington, D.C..

Lemoine, F. G., S. C. Kenyon, J. K. Factor, R. G. Trimmer, N. K. Pavlis, D. S. Chinn, C. M. Cox, S. M. Klosko, S. B. Luthcke, M. H. Torrence, Y. M. Wang, R. G. Williamson, E. C. Pavlis, R. H. Rapp, and T. R. Olson (1998). NASA Tech. Rept. NASA/TP-1998-206861, The development of the joint NASA GSFC and the National Imagery and Mapping Agency (NIMA) geopotential model EGM96, NASA Goddard Space Flight Center, Greenbelt, Maryland.

Liu, P., and R. J. Archuleta (2002). The effect of a low-velocity surface layer on simulated ground motion (abstract), *Seism. Res. Lett.* **73,** no. 2 (SSA Annual Meet.), 267.

Liu, P., and R. J. Archuleta (2004). A new nonlinear finite fault inversion with three-dimensional Green's functions: application to the 1989 Loma Prieta, California, earthquake, *J. Geophys. Res.* **109,** B02318, doi 10.1029/2003JB002625.

Liu, P., and R. J. Archuleta (2006). Efficient modeling of Q for 3D numerical simulation of wave propagation, *Bull. Seismol. Soc. Am.* **96,** no. 4A, 1352–1358.

Los Alamos National Laboratory (2005). Los Alamos grid toolbox LaGriT, http://lagrit.lanl.gov (last accessed February 2008).

Magistrale, H., K. McLaughlin, and S. Day (1996). A geology-based 3-D velocity model of the Los Angeles basin sediments, *Bull. Seismol. Soc. Am.* **86,** no. 4, 1161–1166.

McCulloch, D. S. (1987). Regional geology and hydrocarbon potential of offshore central California, in *Geology and Resource Potential of the Continental Margin of Western North America and Adjacent Ocean Basins: Beaufort Sea to Baja California*, Vol. **6**, Circum-Pacific Council for Energy and Mineral Resources, Earth Science Series, American Association of Petroleum Geologists, Houston, Texas, 353–401.

McPhee, D. K., V. E. Langenheim, S. Hartzell, R. J. McLaughlin, B. T. Aagaard, R. C. Jachens, and C. McCabe (2007). Basin structure beneath the Santa Rosa Plain, northern California: implications for damage caused by the 1969 Santa Rosa and 1906 San Francisco earthquakes, *Bull. Seismol. Soc. Am.* **97**, 1449–1457.

Meltzer, A. S., A. R. Levander, and W. D. Mooney (1987). Upper crustal structure, Livermore Valley and vicinity, California coast ranges, *Bull. Seismol. Soc. Am.* **77,** no. 5, 1655–1673.

Olsen, K. B., and R. J. Archuleta (1996). Three-dimensional simulation of earthquakes on the Los Angeles fault system, *Bull. Seismol. Soc. Am.* **86,** no. 3, 575–596.

Olsen, K. B., S. M. Day, and C. R. Bradley (2003). Estimation of Q for long-period (>2 sec) waves in the Los Angeles basin, *Bull. Seismol. Soc. Am.* **93,** no. 2, 627–638.

Parsons, T., R. Sliter, E. L. Geist, R. C. Jachens, B. E. Jaffe, A. Foxgrover, P. E. Hart, and J. McCarthy (2003). Structure and mechanics of the Hayward-Rodgers Creek fault step-over, San Francisco Bay, California, *Bull. Seismol. Soc. Am.* **93,** no. 5, 2187–2200.

Piatanesi, A., E. Tinti, M. Cocco, and E. Fukuyama (2004). The dependence of traction evolution on the earthquake source time function adopted in kinematic rupture models, *Geophys. Res. Lett.* **31,** L04609, doi 10.1029/2003GL019225.

Rodgers, A., N. A. Petersson, S. Nilsson, B. Sjogreen, and K. McCandless (2008). Broadband waveform modeling of moderate earthquakes in the San Francisco Bay Area and preliminary assessment of the USGS 3D seismic velocity model, *Bull. Seismol. Soc. Am.* **98,** no. 2, 969–988.

Satoh, T. (2006). Inversion of Qs of deep sediments from surface-to-borehole spectral ratios considering obliquely incident SH and SV waves, *Bull. Seismol. Soc. Am.* **96,** no. 3, 943–956.

Somerville, P., and J. Yoshimura (1990). The influence of critical Moho reflections on strong ground motions recorded in San Francisco and Oakland during the 1989 Loma Prieta earthquake, *Geophys. Res. Lett.* **17,** no. 8, 1203–1306.

Somerville, P. G., K. Irikura, R. Graves, S. Sawada, D. Wald, N. Abrahamson, Y. Iwasaki, T. Kagawa, N. Smith, and A. Kowada (1999). Characterizing crustal earthquake slip models for the prediction of strong ground motion, *Seism. Res. Lett.* **70,** no. 1, 199–222.

Stanley, R. G. (1985). Middle Tertiary sedimentation and tectonics of the La Honda basin, central California, *U.S. Geol. Surv Open-File Rept. 85-596* 263 pp.

Stidham, C., M. Antolik, D. Dreger, S. Larsen, and B. Romanowicz (1999). Three-dimensional structure influences on the strong-motion wave-

field of the 1989 Loma Prieta earthquake, *Bull. Seismol. Soc. Am.* **89,** no. 5, 1184–1202.

Tromp, J., C. Tape, and Q. Liu (2005). Seismic tomography, adjoint methods, time reversal and banana-doughnut kernels, *Geophys. J. Int.* **160,** no. 1, 195–216.

U.S. Geological Survey Staff (1990). The Loma Prieta, California, earthquake: an anticipated event, *Science* **247,** no. 4940, 286–293.

Wald, D. J., and R. W. Graves (1998). The seismic response of the Los Angeles basin, California, *Bull. Seismol. Soc. Am.* **88,** no. 2, 337–356.

Wald, D. J., D. V. Helmberger, and T. H. Heaton (1991). Rupture model of the 1989 Loma Prieta earthquake from the inversion of strong-motion and broadband teleseismic data, *Bull. Seismol. Soc. Am.* **81,** no. 5, 1540–1572.

Wald, D., B. Worden, V. Quitoriano, and K. Pankow (2005). *ShakeMap Manual: Technical Manual, Users Guide, and Software Guide* (Version 1.0 Ed.). U.S. Geol. Surv. (available at http://pubs.usgs.gov/tm/2005/12A01/, last accessed February 2008).

Wentworth, C. M., G. R. Fisher, P. Levine, and R. C. Jachens (1995). The surface of crystalline basement, Great Valley and Sierra Nevada, California: a digital map database, *U.S. Geol. Surv. Open-File Rept. 95-96*.

Wessel, P., and W. H. F. Smith (1998). New, improved version of the Generic Mapping Tools released, *EOS* **79,** 579.

Wills, C. J., M. Petersen, W. A. Bryant, M. Reichle, G. J. Saucedo, S. Tan, G. Taylor, and J. Treiman (2000). A site-conditions map for California based on geology and shear-wave velocity, *Bull. Seismol. Soc. Am.* **90,** no. 6B, S187–S208.

Zhao, L., T. H. Jordan, and C. H. Chapman (2000). Three-dimensional Fréchet differential kernels for seismic delay times, *Geophys. J. Int.* **141,** no. 3, 558–576.

U.S. Geological Survey
MS977, 345 Middlefield Road
Menlo Park, California 94025
(B.T.A., T.M.B., M.L.Z.)

Seismological Laboratory
University of California, Berkeley
215 McCone Hall
Berkeley, California 94720
(D.D., D.D.)

URS Corporation
566 El Dorado Strett
Pasadena, California 91101
(R.W.G.)

U.S. Geological Survey
MS966, P.O. Box 25046
Golden, Colorado 80225
(S.H., S.H.)

Lawrence Livermore National Laboratory
Box 808, L-103
Livermore, California 94551-0808
(S.L.)

Manuscript received 7 March 2007

Bulletin of the Seismological Society of America, Vol. 98, No. 2, pp. 1012–1046, April 2008, doi: 10.1785/0120060410

Ⓔ

Ground-Motion Modeling of the 1906 San Francisco Earthquake, Part II: Ground-Motion Estimates for the 1906 Earthquake and Scenario Events

by Brad T. Aagaard, Thomas M. Brocher, David Dolenc, Douglas Dreger, Robert W. Graves, Stephen Harmsen, Stephen Hartzell, Shawn Larsen, Kathleen McCandless, Stefan Nilsson, N. Anders Petersson, Arthur Rodgers, Björn Sjögreen, and Mary Lou Zoback

Abstract We estimate the ground motions produced by the 1906 San Francisco earthquake making use of the recently developed Song *et al.* (2008) source model that combines the available geodetic and seismic observations and recently constructed 3D geologic and seismic velocity models. Our estimates of the ground motions for the 1906 earthquake are consistent across five ground-motion modeling groups employing different wave propagation codes and simulation domains. The simulations successfully reproduce the main features of the Boatwright and Bundock (2005) ShakeMap, but tend to over predict the intensity of shaking by 0.1–0.5 modified Mercalli intensity (MMI) units. Velocity waveforms at sites throughout the San Francisco Bay Area exhibit characteristics consistent with rupture directivity, local geologic conditions (e.g., sedimentary basins), and the large size of the event (e.g., durations of strong shaking lasting tens of seconds). We also compute ground motions for seven hypothetical scenarios rupturing the same extent of the northern San Andreas fault, considering three additional hypocenters and an additional, random distribution of slip. Rupture directivity exerts the strongest influence on the variations in shaking, although sedimentary basins do consistently contribute to the response in some locations, such as Santa Rosa, Livermore, and San Jose. These scenarios suggest that future large earthquakes on the northern San Andreas fault may subject the current San Francisco Bay urban area to stronger shaking than a repeat of the 1906 earthquake. Ruptures propagating southward towards San Francisco appear to expose more of the urban area to a given intensity level than do ruptures propagating northward.

Online Material: Source models, synthetic and observed displacements, modified Mercalli intensities, maps of SA and PGA, velocity waveforms, and movies of simulated wave propagation.

Introduction

The 18 April 1906 magnitude 7.9 San Francisco earthquake ruptured the San Andreas fault for nearly 500 km with a mean slip of 4–5 m (Thatcher *et al.*, 1997; Song *et al.*, 2008). The occurrence and subsequent scientific investigation of this earthquake marked the birth of modern earthquake science in the United States. For the first time, a large earthquake and its effects were systematically documented, and the shaking was properly interpreted as resulting from slip on an active fault and as part of a recurring tectonic process of strain accumulation and release (Lawson, 1908). To commemorate the centennial of the 1906 earthquake (Zoback, 2006), a 2-yr collaborative effort was launched to recreate the strong ground motion produced by this event and the 1989 magnitude 6.9 Loma Prieta earthquake. By utilizing modern computational methods and taking advantage of new data and constraints, we are able to characterize both the amplitude and duration of shaking in 1906 across central and northern California. Aagaard *et al.* (2008) discusses our efforts to validate the 3D geologic and seismic velocities models used in this study with data from the 1989 Loma Prieta earthquake.

The 1906 earthquake was felt throughout California, in southern Oregon, and as far east as central Nevada. It also wrote the first useful strong-motion record, a three-component seismograph from a duplex pendulum recording at Mount Hamilton, about 90 km from the epicenter.

More than 600 detailed reports of shaking intensity and damage were compiled in the two-volume landmark document, *The Report of the State Earthquake Investigation Commission*. Volume I was edited by A. Lawson and was published in 1908 (Lawson, 1908), and volume II was edited by H. F. Reid and was published in 1910 (Reid, 1910). Hereafter, we will refer to the report using the volume number as appropriate.

Based on these data, the commission investigators concluded that, in general, shaking intensity diminished with distance from the fault. They also recognized the importance of site effects, noting that the "amount of damage produced by the earthquake …depended chiefly on the geological character of the ground" (H. O. Wood, vol. I, p. 241), and, in particular, commented that "areas that suffered most severely were those upon filled ground" (vol. I, p. 253). H. F. Reid applied elasticity theory to extend the application of F. J. Rogers's vibrating sand box experiments (vol. I, pp. 326–335). Reid properly concluded that (1) the response of basins depended on their size relative to the wavelength of the seismic waves, (2) in large basins, internal reflections could result in increased amplification (vol. II, p. 54), and (3) variations in amplitude within and between large basins were related to "differences in the character and depth of the alluvium" (vol. II, p. 56). Our ground-motion modeling results demonstrate all of these effects, indicating the robustness of these early observations, modeling, and interpretations.

Reid (vol. II, p. 11) used four local timing observations of ground shaking and an assumed crustal velocity to compute a least-squares hypocenter located near Olema, the site of the largest recorded surface displacement. Bolt (1968) showed that a hypocenter 50 km to the southwest, coincident with the 22 March 1957 magnitude 5.3 Daly City earthquake, could satisfy both the local observations as well as teleseismic *P* and *S* recordings, although he could not preclude Reid's Olema location. Boore (1977) interpreted phases in the sole strong-motion recording at Mt. Hamilton to constrain the epicentral location to lie somewhere offshore from San Francisco and likely much farther south than the previously presumed epicenter near Olema. More recently, Lomax (2005) reevaluated the arrival-time observations and applied modern event-location techniques to determine a maximum-likelihood hypocenter of 37.78° N, 122.51° W at a depth of around 12 km. Wald *et al.* (1993) combined the preserved teleseismic records with empirical Green's functions to construct a finite-source model for the 1906 earthquake; however, the slip distribution differs markedly from the one Thatcher *et al.* (1997) developed based on triangulation surveys. A new source model (Song *et al.*, 2008) that combines both datasets resolves many of the discrepancies between the two.

In the last few decades several studies have attempted to characterize the ground motions in the 1906 earthquake. Borcherdt and Gibbs (1976) combined modern site-response data with intensity mapping in Lawson (1908) to estimate the variability in response for various geologic units and quantify the dependencies of the 1906 shaking intensities with distance from the rupture and site conditions. Anooshehpoor *et al.* (1999) calculated a lower bound for the peak acceleration of about 1*g* at frequencies less than 2 Hz at the Point Reyes train station based, in part, on the conductor's description of the ground motions that overturned the train, as documented in Lawson (1908). Ward (2000) combined a quasi-static model of the 1906 earthquake and modified whole-space Green's functions with the geodetic slip model from Thatcher *et al.* (1997) to compute a very rough estimate of the variability of shaking. The simulated ground motions were limited to a few stations and included directivity, but not 2D or 3D Earth structure. As a result, these simulations fail to capture the dynamics (i.e., rise time) of the source. None of these studies provide a regional perspective of the spatial variations in the intensity, duration, and character of the ground motions.

Boatwright and Bundock (2005) constructed a ShakeMap for the 1906 earthquake (Fig. 1) by carefully examining more than 600 reports of shaking and damage compiled in Lawson (1908) and reinterpreting them in terms of the modern Modified Mercalli Intensity (MMI) scale. This ShakeMap provides a comprehensive picture of the shaking intensities and serves as the primary independent constraint for our ground-motion simulations. Shaking intensities, such as

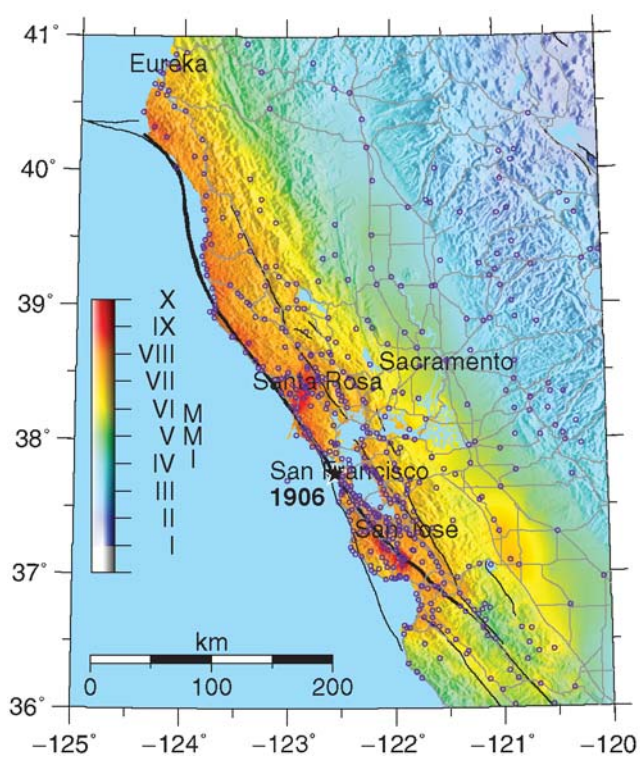

Figure 1. ShakeMap for the 1906 San Francisco earthquake based on the Boatwright and Bundock (2005) intensities (processed 18 October 2005). Open circles identify the intensity sites used to construct the ShakeMap.

those in ShakeMap, however, lack information about the duration and character of the ground motion.

Our ground-motion simulations utilize up-to-date information on the 3D crustal structure and our experience in generating realistic kinematic source models to produce ground-motion time histories over the San Francisco Bay Area and the surrounding region extending more than 500 km along the San Andreas fault. We also investigate the variability in ground motions for similarly sized events on this portion of the San Andreas fault due to changes in the hypocenter, rupture directivity, and differences in the distribution of slip. Instead of focusing on a particular geologic structure (e.g., one of the sedimentary basins) or geographic location (e.g., San Francisco), we examine ShakeMaps displaying the spatial distributions of shaking over the San Francisco Bay Area and entire rupture extent as well as velocity time histories at a number of sites. We also estimate the relative impact each scenario would have on today's infrastructure in the context of the analysis by Kircher *et al.* (2006), who calculated the expected impact of a repeat of the 1906 earthquake.

Methodology

For our ground-motion modeling of the 1906 earthquake, we use the Song *et al.* (2008) source model, which uses both teleseismic records and triangulation surveys to constrain the slip distribution, and teleseismic records to constrain the rupture speed. Even with these combined datasets, many important details and source parameters are missing from the rupture model. We fill in the missing details, such as short-length scale variations in slip and rise time, based on empirical observations and parameter searches in which we attempt to fit the Boatwright and Bundock (2005) shaking intensities. Given the large uncertainty in the source parameters, we employed five different ground-motion modeling groups to search the parameter space and constrain the missing details, yielding our preferred source model for generating strong ground motions from the 1906 earthquake.

Wave-Propagation Codes

The five ground-motion modeling groups include (1) Aagaard, (2) Graves, (3) Harmsen *et al.* (consisting of Harmsen and Hartzell), (4) Larsen *et al.* (consisting of Larsen, Dreger, and Dolenc), and (5) Petersson *et al.* (consisting of Petersson, Rodgers, McCandless, Nilsson, and Sjögreen). Each group employs a different modeling code to solve the elastic-wave equation. Four of these codes (Larsen and Schultz, 1995; Graves, 1996; Aagaard *et al.*, 2001; Liu and Archuleta, 2002) were used in our efforts to model the Loma Prieta earthquake (Aagaard *et al.*, 2008). The other one, called the wave propagation project (WPP), used by Petersson *et al.* and developed by Nilsson *et al.* (2007), relies on node-centered (nonstaggered) finite differences with a displacement formulation to discretize the elastic-wave equation.

Table 1 gives the sizes and various features of the domains for the ground-motion simulations. Simulating wave propagation through the 3D structure in the volume surrounding the entire rupture length of the 1906 earthquake at periods of 1–2 sec and longer requires extensive computational resources. As a result, Aagaard and Harmsen *et al.* model only portions of the rupture, whereas the domains for Graves, Larsen *et al.*, and Petersson *et al.* cover the entire rupture as shown in Figure 2. Many of the features and parameters match those used in modeling the Loma Prieta earthquake, including the use of a recently developed 3D geologic model (Jachens *et al.*, 2006) and the seismic velocity model, U.S. Geological Survey Bay Area Velocity Model 05.1.0 (USGS 05.1.0) (Brocher, 2005, 2008). Some notable exceptions include the bounding boxes of the domains of the Graves and Larsen *et al.* modeling groups and the inclusion of topography and attenuation in the Larsen *et al.* simulations.

Because the 3D geologic and seismic velocity models include topography, the ground-motion simulations must account for it when querying the velocity model for material properties. The finite-difference wave-propagation codes that do not include topography directly either bulldoze the surface of the Earth by stripping away any material above some elevation and filling in voids below this elevation with some generic material, or they squash the surface of the Earth by deforming the near-surface material in the vertical direction so that the free surface is flat and aligned at some elevation. The bulldozing method tends to remove shallow, low-velocity layers but retains the geometry of the geologic units, whereas squashing includes shallow, low-velocity layers but tends to distort the geometry of the geologic units. Graves and Petersson *et al.* employ variations of the bulldozing approach: Petersson *et al.* include water while Graves fills areas below sea level with a generic sediment ($V_p = 2200$ m/sec, $V_s = 760$ m/sec, density $= 2100$ kg/m^3). Harmsen *et al.* employ the squashing approach. Our simulations of the Loma Prieta earthquake (Aagaard *et al.*, 2008) indicate that including topography is the preferred approach, followed by squashing and then bulldozing. Bulldozing often removes shallow, low-velocity layers that are important for capturing basin effects.

Another difference with respect to the Loma Prieta simulations is that in this study, the Graves, Larsen *et al.*, and Petersson *et al.* domains extend well beyond the boundaries of the detailed portion of the velocity model and into the coarser resolution regional portion as shown in Figure 2. While there is a smooth transition from the detailed portion to the regional portion, the regional portion contains only the major geologic units (mantle, mafic lower crust, major Mesozoic units, and a representation of the Great Valley fill). As a result, we expect to capture much less detail in the spatial distribution of shaking and the waveforms in the areas of the simulation domains that lie in the regional portion of the velocity model.

Table 1

Wave Propagation Codes and Modeling Domains

	Aagaard	Graves	Harmsen *et al.*	Larsen *et al.*	Petersson *et al.*
Domain					
Length	250 km	555 km	128 km	630 km	550 km
Width	110 km	162 km	52 km	320 km	200 km
Maximum depth	40 km	45 km	31 km	55 km	40 km
Northwest corner	−123.7083, 38.2832	−125.5000, 40.2000	−122.7313, 37.6313	−126.2037, 39.6589	−125.4990, 40.0440
Northeast corner	−122.7002, 38.8944	−123.9482, 41.0505	−122.3116, 37.9610	−123.2940, 41.3485	−123.6000, 41.1000
Southeast corner	−121.0208, 37.0716	−120.2911, 36.9623	−121.2978, 37.1331	−119.0100, 36.7700	−119.9590, 37.1030
Southwest corner	−122.0180, 36.4894	−121.8528, 36.1118	−121.7173, 36.8069	−121.8819, 35.0804	−121.8060, 36.0470
Projection	None (3D Earth)	Spheroidal	Ellipsoid transverse Mercator	Spheroidal	Spheroidal
Discretization	Unstructured FE	Staggered-grid FD	Staggered-grid FD	Staggered-grid FD	Node-centered FD
Space	second order	fourth order	fourth order	fourth order	second order
Time	second order	second order	second order	second order	second order
Resolution	variable	150 m	50 m, 150 m	100 m	125 m
Bandwidth	$T > 2.0$ sec	$T > 1.0$ sec	$T > 1.0$ sec	$T > 1.0$ sec	$T > 2.0$ sec
Minimum V_s	700 m/sec	760 m/sec	330 m/sec	500 m/sec	500 m/sec
Features					
Topography	Yes	Bulldozed	Squashed	Yes	Bulldozed
Water	Air filled	Sediment filled	Excluded	Included	Included
Material properties	USGS 05.1.0	USGS 05.1.0	USGS 05.1.0	USGS 05.1.0	USGS 05.1.0
Attenuation	No	Graves	Graves	USGS 05.1.0	No
Earthquake source	Offset in mesh	Point sources	Point sources	Point sources	Point sources
Number of point sources	N/A	6084	1200–1400	6084	12,313 (SongMod)
Fault surface	3D geologic model	3D geologic model	3D geologic model	3D geologic model	3D geologic model

The corners of the bounding boxes of each domain are given in longitude and latitude (World Geodetic System 1984 [WGS84] horizontal datum).

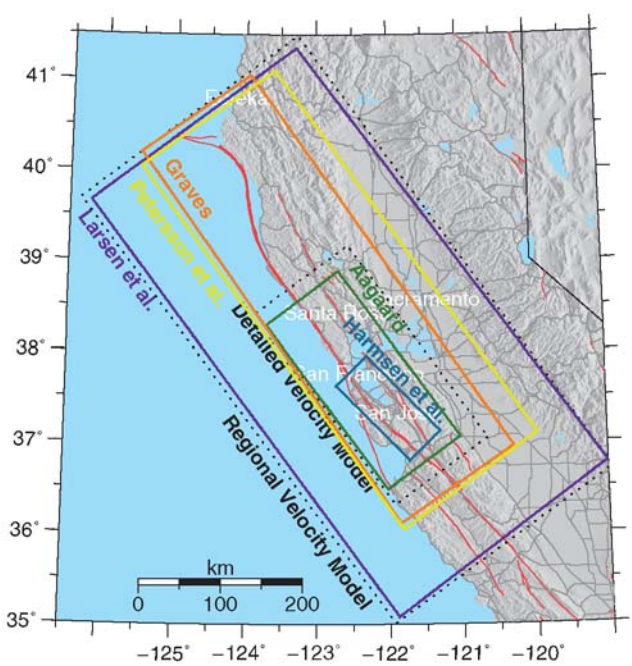

Figure 2. Bounding boxes of the domains used by the five ground-motion modeling groups and the detailed and regional portions of the USGS 05.1.0. The thick red line shows the portion of the San Andreas fault that ruptured in 1906, and the thin red lines delineate the surface traces of major faults in the region.

All of the ground-motion simulations use the fault geometry of the San Andreas fault from the 3D geologic model. For the four finite-difference wave-propagation codes in which the earthquake rupture is implemented with point sources, we discretize the fault surface into a 1-km uniform resolution logically rectangular grid (i.e., a grid in along-strike and down-dip coordinates) that conforms to the nonplanar geometry of the continuous surface. Aagaard's simulations incorporate the fine-resolution triangulated surface as an interior interface in the finite-element mesh, with the same Laplacian smoothing of the vertex coordinates that was used in the Loma Prieta modeling (Aagaard *et al.*, 2008).

The domains for each of the finite-difference wave propagation codes employ a projected coordinate system. Graves, Larsen *et al.*, and Petersson *et al.* all use simple spheroidal projections, whereas Harmsen *et al.* use an ellipsoidal transverse Mercator projection. Aagaard's finite-element model conforms to the 3D geometry of the Earth so it does not use a projected coordinate system. The differences in geometry among the domains as a result of the projection or lack thereof are small and do not significantly contribute to any noticeable differences among the synthetic ground motions.

Including Short-Period Energy

Graves extended his simulations to shorter periods using the same hybrid procedure as he did for the Loma Prieta simulations (Aagaard *et al.*, 2008). The hybrid procedure generates broadband ground motions, in this case

$T > 0.1$ sec, by combining stochastic modeling at short periods (0.1 sec $< T <$ 1 sec) with the deterministic modeling (described in the previous section) at long periods ($T >$ 1 sec). The short-period simulation methodology sums the response for each subfault assuming a random phase, an omega-squared source spectrum, and simplified 1D Green's functions. The modeling technique also applies site corrections across all periods to account for near-surface, period-dependent, nonlinear site effects.

Source Models

In addition to adapting the Song *et al.* source model for use in our strong ground-motion simulations of the 1906 earthquake, we also constructed source models for seven hypothetical scenarios in order to characterize the potential variability in ground motions for future events of this size on the northern San Andreas fault. Table 2 gives the label of each of the scenarios, along with the names of the corresponding slip models and hypocenters. Three of these are simply perturbations from our adapted Song *et al.* model with different hypocenters. The other four scenarios use distributions of slip and rupture speed that are significantly different from that in the Song *et al.* source model but use the 1906 hypocenter and the same three hypothetical hypocenters.

Slip-Time Function

In each of the source models, we employ the same slip-time function that we used in our Loma Prieta simulations Aagaard *et al.* (2008). The slip-time history follows the integral of Brune's far-field time function (Brune, 1970):

$$D(t) = D_{\text{final}}\left[1 - e^{-t/t_0}\left(1 + \frac{t}{t_0}\right)\right], \tag{1}$$

$$t_0 = \frac{D_{\text{final}}}{eV_{\max}}, \tag{2}$$

Table 2
Description of Earthquake Simulations

Simulation Label	Slip Distribution	Hypocenter
Song	Song	1906
SongMod	SongMod	1906
SongModHypoN	SongMod	Rockport
SongModHypoC	SongMod	Bodega Bay
SongModHypoS	SongMod	San Juan Bautista
RandomHypo06	Random	1906
RandomHypoN	Random	Rockport
RandomHypoC	Random	Bodega Bay
RandomHypoS	Random	San Juan Bautista

The Song slip distribution produces a moment magnitude 7.9 event (average slip is 4.3 m), whereas the SongMod and Random slip distributions produce moment magnitude 7.8 events (average slip is 3.0 m). Hypocenter locations are given in Table 3.

$$V_{\max}[\text{m/sec}] = C_{\text{tr}}\sqrt{D_{\text{final}}[m]}, \tag{3}$$

$$C_{\text{tr}} = \begin{cases} 0.6 & z \geq 0 \text{ km}, \\ -0.12z + 0.6 & -5.0 \text{ km} < z < 0 \text{ km}, \\ 1.2 & z \leq -5.0 \text{ km}, \end{cases} \tag{4}$$

where $D(t)$ is the slip as a function of time, D_{final} is the final slip at a point, t_0 is a time constant, $V_{\max}$ is the peak slip rate, C_{tr} is a constant that controls the rise time, and z is the elevation with respect to sea level in kilometers. We chose this slip-time function because its asymmetric shape is compatible with slip-time histories produced by spontaneous rupture models with slip-weakening friction (e.g., Guatteri *et al.*, 2003 and Piantanesi *et al.*, 2004). The rise time (the time it takes for 95% of the slip to occur, t_{95}) for this slip-time function, which is given by

$$t_{95} = 1.745\frac{D_{\text{final}}}{V_{\max}}, \tag{5}$$

where

$$D(t_{95}) = 0.95D_{\text{final}} \tag{6}$$

is in the range of 3–4 sec for slip in the range of 4–8 m when $C_{\text{tr}} = 1.2$. These rise times are consistent with the expressions for rise times in kinematic source inversions (Somerville *et al.*, 1999) extrapolated to events of this size. We lengthen the rise time near the surface (equation 4) based on preliminary simulations with the Song model, in which longer rise times in the near-surface region improved the fit to the Boatwright and Bundock intensities, and on empirical observations of longer rise times for large surface rupture (Kagawa *et al.*, 2004).

Adapting the Song *et al.* Model

The Song *et al.* source model uses a hypocenter a few kilometers offshore from San Francisco consistent with both the geometry of the San Andreas fault in the 3D geologic model and the Lomax (2005) probability analysis. This yields a hypocenter of 122.557° W, 37.75° N, and a depth of 10 km. As mentioned earlier, the Song *et al.* source model only contains slip variations at long-length scales and a gross estimate of the rupture speed. The source model specifies slip on 10-km along-strike and 12-km down-dip patches, with the average rupture speed determined over portions ranging in length from 40 to 120 km. The first 120 km of rupture north of the hypocenter propagates faster than the shear-wave speed before dropping below the shear-wave speed for the remaining northward propagation. The inversion resolves neither the slip-time function nor slip rise time. In order to accurately estimate the ground motions in the period range of interest (about 1–2 sec and longer), our ground-motion simulations require a finer-scale resolution of the rupture properties, which necessitated incorporating additional infor-

mation and making several small adjustments to the Song *et al.* source model.

We taper the rupture speed in the upper 5 km of the fault to be 60% of the original Song *et al.* value. This modification follows from both variations in rupture speed associated with slower shear-wave speeds in the top few kilometers of the crust and associating relatively slower ruptures speeds with the observations of longer rise times in near-surface regions for large events with surface rupture (e.g., Kagawa *et al.*, 2004). Figure 3 shows the distributions of slip with contours of slip initiation time for this source model (hereafter referred to as Song). Thus, the Song source model is identical to the Song *et al.* source model except for a slower rupture speed over the top 5 km of the fault.

We construct the SongMod source model to add shorter-length scale variations in slip based upon insight from previous studies of strong ground motions and to improve the fit between the synthetic and Boatwright and Bundock intensities. The randomly phased, shorter-length scale-slip variations follow a wavenumber-squared falloff consistent with studies of kinematic source inversions (Somerville *et al.*, 1999; Mai and Beroza, 2002). The form of the wavenumber filter applied to the slip distribution is given by

$$A(k) = C(1 + k_0^4)^{-1/2}, \tag{7}$$

$$k_0^2 = k_x^2 x_L^2 + k_y^2 y_L^2, \tag{8}$$

where k_0 is the normalized wavenumber, C is a scaling factor to give the correct seismic moment, and x_L and y_L are correlation lengths (inverse of wavenumber corners) given by

$$\log_{10} x_L = \log_{10} y_L = 0.5M_{\mathrm{w}} - 2. \tag{9}$$

This relation for the correlation lengths is a generalization of the expression given in Somerville *et al.* (1999). It is similar to the circular averaged correlation length determined by Mai and Beroza (2002), as well as the relation for characteristic subevent size (interpreted to be asperity size) found by Beresnev and Atkinson (2001). From equation (9), the correlation lengths for moment magnitude 7.8 and 7.9 events are 79 and 89 km, respectively. In order to preserve the long wavelength features of the original model, no filtering is applied at wavelengths greater than 20 km.

We also incorporate local variations in rupture speed based on observations that ruptures tend to propagate faster in regions with larger slip as seen in spontaneous rupture models (e.g., Day, 1982) and inferred from source inversions of past earthquakes (e.g., Yaji, 2004). We adjust the slip initiation times according to

$$t_r = t_{\mathrm{orig}} - t_{\mathrm{shift}}(\mathrm{slip}), \tag{10}$$

where t_r is the slip initiation time, t_{orig} is the slip initiation time given by the Song model, and $t_{\mathrm{shift}}(\mathrm{slip})$ is a timing perturbation that scales linearly with slip amplitude such that

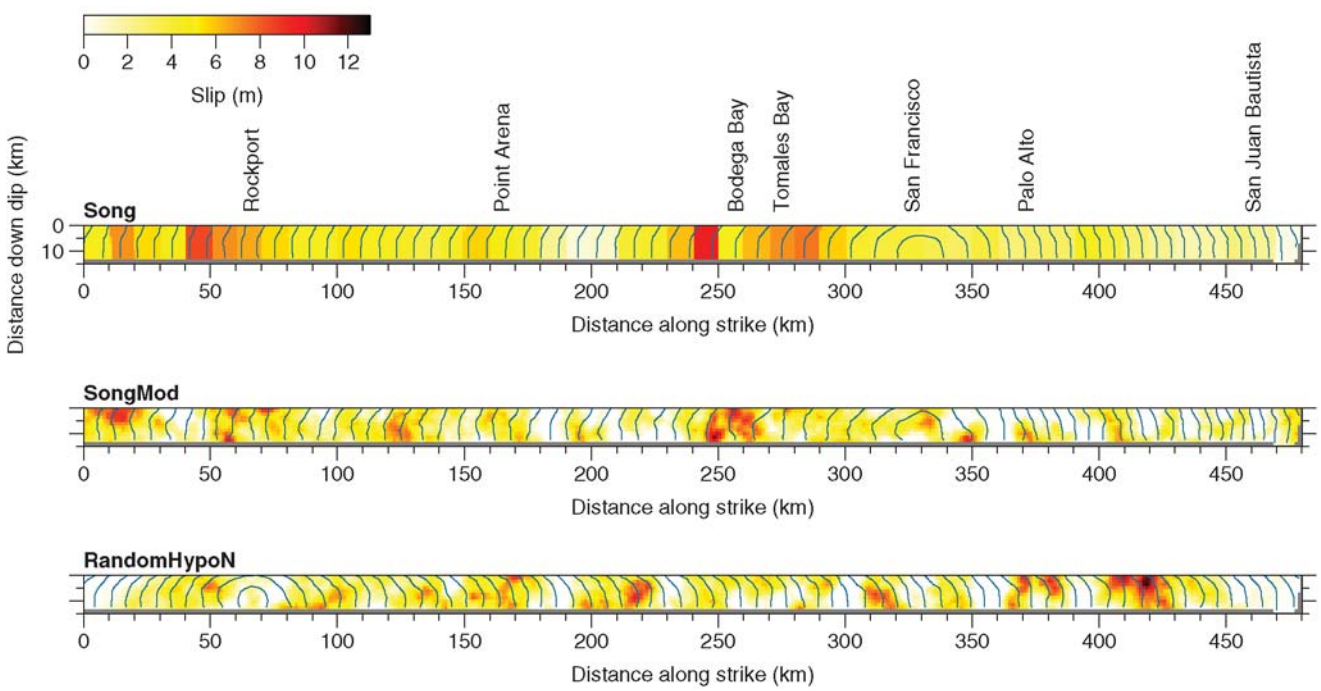

Figure 3. Source models for three of the scenarios. The top panel shows the Song source model, the middle panel the SongMod source model, and the bottom panel the RandomHypoN source model (Rockport epicenter). The colors depict the magnitude of right-lateral slip, and the contours show slip-initiation time (contour interval is 2.0 sec). The nonplanar fault geometry has been mapped onto a rectangular grid for plotting purposes.

$t_{\text{shift}} = 1.0$ sec at the location of maximum slip and $t_{\text{shift}} = 0$ at locations where the slip is equal to the average value. The prescribed value of t_{shift} is based on modeling of past earthquakes (e.g., Graves and Pitarka, 2004) and on theoretical analyses (e.g., Hisada, 2001).

In addition to these modifications necessary to make the source model more suitable for ground-motion modeling, we also alter the model to improve the match between the synthetic and Boatwright and Bundock intensities. Because the rupture length is relatively well constrained, and small perturbations in the rupture width and rise time did not provide a significant improvement in fit with the Boatwright and Bundock intensities in preliminary simulations, we chose to reduce the average slip from 4.3 to 3.0 m and to make a few small perturbations to the large-length scale distributions of slip and rupture speed. The smaller average slip results in a moment-magnitude 7.8 event compared to a moment-magnitude 7.9 event. In a later section, we will return to this issue of how to adjust the Song source model to better fit the Boatwright and Bundock intensities using more complex modifications to the source parameters while maintaining a moment magnitude 7.9 event. The ground motions associated with this further-refined source model are very similar to those generated by the SongMod source model. Figure 3 contains the SongMod in the middle panel, and Ⓔ the electronic edition of *BSSA* contains the slip distributions and slip initiation times on the fault surface for each of the scenario source models.

Scenario Source Models

The first set of scenario rupture models uses the same distributions of slip and rupture speed as the SongMod source model; however, we consider three alternative hypocenter locations: one near the northern end of the rupture (Rockport), one near the center of the rupture (Bodega Bay), and one near the southern end of the rupture (San Juan Bautista). We refer to these scenarios as SongModHypoN, SongModHypoC, and SongModHypoS, respectively. Table 3 gives the precise hypocenters, and Figure 4 provides a map of the locations.

We also consider a set of purely hypothetical rupture models making use of the same rupture geometry. We generate a slip distribution with random phase at all wavelengths using the wavenumber-squared filter given in equation (7) while constraining the average slip to be the same as the SongMod source model. We generated several realizations of the slip model and chose one whose spatial distribution differed substantially from that in the SongMod source model. The slip initiation time follows equation (10), where $t_{\text{orig}} = d/v_r$ and d denotes the rupture path length from the hypocenter and v_r denotes the rupture speed. In these scenarios, we prescribe an average rupture speed of 80% of the local shear-wave speed. We construct source models with these parameters for the 1906 hypocenter as well as the three hypothetical hypocenters. We refer to these scenarios as RandomHypo06, RandomHypoN, RandomHypoC, and RandomHypoS. Figure 3 displays the slip distribution and slip initiation times for RandomHypoN.

Table 3
Hypocenter Locations

Hypocenter	Longitude	Latitude
1906	−122.55	37.75
Rockport	−124.000	39.800
Bodega Bay	−123.016	38.300
San Juan Bautista	−121.615	36.872

All hypocenters are at an elevation of −10 km. Longitude and latitude are given in the WGS84 horizontal datum.

Results

We now focus on the results of the simulations, first considering the 1906 earthquake and then the scenario events. We examine the consistency of the results across the five wave-propagation codes and how well the shaking intensities from the simulations of the 1906 earthquake agree with those in the ShakeMap constructed by Boatwright and Bundock (2005).

1906 Earthquake

The MMI values for the 1906 earthquake reported by Boatwright and Bundock, shown in Figure 1, indicate that the strongest shaking was experienced along the San Andreas fault. In fact, most locations within 50 km of the rupture length experienced shaking intensities of MMI VII or greater. Two regions suffered particularly high shaking: the area extending from Tomales Bay to Santa Rosa (see Fig. 4 for place-name locations) and the southern Santa Cruz Mountains southwest of San Jose. High intensities were also experienced along the northern California coast, with MMI values greater than VIII south of Point Arena and at Cape Mendocino.

These regions with particularly intense shaking north of San Francisco correlate well with large slip (more than 4 m) along the fault directly north of the epicenter. The strong shaking from Tomales Bay to Santa Rosa appears to be accentuated by directivity effects and the supershear rupture speed (>4.5 km/sec) in the first 100 km of rupture north of the epicenter (Boatwright and Bundock, 2008). Strong shaking in Santa Rosa was likely exacerbated by low-velocity basin fill (McPhee *et al.*, 2007).

Fit to Inferred Shaking Intensities

We compute the MMI values from our simulations using relationships between peak horizontal ground velocity (PGV), peak horizontal ground acceleration (PGA), and MMI developed for ShakeMap (Wald, *et al.*, 2005), just as we did for our simulations of the Loma Prieta earthquake (Aagaard *et al.*, 2008). For the broadband simulations,

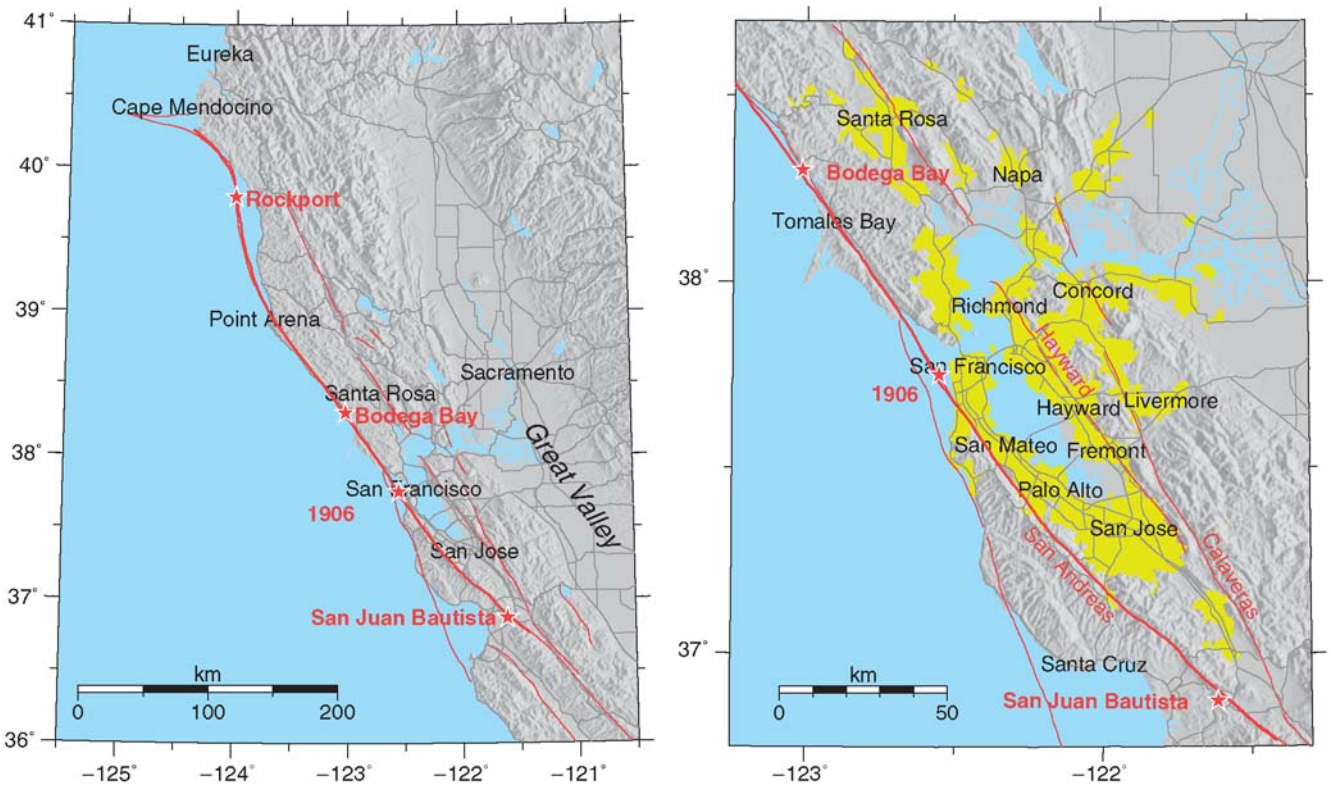

Figure 4. Map of scenario epicenters as viewed on maps of the entire rupture length (left) and the San Francisco Bay vicinity (right). The thick red line delineates the extent of ruptures in the simulations and the red stars denote the 1906 and scenario epicenters. The yellow highlighted regions denote the urbanized areas within the nine-county San Francisco Bay Area.

$$\mathrm{MMI} = \begin{cases} \mathrm{MMI_{PGA}} & \text{if } \mathrm{MMI} < \mathrm{V}, \\ \frac{1}{2}[(\mathrm{VII} - \mathrm{MMI_{PGA}})\mathrm{MMI_{PGA}} \\ \quad + (\mathrm{MMI_{PGA}} - \mathrm{V})\mathrm{MMI_{PGV}}] & \text{if } \mathrm{V} \le \mathrm{MMI} < \mathrm{VII}, \\ \mathrm{MMI_{PGV}} & \text{if } \mathrm{MMI} \ge \mathrm{VII}, \end{cases} \tag{11}$$

$$\mathrm{MMI_{PGA}} = \begin{cases} 2.20\log(\mathrm{PGA}) + 1.00 & \text{if } \mathrm{MMI} < \mathrm{V}, \\ 3.66\log(\mathrm{PGA}) - 1.66 & \text{if } \mathrm{MMI} \ge \mathrm{V}, \end{cases} \tag{12}$$

$$\mathrm{MMI_{PGV}} = \begin{cases} 2.10\log(\mathrm{PGV}) + 3.40 & \text{if } \mathrm{MMI} < \mathrm{V}, \\ 3.47\log(\mathrm{PGV}) + 2.35 & \text{if } \mathrm{MMI} \ge \mathrm{V}, \end{cases} \tag{13}$$

where peak ground acceleration is in *g*s and peak ground velocity is in cm/sec. Because of discrepancies among how the simulations and ShakeMap account for water, we do not include areas covered by water in our analysis. We only use the PGV-to-MMI relation (equation 13) in computing the MMI values for our long-period simulations, because the simulations have low PGA values due to the absence of short-period energy. In fact, because the intensities are above V at most locations, the intensities are relatively insensitive to the level of PGA. This, combined with the observation that the periods of directivity pulses are longer for larger events (Somerville, 2003), suggests that we should expect the long-period simulations to provide similar fits to the Boatwright and Bundock intensities as the short-period simulations.

Our modeling of the Loma Prieta earthquake suggests that intensities computed from our simulations match instrumental intensities within about 0.5 MMI units when compared across the same bandwidths. For the 1906 earthquake, however, we are comparing intensities derived from descriptions of the shaking and damage reports of structures built before modern building codes, not instrumental intensities. This makes calibration of intensity assignments much more difficult due to the variability in construction. Furthermore, the ShakeMap relation for computing MMI from PGV is constrained using events up to magnitude 7.3 with very little data at peak velocities exceeding 1 m/sec (Wald, *et al.*, 1999). Thus, the relationship is poorly constrained for velocities greater than 1 m/sec (MMI values of IX and greater) or magnitude 7.8–7.9 events, and it might over predict shaking intensities for long-period motions, such as those in our simulations. This would lead us to expect the intensities from our simulations to be a little higher than those in the Boatwright and Bundock ShakeMap.

Figures 5 and 6 display synthetic ShakeMaps for the Aagaard and Larsen *et al.* Song simulations. The synthetic intensities reveal a pattern of ground motion similar to the Boatwright and Bundock intensities. Ground motions are highest along the San Andreas fault, especially where the estimated slip was high, and decrease away from the fault. The simulations also capture the pattern of high intensities between Tomales Bay and Santa Rosa. The Boatwright and

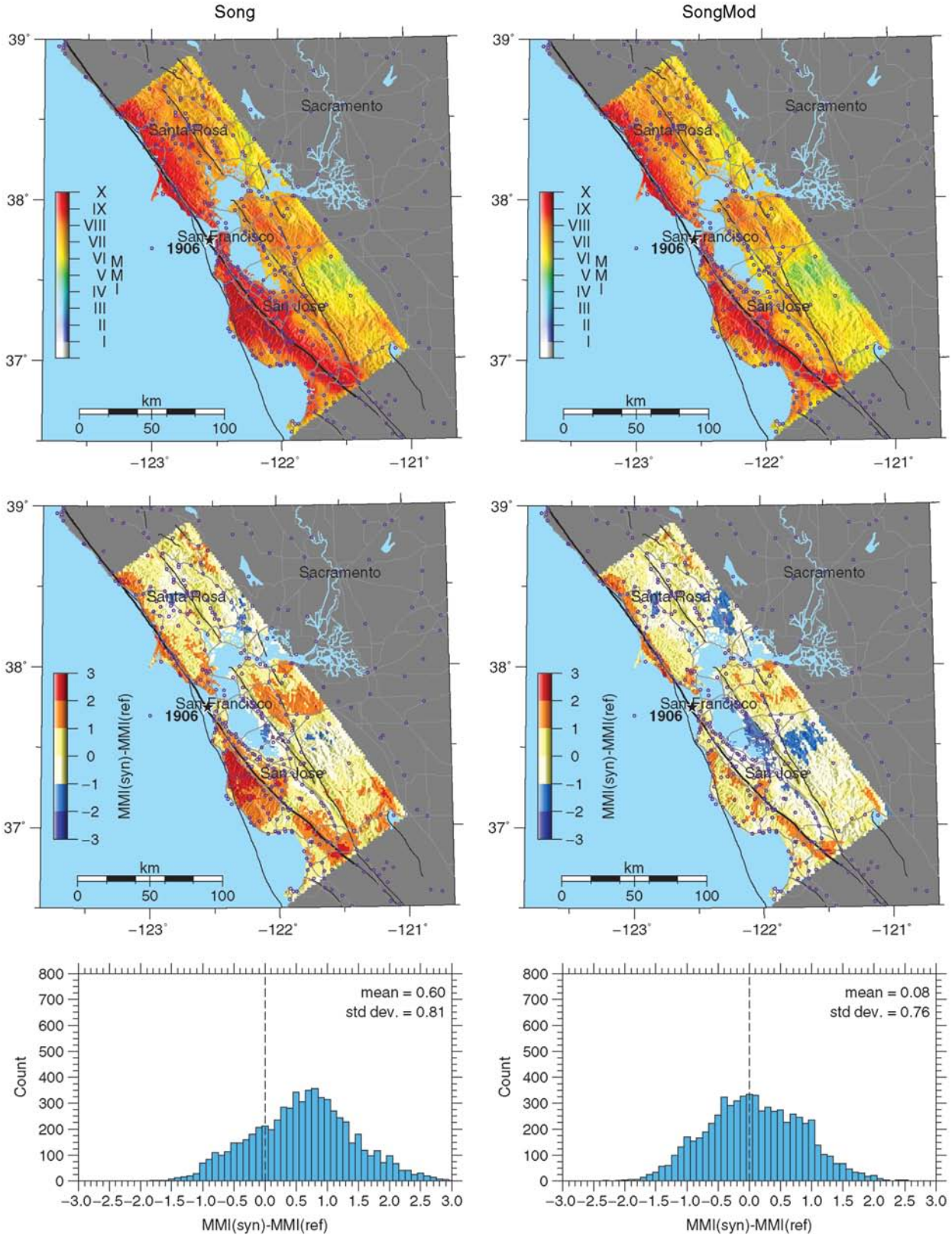

Figure 5. ShakeMaps for Aagaard's simulations ($T > 2.0$ sec) of the 1906 earthquake using the Song (left) and SongMod (right) source models. Open circles identify the Boatwright and Bundock intensity sites. Lower panels show comparisons of the synthetic ShakeMaps with respect to the Boatwright and Bundock ShakeMap. The SongMod simulation matches the Boatwright and Bundock intensities much better than the Song simulation.

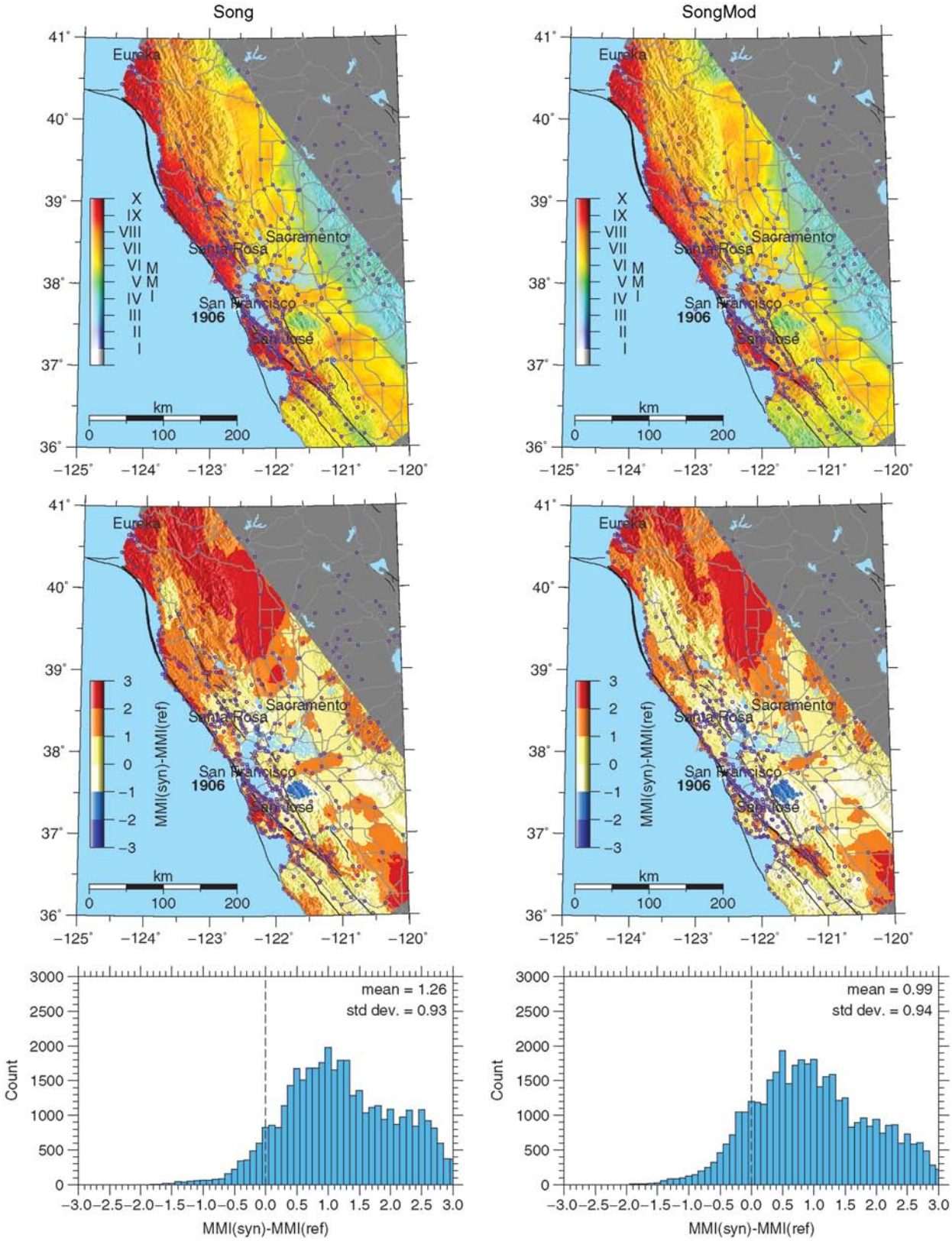

Figure 6. ShakeMaps for Larsen *et al.*'s simulations ($T > 1.0$ sec) of the 1906 earthquake using the Song (left) and SongMod (right) source models. Open circles identify the Boatwright and Bundock intensity sites. Lower panels show comparisons of the synthetic ShakeMaps with respect to the Boatwright and Bundock ShakeMap. The SongMod simulation yields a better fit to the Boatwright and Bundock intensities, but both simulations over predict the intensities north of Sacramento and Santa Rosa where the regional velocity model greatly simplifies the geologic structure.

Bundock intensities have the greatest density within the San Francisco Bay Area. This area also coincides with the detailed portion of the velocity model, so we believe that our simulations are generally more accurate within this area as well. The synthetic intensities for Aagaard's Song simulation in the San Francisco Bay Area, as illustrated in Figure 5, over predict the Boatwright and Bundock intensities by an average 0.60 MMI units. The misfit is largest in the Santa Cruz mountains west of San Jose, where the synthetic intensities are at least two MMI units greater than the Boatwright and Bundock intensities over a significant area, and at the southern end of the rupture. Only a very few scattered locations under predict the shaking intensities.

Based on our Loma Prieta simulations with a well-constrained source model, we would expect the synthetic intensities to have some scatter while under predicting the observed intensities on average. Clearly, the intensities for the Song simulation compared with the Boatwright and Bundock intensities do not follow this trend. The average misfit of 0.60 MMI units in Aagaard's Song simulation corresponds to an over prediction in PGV of about 50%. Boatwright and Bundock (2005) estimate the uncertainties in their MMI assignments to be ± 0.5 MMI units for well-constrained values (such as large towns with multiple reported effects) and up to ± 1.0 MMI units for poorly constrained values (incomplete reports of effects). The large number of samples in the San Francisco Bay Area suggests that, on average, the mean error in the Boatwright and Bundock intensities should be significantly less than 0.5 MMI units. Therefore, we attribute only a small fraction of the average misfit to errors in the Boatwright and Bundock intensities. A larger fraction may arise from error in the PGV/MMI relation at large velocities for large-magnitude events, but these errors would have be quite large to explain a mean misfit of 0.6 MMI units. Therefore, we conclude that our synthetic intensities are too high.

We attempted to reduce the misfit by increasing the rise time (the source parameter with the weakest constraints); however, reasonable increases to the rise time (reducing the peak slip rate) produce only slight reductions in the mean misfit. Similarly, small increases in the rupture width did not significantly reduce the mean misfit. In order to obtain a mean misfit close to zero, the rise time must be increased by about a factor of 2 everywhere. Such rise times are much longer than those extrapolated from observed rise times in kinematic source observations (e.g., the rise time and magnitude relationship derived by Somerville *et al.*, 1999). The most effective means of reducing the misfit involves decreasing the average slip; reducing the slip by 30% decreases the misfit significantly as illustrated in Figure 5 using the SongMod simulation. The misfit of 0.08 MMI units in Aagaard's SongMod simulation corresponds to a misfit in PGV of only about 5%, suggesting that the SongMod simulation gives an acceptable match to the Boatwright and Bundock intensities.

In addition to the reduced average slip in the SongMod source model, the model also includes the short-length scale variations in slip associated with the wavenumber filter and small perturbations to the distributions of slip and rupture speed. However, the dramatic reduction in the mean misfit arises from the lower average slip; the local variations in the source model cause local perturbations in the shaking intensities and have little affect on the mean misfit; instead, they tend to affect the standard deviation. Our small perturbations to the long-length scale distribution of slip and reducing the rupture speed in the southern most 40 km of rupture decrease the locally large misfits in the Santa Cruz mountains west of San Jose and at the southern end of the rupture. Additionally, perturbations in the long length scale slip distribution in the Tomales Bay Area fine tune the fit in the region extending from Tomales Bay to Santa Rosa. Overall, these perturbations to the long-length scale features reduce the standard deviation. On the other hand, the wavenumber filter with random phase creates short-length scale variations that locally increase and decrease the intensities according to the random fluctuations in slip. As a result, the wavenumber filter tends to increase the standard deviation. The combination of these effects results in a drop of the standard deviation from 0.81 in Aagaard's Song simulation to 0.76 in Aagaard's SongMod simulation.

Examining the misfit in shaking intensities over the entire rupture length for the Song source model using Figure 6, we find the synthetic intensities over predict the Boatwright and Bundock intensities over most of the region north of Santa Rosa and Sacramento with a greater misfit than in the San Francisco Bay Area. The area north of Santa Rosa and Sacramento lies outside the detailed portion of the velocity model, so the simulations capture only the most basic geologic effects. For example, the misfit at the northern end of the Great Valley north of Sacramento can be attributed to greatly simplified geologic structure in the regional portion of the velocity model. On the other hand, the over prediction of the intensities in the region adjacent to the rupture north of Santa Rosa is associated with MMI values of X+ and peak velocities exceeding 2 m/sec. Over Larsen *et al.*'s entire simulation domain, the synthetic intensities exceed the Boatwright and Bundock intensities by an average of 1.3 MMI units. We attribute much of this larger mean misfit for Larsen *et al.*'s simulation compared with Aagaard's simulation to the over prediction of the intensities at the north end of the Great Valley resulting from poor resolution of the regional velocity model in this area. Similar to what we found for the San Francisco Bay Area, using the SongMod source model in these simulations of the entire rupture length reduces the mean misfit to 1.0 MMI units. The poor resolution of the regional velocity model prevents the misfit from dropping as much as it did for the Aagaard simulations, which are confined to the detailed portion of the velocity model.

Geodetic Displacements

The geodetic displacements computed by Song *et al.* (2008) from the triangulation surveys provide another, albeit not independent, data source with which to judge the Song

and SongMod simulation results. Note that Song *et al.* use a homogeneous half-space in modeling the triangulation surveys, while we compute the displacements in the simulations using the 3D seismic velocity model. Figure 7 shows that the static surface offsets calculated from the Petersson *et al.* Song ground-motion simulation follow the geodetically derived surface motions corresponding to the triangulation surveys. The displacements from the other Song simulations are nearly identical (Ⓔ see the electronic edition of *BSSA*). At most locations, the residuals are well within the 95% confidence limits of the geodetic displacements.

We expect this agreement with the triangulation surveys because the slip for the Song rupture model was heavily constrained by the geodetic data. In fact, the discrepancies between the simulations and the geodetic displacements reproduce the misfit in displacements for the Song source model (which is constrained by both geodetic and seismic observations). Ⓔ The electronic edition of *BSSA* contains additional figures that illustrate the agreement between our displacements and those associated with the Song source model compared with the displacements from the triangulation surveys. In other words, including 3D material properties, nonplanar fault geometry, and topography do not significantly change the misfit from that already present in the Song source model.

The adjustments made to the Song source model in constructing the SongMod source model (i.e., reducing the slip by 30%, applying a wavenumber squared filter to the slip distribution, and introducing some small perturbations in the long-length scale distributions of slip and rupture speed) slightly degrades the fit to the geodetic displacements (Figs. 7 and 8). The wavenumber filter appears to have the greatest impact at some sites very close to the fault, such as the pair of sites just south of Cape Mendocino, because the differences in the displacements from Song to SongMod coincide with substantially more than a mere 30% reduction in magnitude. Additionally, Figure 8 shows that the residuals for the SongMod model are only slightly larger than those for the Song model. This suggests that the average slip is not tightly constrained as a result of the presence of considerable deformation unrelated to the 1906 earthquake in the triangulation observations.

The triangulation surveys, which largely control the slip in the Song *et al.* inversion, include some long-term strain accumulation, which reduces the geodetic displacements. Song *et al.* (2008) argue that this means the slip in their source model should be considered a lower bound. Reducing the average slip by 30%, on the other hand, appears to be the simplest approach to obtain a reasonable fit to the Boatwright and Bundock intensities. Later, we discuss another way to construct a source model that more evenly balances preserving the characteristics of the Song *et al.* source model and fitting the Boatwright and Bundock (2005) intensities. The ground motions from this source model are very similar to those from the SongMod source model.

Consistency Across Modeling Groups

With significantly better fits to the intensities using the SongMod simulations, we now focus on the consistency in the shaking intensities and ground motions across the wave-propagation codes for this realization of the 1906 earthquake. Figures 9 and 10 display the shaking intensities for the other three modeling groups, including the extension of the Graves simulation to shorter periods. All five of the wave-propagation codes produce similar patterns of shaking intensity (Ⓔ the electronic edition of *BSSA* contains additional figures that more directly illustrate the consistency of the shaking intensities). The intensities are greatest along the San Andreas fault with sedimentary basins accentuating high intensities at some locations, such as Santa Rosa (Windsor and Cotati basins) and southeast of San Jose (Cupertino basin).

The differences in mean misfit with respect to the Boatwright and Bundock intensities result primarily from the use of different modeling domains, but differences in the numerical methods also contribute. For example, the Harmsen simulations predict a bias of 0.31 MMI units in the intensities, but the simulation domain covers a small area where the synthetics best reproduce the Boatwright and Bundock intensities. The Petersson *et al.* simulation yields a similar misfit in the San Francisco Bay Area but exhibits a strong trend of increasing misfit at greater distances from the epicenter due to an absence of attenuation in the simulations. The shaking distribution from Graves's long-period simulation very closely matches the one from Larsen *et al.*'s simulation; the Larsen *et al.* intensities are generally about 0.4 MMI units higher due to a slower minimum shear-wave speed.

Including shorter period energy ($1.0\ \text{sec} > T > 0.1\ \text{sec}$) in the Graves simulation increases the mean misfit of the intensities by 0.09 MMI units (about a 5% increase in PGV), but the standard deviation remains essentially unchanged. The higher intensity values for the broadband simulations primarily arise from the inclusion of site-specific amplification factors, which generally increase the ground-motion amplitudes due to the relatively high minimum V_s of 760 m/sec in the long-period simulations. The distribution of peak ground accelerations (Ⓔ the electronic edition of *BSSA* contains velocity waveforms and maps of peak ground acceleration for a few of the broadband simulations) closely follows the distribution of slip, whereas the distributions of peak velocities (PGV) and MMI are strongly influenced by rupture directivity. These features are consistent with empirical observations of the period dependence of rupture directivity effects (Somerville, 2003).

We can also evaluate the simulations by comparing the spectral accelerations with recently developed empirical attenuation relationships. Figure 11 shows the average horizontal spectral acceleration at Boatwright and Bundock intensity sites from Graves's SongMod broadband ($T > 0.1\ \text{sec}$) simulation. Ⓔ The electronic edition of *BSSA* contains plots for additional periods. The curves delineate the

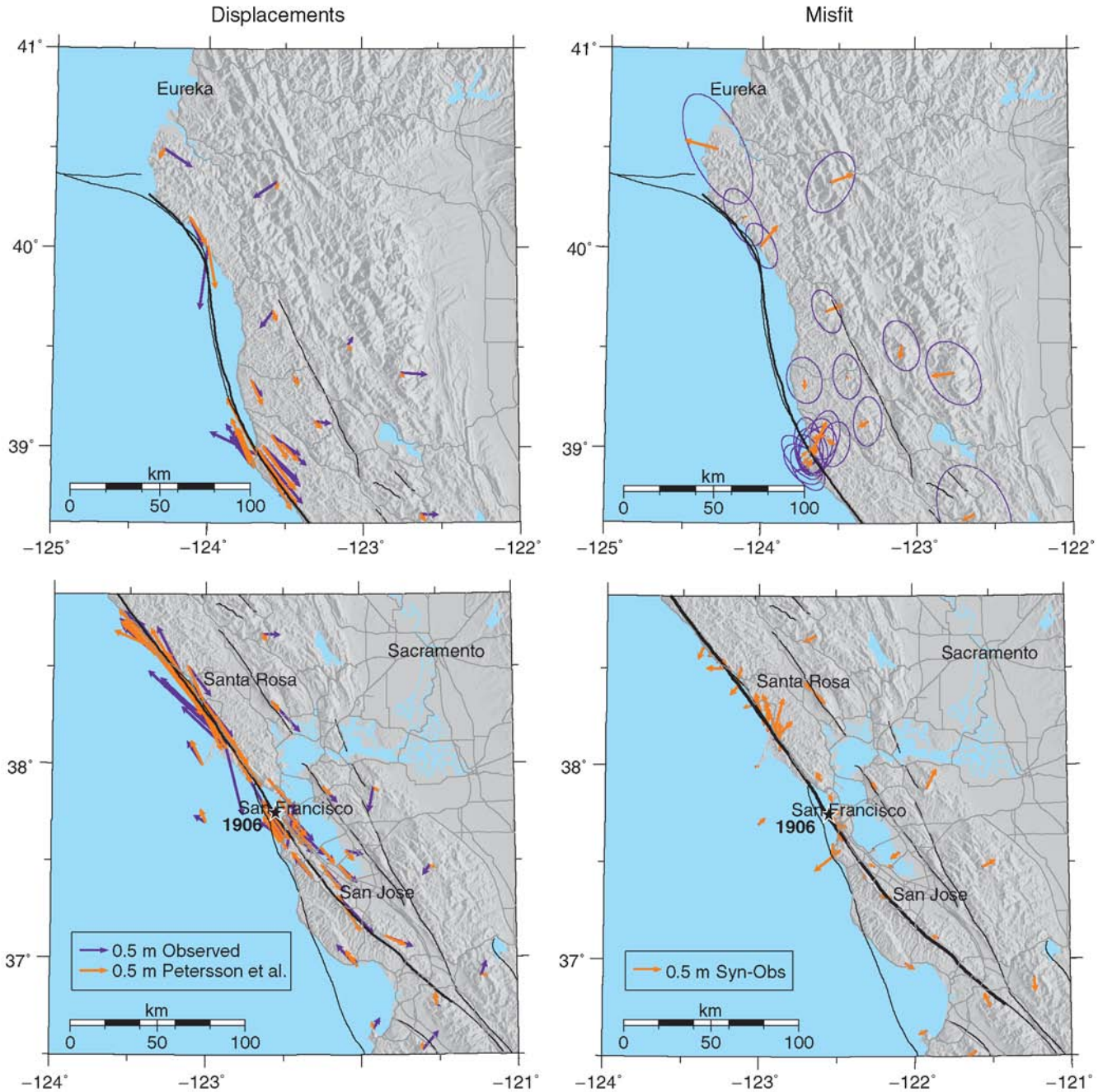

Figure 7. Comparison of geodetic displacements for Petersson *et al.*'s simulations of the 1906 earthquake using the Song source model with the displacements inferred by Song *et al.* from the triangulation surveys. The right panels show the residuals (synthetics minus observed) and the 95% uncertainty limits of the displacements from the triangulation surveys. The upper and lower panels overlap 0.25° in latitude. The synthetic displacements reproduce the observed displacements within the 95% confidence limits.

mean and plus and minus one sigma bounds from the Campbell and Bozorgnia (2007) and Chiou and Youngs (2006) next-generation attenuation relations. We separate the spectral accelerations at the intensity sites into two groups based on a map of V_s30 values compiled by Wills *et al.* (2000). The spectral accelerations from the simulation tend to follow the Campbell and Bozorgnia curves, especially at shorter periods (0.3 sec). This is not surprising because the methodology used in modeling the short-period ground motions was validated with the same data used to constrain the empirical relations developed by the next-generation attenuation project. At longer periods, the spectral accelerations tend to exceed the empirical relations. We associate these discrepancies with the supershear rupture and strong directivity effects in our simulations, which are not explicitly included in the empirical attenuation relations. This may also explain why the syn-

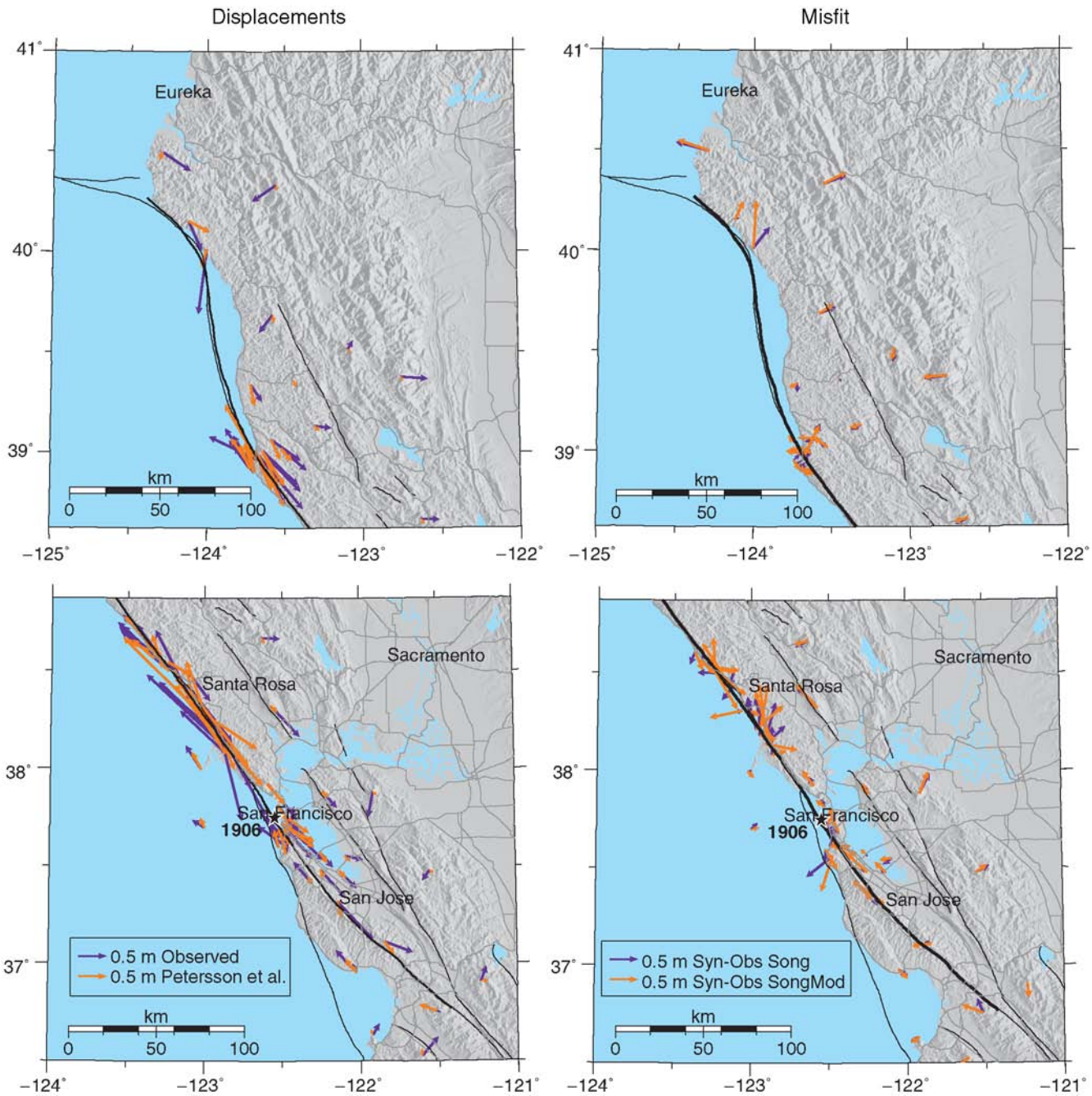

Figure 8. Comparison of geodetic displacements for Petersson *et al.*'s simulations of the 1906 earthquake using the SongMod source model with the displacements inferred by Song *et al.* from the triangulation surveys. The right panels show the residuals (synthetics minus observed) for both the Song and SongMod simulations. The upper and lower panels overlap 0.25° in latitude. The adjustments to the Song source model in constructing the SongMod source model cause only a small increase in the displacement residuals at most locations.

thetic spectral accelerations do not show as much sensitivity to the site conditions (variations in V_s30) as predicted by the attenuation relations at longer periods.

Our broadband source characterization for the 1906 rupture follows from recent observations of large-magnitude surface rupturing earthquakes (e.g., 1992 Landers, 1999 Hector Mine, 1999 Izmit) that all have relatively modest short-period ground-motion levels (Kagawa *et al.*, 2004). Consequently, including the shorter-period energy in the simulations does not have nearly as strong an impact on the PGV levels (and hence MMI estimates) as it did in our Loma Prieta simulations (Aagaard *et al.*, 2008), because relatively long periods dominate the source-rupture process. Based on the relatively small differences that result when we include short periods, we will focus on the long-period simulations for the remainder of this article.

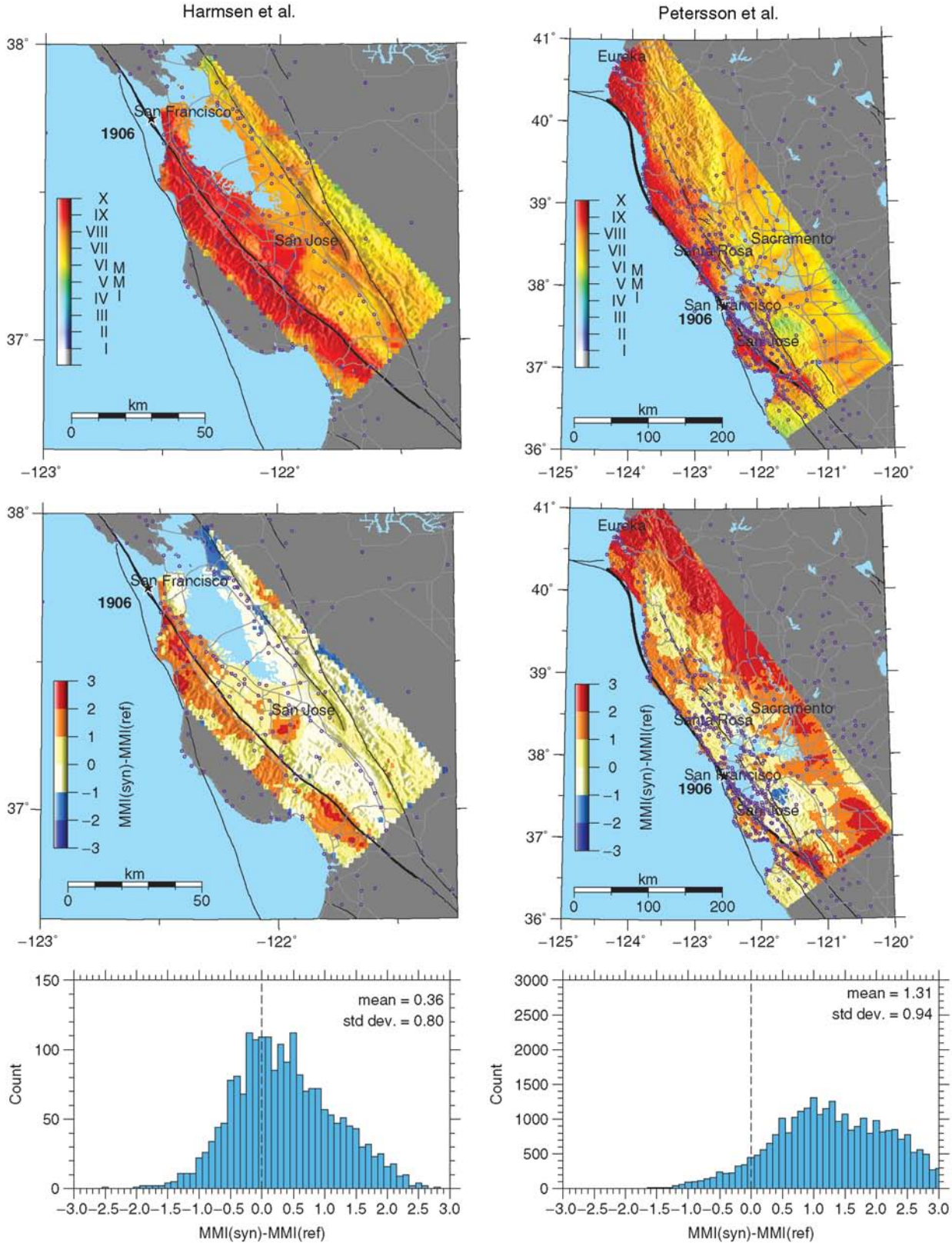

Figure 9. ShakeMaps for Harmsen *et al.*'s simulation ($T > 1.0$ sec) and Petersson *et al.*'s simulation ($T > 2.0$ sec) of the 1906 earthquake using the SongMod source model. Open circles identify the Boatwright and Bundock intensity sites. Lower panels show comparisons of the synthetic ShakeMaps with respect to the Boatwright and Bundock ShakeMap. The Harmsen *et al.* intensities are within 1 MMI unit of the Boatwright and Bundock intensities over most of the simulation domain. Petersson *et al.* over predict the Boatwright and Bundock intensities in areas far from the source due to a lack of attenuation.

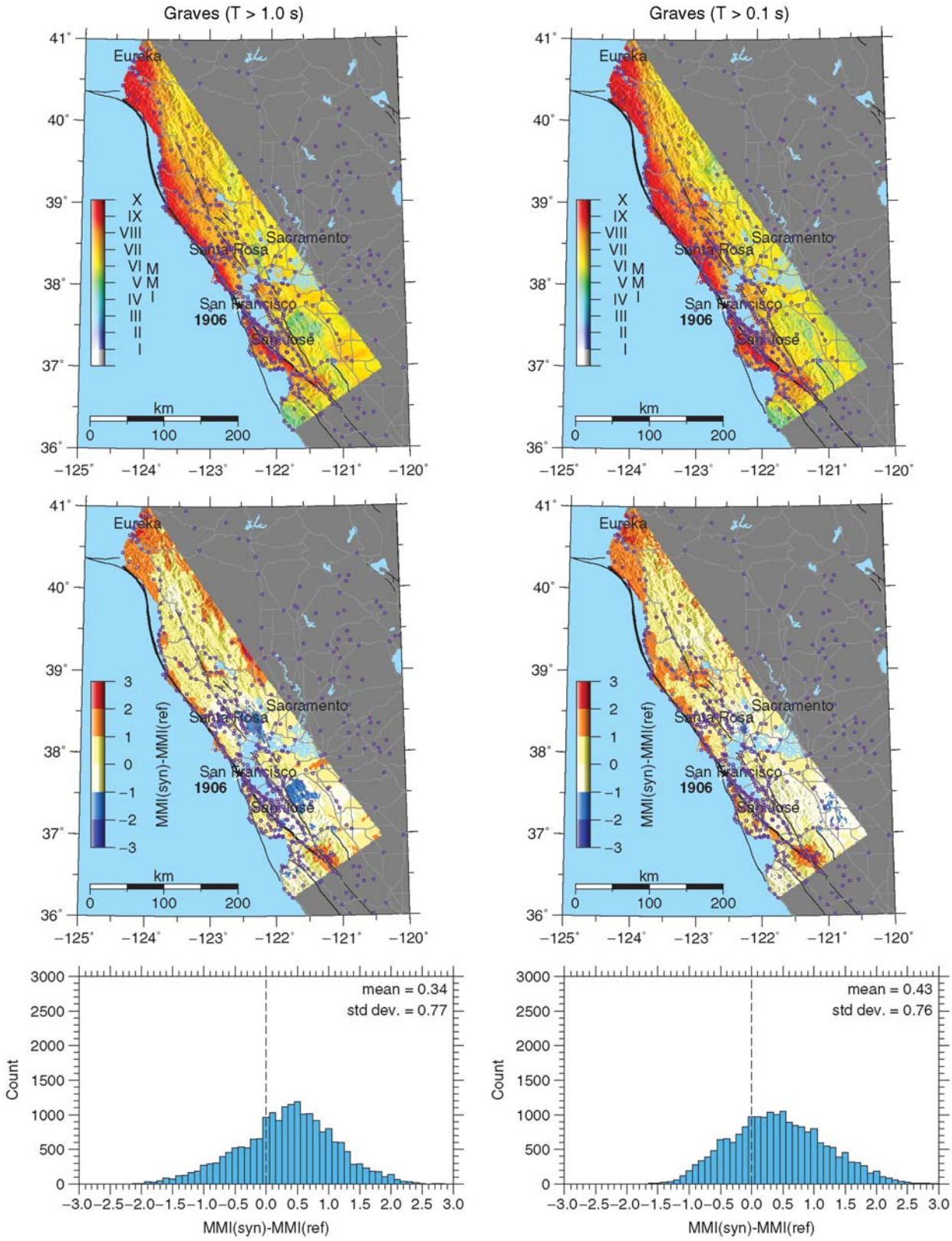

Figure 10. ShakeMaps for Graves's long-period (left) and broadband (right) simulations of the 1906 earthquake using the SongMod source model. Open circles identify the Boatwright and Bundock intensity sites. Lower panels show comparisons of the synthetic ShakeMaps with respect to the Boatwright and Bundock ShakeMap. Extending the long-period simulation ($T > 1.0$ sec) to shorter periods ($T > 0.1$ sec) has little impact on the fit to the Boatwright and Bundock intensities; both match the intensities to within 1 MMI unit over most of the simulation domain.

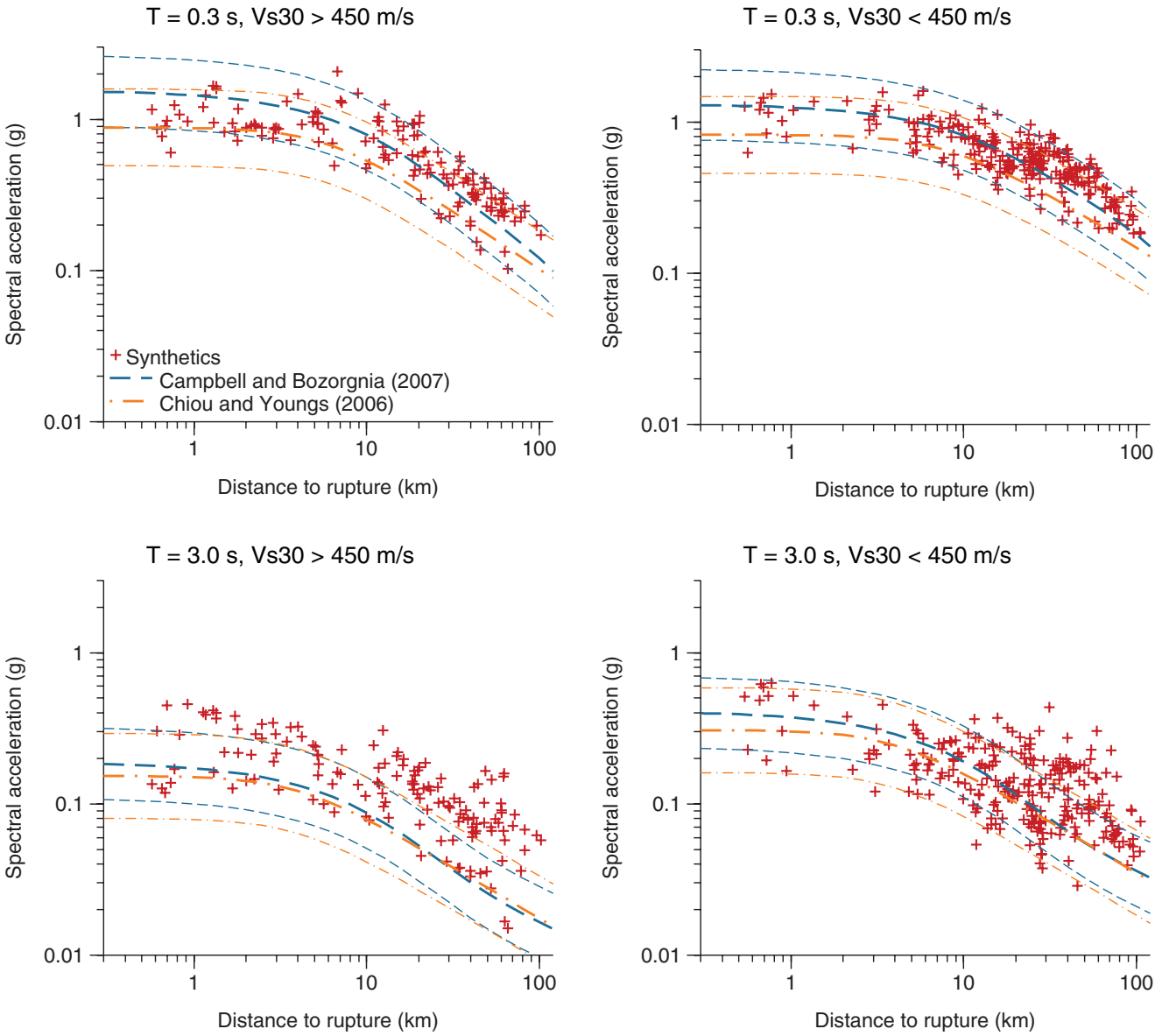

Figure 11. Average horizontal spectral acceleration at the Boatwright and Bundock intensity sites for Graves's broadband simulation of the 1906 earthquake using the SongMod source model. The plots show the spectral acceleration at periods of 0.3 sec (top row) and 3.0 sec (bottom row) for sites with V_s30 values greater than 450 m/sec (left column) and less than 450 m/sec (right column). The curves correspond to the mean spectral acceleration and plus and minus one sigma for two recently developed attenuation relations for V_s30 values of 700 m/sec (left column) and 300 m/sec (right column).

Velocity Waveforms

We now turn our attention to the velocity waveforms for the SongMod simulations. We will discuss the hypothetical scenarios in the next section. Velocity waveforms provide significantly more information about the ground motions than a single-intensity metric such as MMI. For example, they include information about the duration of shaking as well as the polarity of motion. We do not have strong-motion records with which to directly constrain the waveforms, but we do have indirect constraints through the source model and the Boatwright and Bundock intensities. Hence, the velocity waveforms should be indicative of the amplitude and overall duration of shaking with more accurate motions in the detailed portion of the seismic velocity model. Table 4 and Figure 12 give the locations of six sites associated with the velocity waveforms for the simulations displayed in Figures 13–18. All of these six sites lie within the detailed portion of the velocity model except for Eureka, which lies well outside the detailed portion of the model near the northern end of the regional portion. The waveforms in these figures are filtered to a bandwidth of $T > 2.0$ sec. Ⓔ The electronic edition of *BSSA* contains waveforms in the bandwidth of each simulation for these plus four additional sites.

For the SongMod simulations, the velocity waveforms in San Francisco (site SF472, Fig. 13) show a strong double-

Table 4
Locations of Velocity Waveform Sites

Site Label	Location	Longitude	Latitude
SF172	Eureka	−124.1625	40.8022
SF292	Livermore	−121.7669	37.6819
SF472	San Francisco	−122.4183	37.7750
SF474	San Jose	−121.8939	37.3394
SF501	Santa Rosa	−122.7133	38.4406
CT06013301000	Sacramento delta	−121.6301	38.0383

Site CT06013301000 is the centroid of census track 06013301000. The other sites correspond to Boatwright and Bundock (2005) intensity sites.

sided pulse in the north–south direction with a weaker pulse in the east–west direction. This is consistent with a strong fault-parallel pulse in the northwest–southeast direction associated with the *SH* wave radiated perpendicular to the fault away from the epicenter. The strong shaking begins within a few seconds of the rupture initiation and ends about 15 sec later. The amplitudes in the Harmsen *et al.* velocity waveforms are smaller than the others because the Harmsen *et al.* model is truncated just north of San Francisco so that the waveforms are missing contributions from the source north of their domain boundary.

Rupture directivity and local geologic structure influence the waveforms in San Jose (site SF474, Fig. 14). The strong shaking does not begin until about 20 sec after rupture initiation and lasts for about 35 sec. Direct shear waves and Love waves emanating from the nearby Cupertino basin west of San Jose dominate the motions. Love waves arriving at about 45 sec produce the peak velocities. The early phases are very similar across all wave-propagation codes. The Harmsen *et al.* simulation predicts significantly more of a basin response than the other four simulations beginning at about 40 sec. This difference likely arises from the lower minimum shear-wave speed of 330 m/sec in the Harmsen *et al.* simulations.

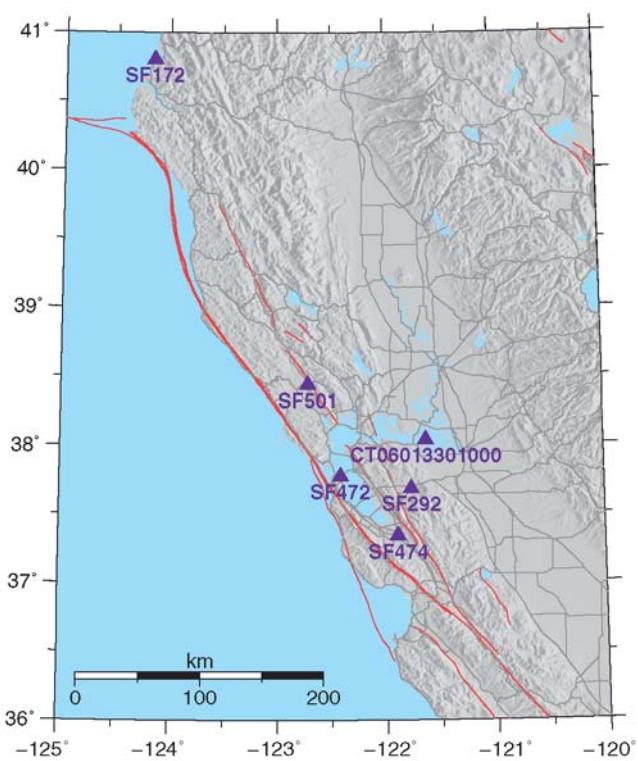

Figure 12. Locations of the six sites used in the comparison of velocity waveforms. Place names for the sites are given in Table 4.

In Livermore (site SF292, Fig. 15) the Livermore basin amplifies the shaking, but the amplitudes are smaller than in San Jose due to the greater distance from the rupture and the source characteristics, including the southward rupture propagation and distribution of slip. Relative to the epicenter, Livermore lies near a node in the shear-wave radiation pattern and a peak in the compressional-wave and Rayleigh-wave radiation patterns. This results in a relatively weak onset to the motion at about 22 sec with larger-amplitude shaking corresponding to the Rayleigh waves dominating the motion from 30–45 sec. The wave-propagation codes produce very similar motions at Livermore, capturing both the early phases and the Rayleigh waves.

The Cotati and Windsor basins strongly influence the waveforms in Santa Rosa (site SF501, Fig. 16). Large slip north of the epicenter and the supershear rupture speed directs energy toward Santa Rosa. When combined with amplification in the basins, this creates a very strong shear-wave arrival at about 22 sec in the east–west direction. The complex basin structure creates a beating effect in the ground motions, especially in the north–south direction, where strong shaking at around 26–36 sec is followed by a short lull before strong shaking returns for about 16 more seconds. Differences in the resolution of the simulations appear to create small discrepancies in the waveforms, especially for the later arrivals in the east–west direction. Nevertheless, the north–south and vertical components of the synthetic waveforms give a consistent indication that the duration of strong shaking was about 40 sec.

Only two of the ground-motion simulations, Graves and Larsen *et al.*, provide waveforms at the site in the delta region of the Sacramento and San Joaquin rivers (site CT06013301000, Fig. 17). The delta sits over the western edge of the Great Valley, with sedimentary rocks down to a depth of 10 km (Wentworth *et al.*, 1995). As a result, large-amplitude, long-duration surface waves characterize the motions; both simulations illustrate that shear and Love waves with periods in the range of 8–10 sec dominate the waveforms at this site. The distance from the source, coupled with slow sediments, result in a relatively slow decay in motions over about 50 sec.

Shear-wave directivity controls the ground motions in Eureka (site SF172, Fig. 18). Eureka sits in the forward directivity direction so that all of the strong shear-wave energy radiated along the fault from the epicenter to the northern extent of rupture arrives within a short time window. As a result, the motions are dominated by large-amplitude, long-period velocity pulses polarized in the east–west (fault per-

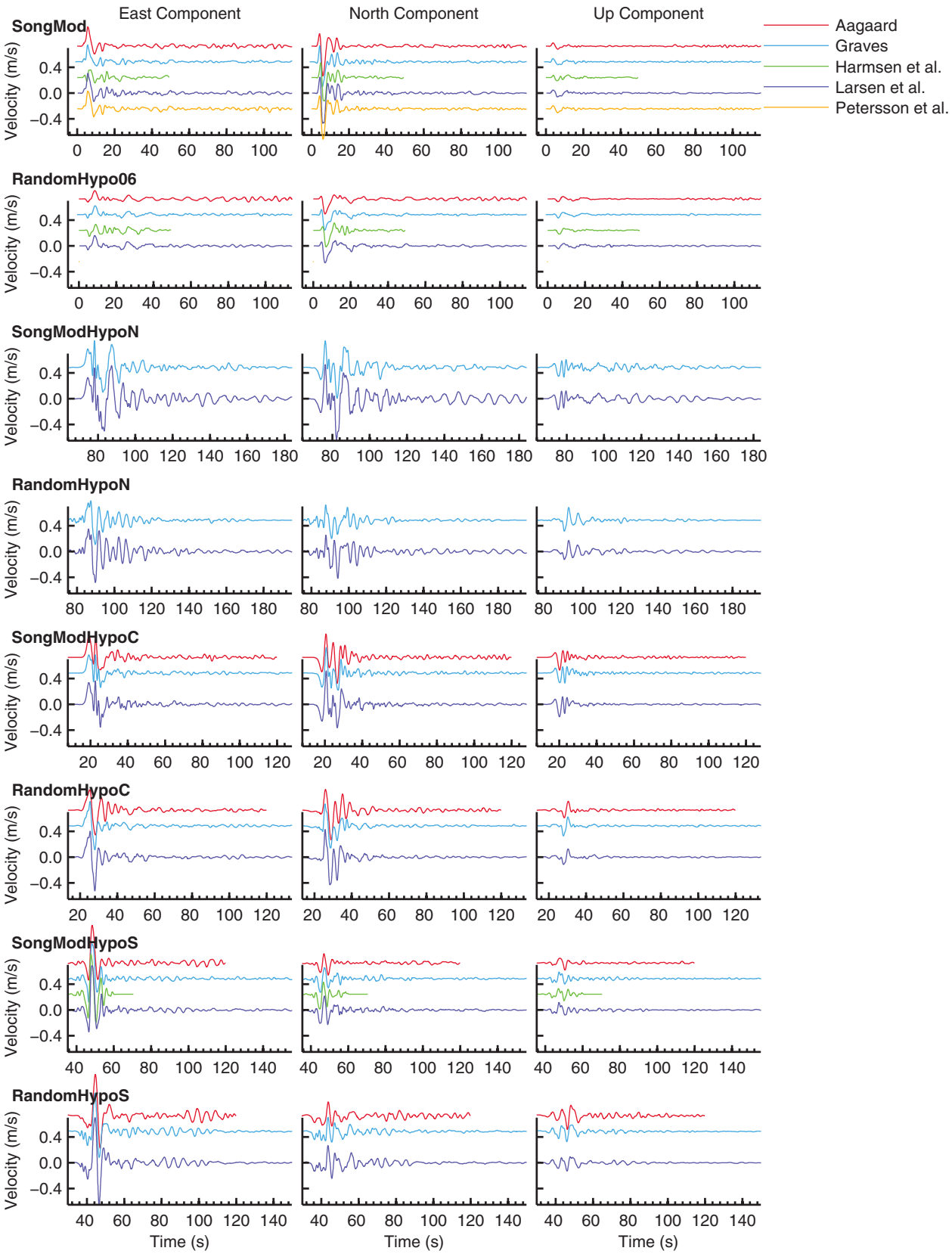

Figure 13. Comparison of velocity waveforms in downtown San Francisco (site SF472). All waveforms have been low-pass filtered to a bandwidth of $T > 2.0$ sec. Time is with respect to the origin time; changing the hypocenter affects the arrival time. Many of the hypothetical scenarios produce stronger shaking in San Francisco than the 1906 earthquake.

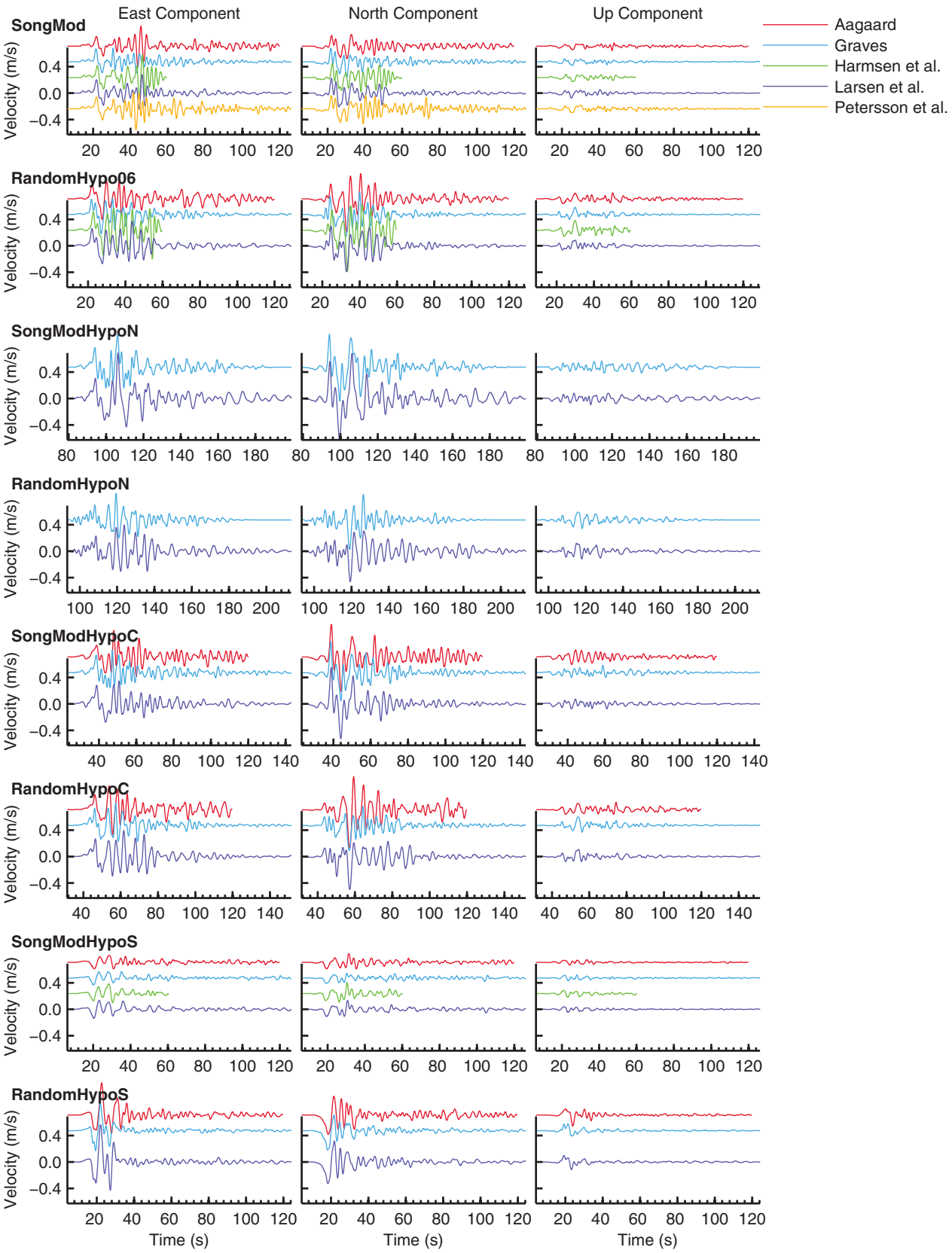

Figure 14. Comparison of velocity waveforms in downtown San Jose (site SF474). All waveforms have been low-pass filtered to a bandwidth of $T > 2.0$ sec. Time is with respect to the origin time; changing the hypocenter affects the arrival time. North-to-south ruptures consistently cause strong shaking lasting tens of seconds in San Jose.

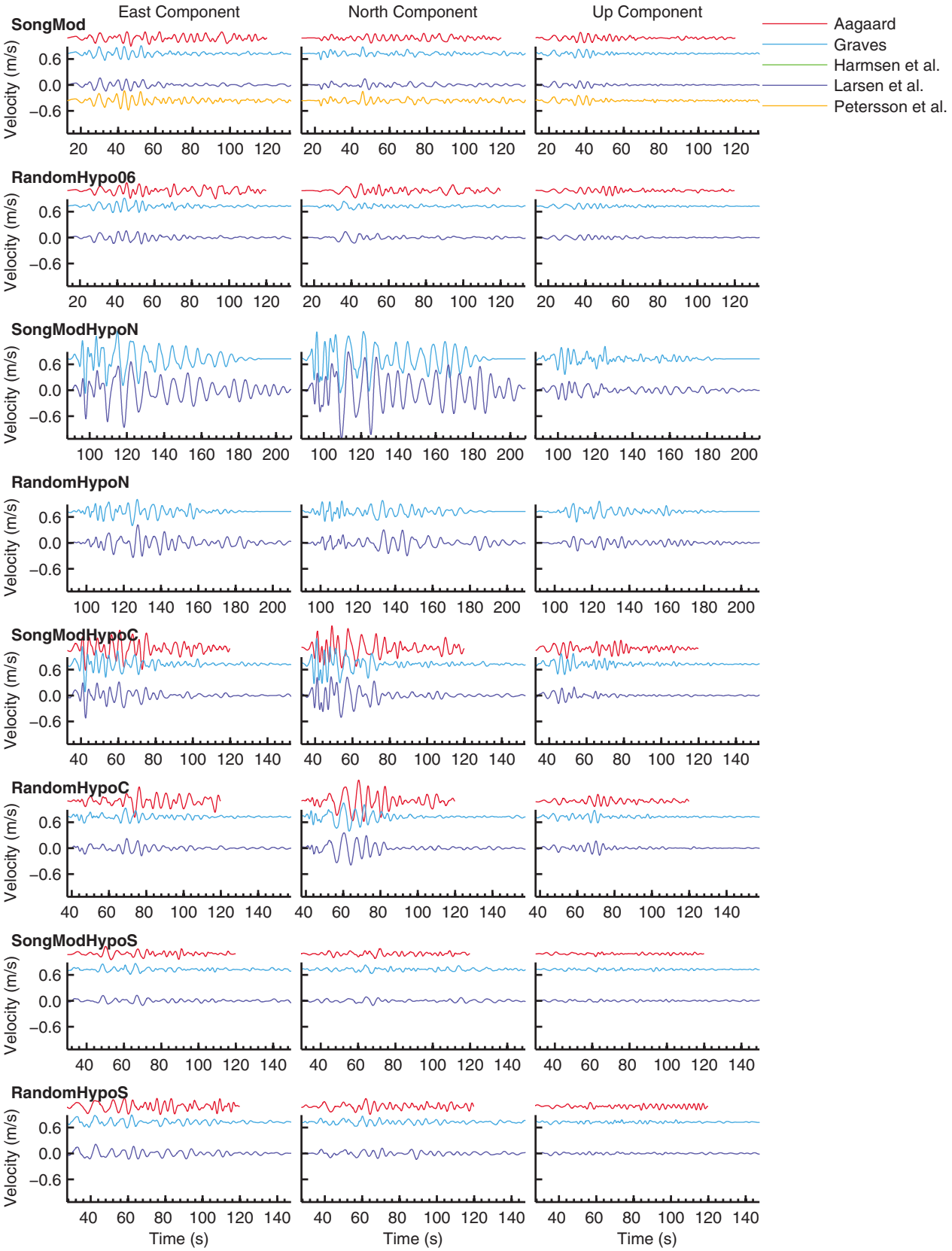

Figure 15. Comparison of velocity waveforms in Livermore (site SF292). All waveforms have been low-pass filtered to a bandwidth of $T > 2.0$ sec. Time is with respect to the origin time; changing the hypocenter affects the arrival time. North-to-south ruptures radiate abundant energy into the Livermore basin resulting in large-amplitude, long-duration motions.

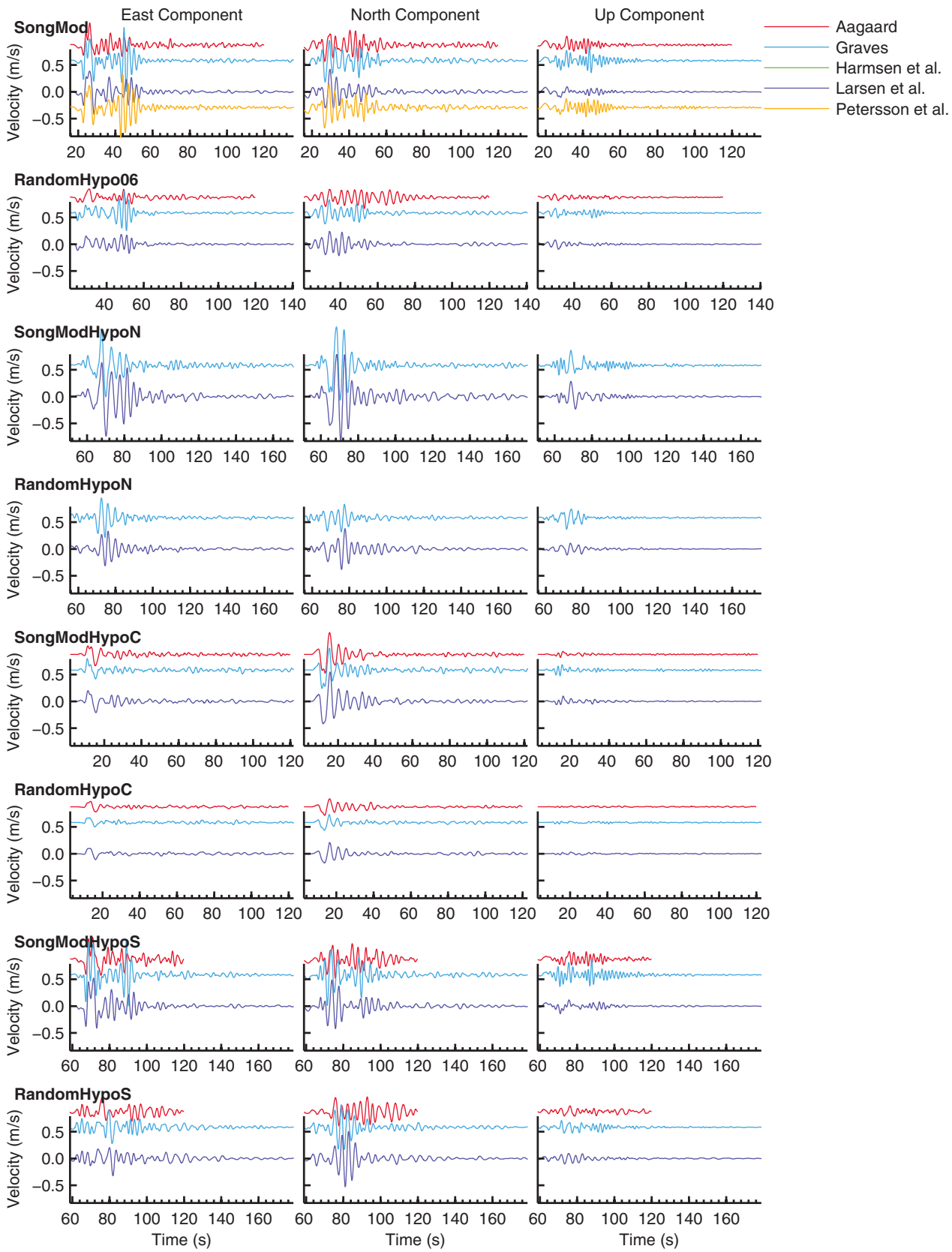

Figure 16. Comparison of velocity waveforms in Santa Rosa (site SF501). All waveforms have been low-pass filtered to a bandwidth of $T > 2.0$ sec. Time is with respect to the origin time; changing the hypocenter affects the arrival time. The Cotati and Windsor basins amplify the ground motions leading to strong shaking in most of the scenarios, but the details of the waveforms are strongly dependent on the hypocenter, slip distribution, and propagation path.

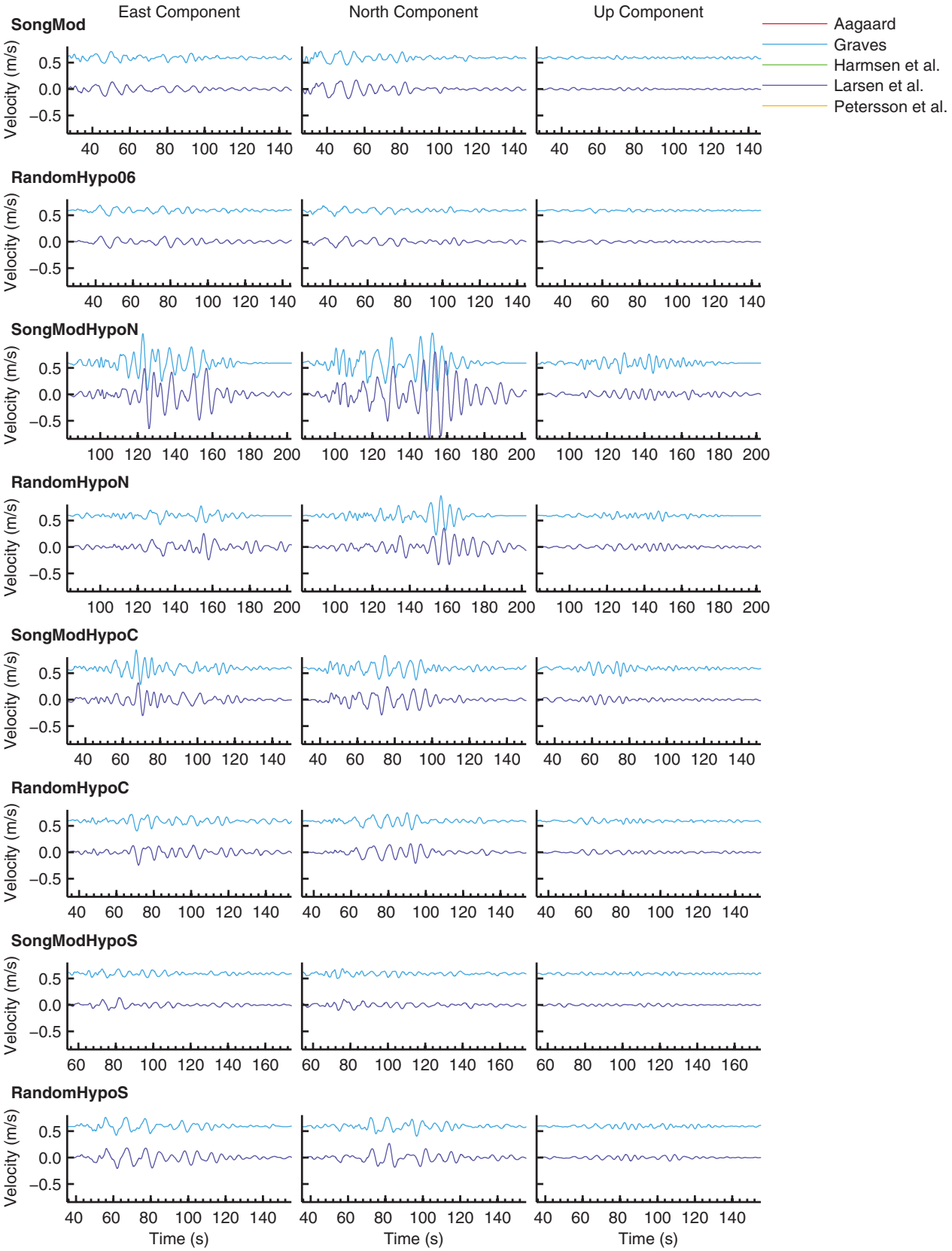

Figure 17. Comparison of velocity waveforms in the Sacramento–San Joaquin delta (site CT06013301000). All waveforms have been low-pass filtered to a bandwidth of $T > 2.0$ sec. Time is with respect to the origin time; changing the hypocenter affects the arrival time. The Delta sits over the western end of the Great Valley; this large basin amplifies surface waves, leading to long-duration long-period shaking.

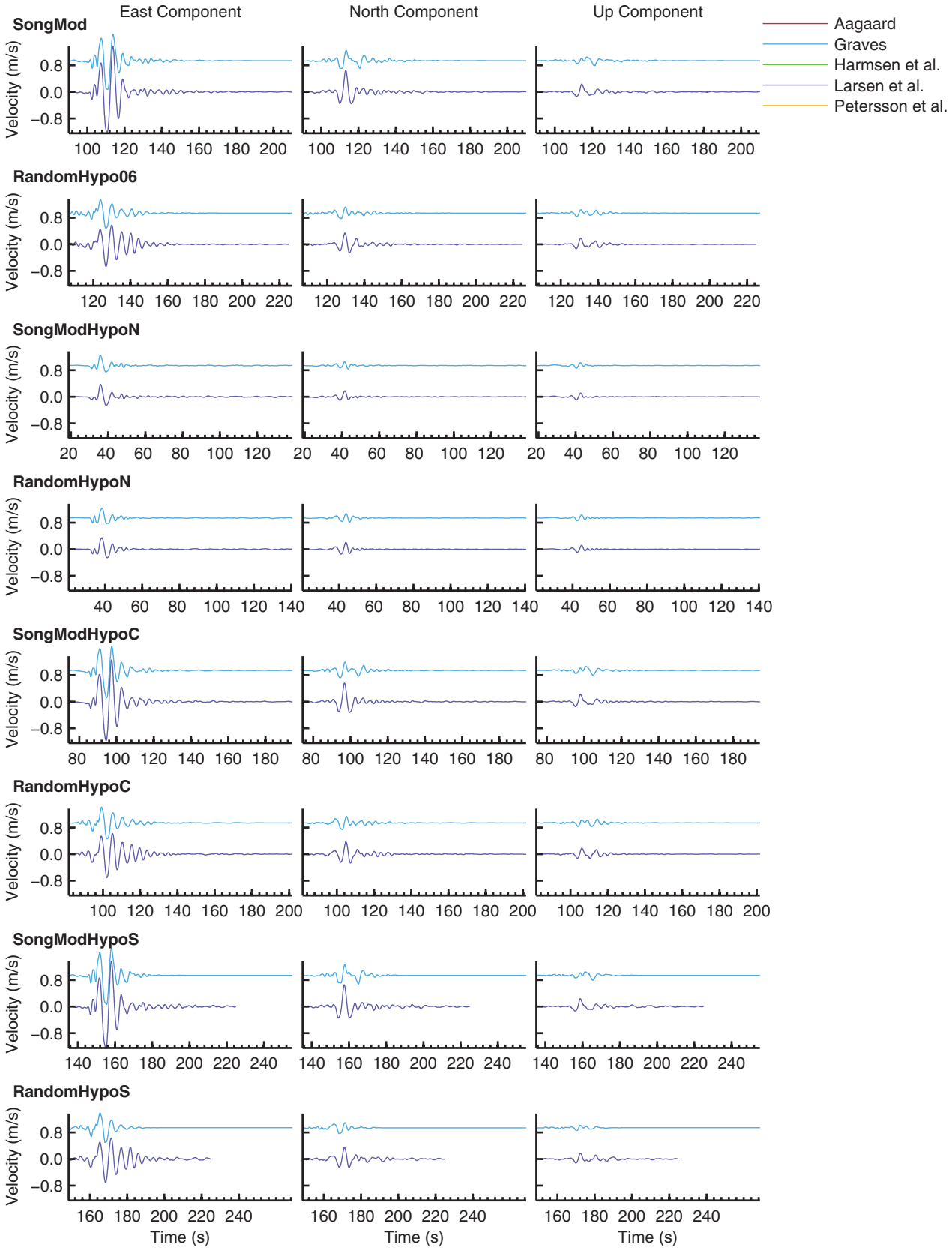

Figure 18. Comparison of velocity waveforms in Eureka (site SF172). All waveforms have been low-pass filtered to a bandwidth of $T > 2.0$ sec. Time is with respect to the origin time; changing the hypocenter affects the arrival time. South-to-north ruptures produce strong directivity pulses in Eureka. Ruptures that start near Eureka and propagate south produce smaller motions.

pendicular) direction. The duration of very strong shaking is only about 20 sec. The wave-propagation codes show excellent consistency in the waveform shape for these velocity pulses, but the Larsen *et al.* simulation predicts slightly larger amplitudes than the Graves simulation, which we attribute to the lower minimum shear-wave speed used in the Larsen *et al.* simulations.

Alternate Earthquake Scenarios

We know neither the slip distribution nor the hypocenter of future large earthquakes on the northern San Andreas fault, so we must examine a variety of scenarios in order to characterize the potential shaking in future, large northern San Andreas fault earthquakes. In this study, our objective is to assess the variability in the ground motions and distributions of shaking for a limited number of scenarios with different hypocenters and different distributions of slip. We consider three alternative hypocenters with the SongMod source model, as well as a random slip distribution with the same suite of different hypocenters. Contrasting the random slip distribution (Random) with the SongMod model (see Fig. 3), the San Francisco to Tomales Bay portion of the rupture has less slip, whereas the San Jose to San Francisco portion has more slip. In the random slip source models, we also keep the rupture subshear over the entire rupture extent. This reduces the rupture speed in the first 100-km north of the epicenter compared with the simulations using the SongMod rupture speed distribution.

Changing the hypocenter directly affects the rupture directivity and has the strongest influence on the overall distribution of shaking for our suite of eight earthquake simulations. In each case, rupture directivity generates strong shaking along the fault away from the epicentral region, creating strong correlations between the distributions of shaking for each pair of simulations with the same hypocenter (Figs. 19–22). Most areas subjected to the strongest shaking with the Song distribution of slip are also exposed to the strongest shaking with the Random distribution of slip. These areas are generally confined to regions in close proximity to the fault rupture and regions with softer near-surface sediments, such as the southern perimeter of the San Francisco Bay, the delta of the Sacramento and San Joaquin rivers, and the Santa Rosa area. In the San Francisco Bay region, the strongest directivity and ground motions with MMI values greater than VIII arise from rupture starting at northern and central hypocenters (Rockport and Bodega Bay, Figs. 19 and 20). Areas near the northern and southern ends of the Great Valley also tend to experience significant shaking with MMI values around VII, but these are areas within the regional seismic velocity model where our simulations are not as accurate due to the coarse resolution of the geologic structure.

The most significant changes in the distributions of shaking intensity occur along the San Francisco peninsula between San Jose and San Francisco. The greater slip along this portion of the San Andreas fault in the Random source model accentuates the directivity effects, increasing the shaking intensities for each of the hypocenters from MMI in the range VII–VIII to MMI in the range VIII–IX (Figs. 19–22). North of Point Arena, the opposite effect occurs; the Random slip distribution has less slip than that in SongMod, and the shaking intensities decrease by about one MMI unit. The decrease in rupture speed in the 100-km north of San Francisco for the random slip scenarios tends to decrease the shaking intensities from around VII–VIII to around VI–VII in the vicinity of Santa Rosa, because subshear rupture directs less energy away from the fault compared with supershear rupture (Aagaard and Heaton, 2004).

In downtown San Francisco (site SF472, Fig. 13) the velocity waveforms reaffirm the strong influence of the hypocenter. The amplitude and duration of shaking tend to correlate across hypocenter location much more so than across the slip distributions. The duration of strong shaking for the northern hypocenter (SongModHypoN and RandomHypoN) is about 40 sec compared to 15–20 sec for the central and southern hypocenters (SongModHypoC, RandomHypoC, SongModHypoS, and RandomHypoS), and as little as 15 sec for the 1906 hypocenter (SongMod and RandomHypo06). The largest amplitude motions (with peak velocities of about 0.6 m/sec) are associated with strong shear-wave directivity; this occurs in the four scenarios with the two hypocenters north of San Francisco (Rockport and Bodega Bay) and the southern hypocenter at San Juan Bautista (especially for the case of random slip). The southern hypocenter generates motion predominantly in the east–west direction, whereas the hypocenters north of San Francisco generate motions in the east–west and north–south direction of about the equal amplitude. This difference cannot easily be tied to features in the source models because the slip distributions for the SongMod and Random models are significantly different, and the rupture speeds in SongModHypoN and SongModHypoC are supershear immediately north of San Francisco but subshear in this same region for RandomHypoN and RandomHypoC.

The amplitude and duration of shaking is somewhat more consistent across the eight scenarios in San Jose (site SF474, Fig. 14). The strongest shaking lasts about 40 sec for the three hypocenters north of San Jose (Rockport, Bodega Bay, and 1906). The largest amplitude motions occur for the central and northern hypocenters, and the peak velocities reach 0.5 m/sec many times over the 20 sec of intense shaking. In the case of the southern epicenter at San Juan Bautista, the rupture radiates most of the energy north of San Jose. In the SongModHypoS simulation, the velocities are less than 0.2 m/sec, but in the case of the random slip distribution, large slip on a portion of the rupture nearby does generate large-amplitude motions with velocities reaching 0.4 m/sec.

The simulations suggest that the ground motions in both Livermore (site SF292, Fig. 15) and Santa Rosa (site SF501, Fig. 16) from large events on the San Andreas fault are quite variable. For some hypocenters and slip distributions, the

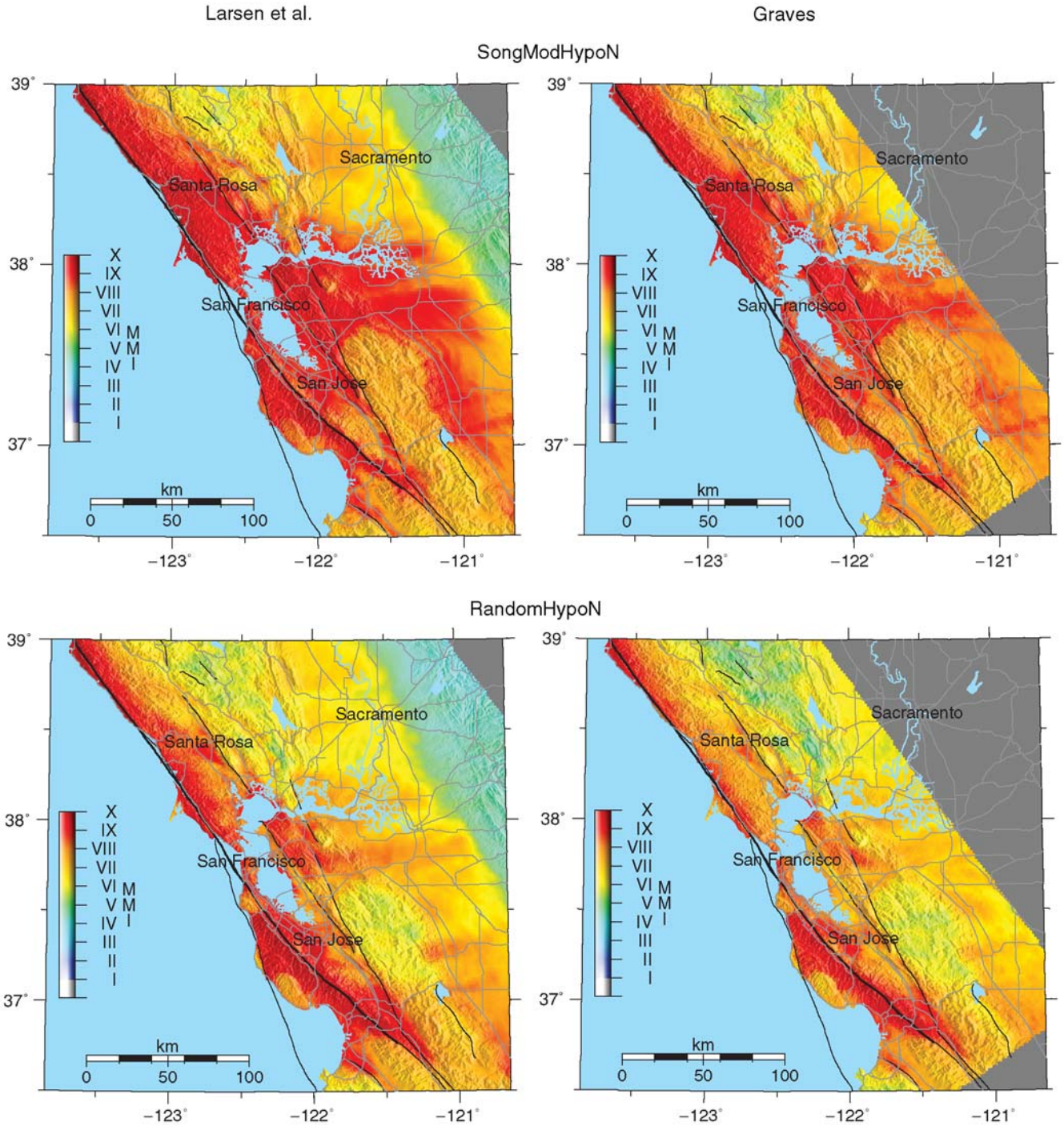

Figure 19. ShakeMaps covering the San Francisco Bay Area for Larsen *et al.*'s ($T > 1.0$ sec, left) and Graves's ($T > 1.0$ sec, right) SongModHypoN and RandomHypoN simulations. The thick black line delineates the rupture; the epicenter lies north of the region shown in the map. The SongModHypoN simulations produce the strongest shaking in the San Francisco Bay Area of the scenarios considered in this study. The RandomHypoN simulations also produce strong shaking but the intensities east of the San Francisco Bay are 1–2 MMI units lower.

peak velocities fail to exceed 0.3 m/sec. In other cases, such as SongModHypoN, the peak velocities approach and may exceed 1 m/sec at each location. The significant variations in amplitude and duration of motion can be attributed to both site and source effects. Some scenarios, such as SongModHypoN and SongModHypoC with supershear rupture and large slip north of San Francisco, radiate much more energy toward Livermore than the other scenarios. The Livermore basin amplifies the incoming surface waves and traps the energy, giving rise to large-amplitude, long-duration motions.

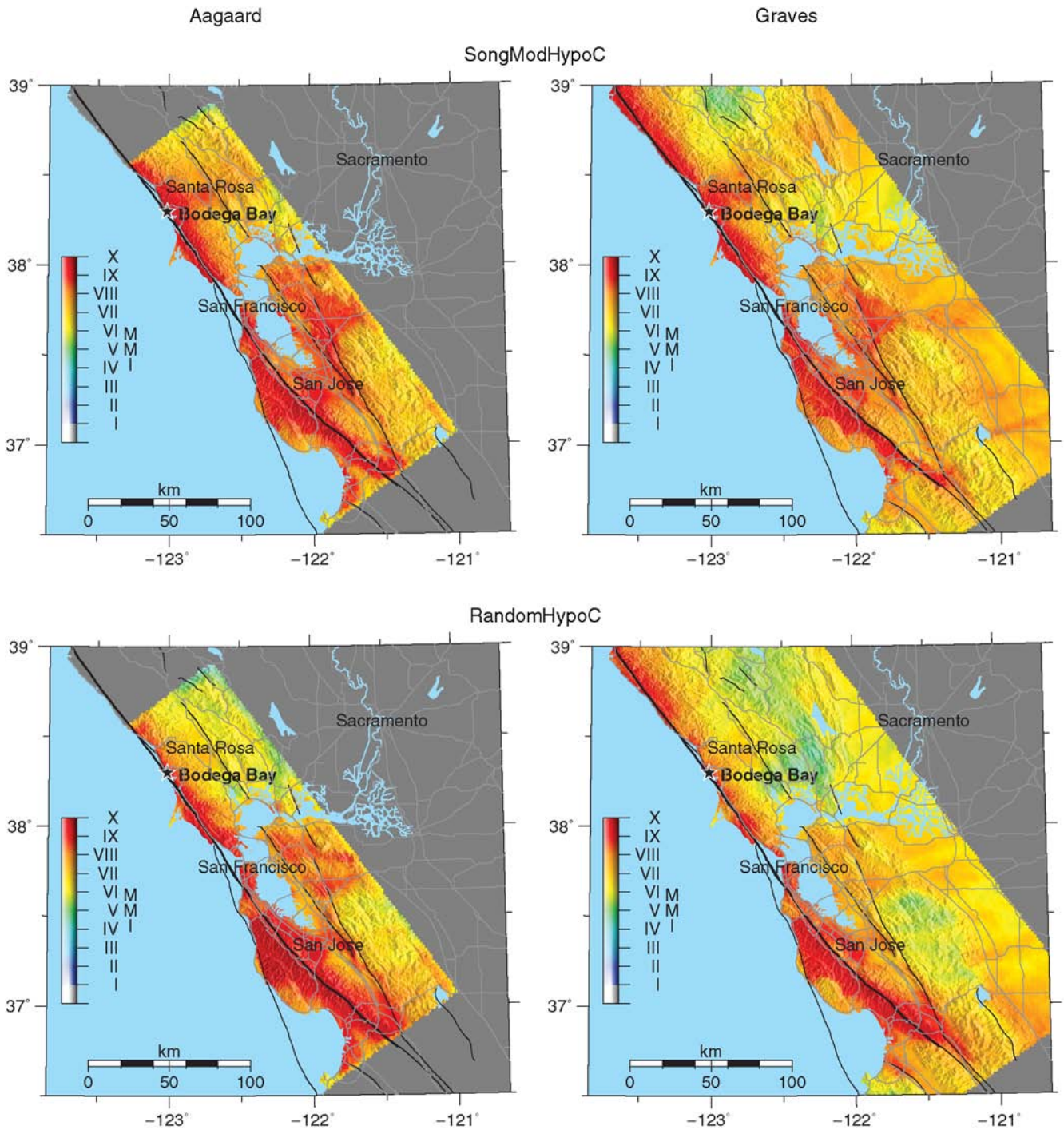

Figure 20. ShakeMaps covering the San Francisco Bay Area for Aagaard's ($T > 2.0$ sec, left) and Graves's ($T > 1.0$ sec, right) SongModHypoC and RandomHypoC simulations. The thick black line delineates the rupture, and the black star identifies the epicenter. The SongModHypoC simulations yield a similar pattern of shaking in the San Francisco Bay Area to the SongModHypoN simulations but with slightly lower intensities. Changes to the slip distribution as illustrated by the RandomHypoC simulations perturb the distribution of shaking, but the intensities remain high along the fault as a result of rupture directivity.

Similarly, the Cotati and Windsor basins exhibit a strong influence on the motions in Santa Rosa. The northward-propagating ruptures with large slip north of San Francisco in SongMod and SongModHypoS generate large Rayleigh waves that bounce around the basins, resulting in a beating effect with two large pulses of energy spread over about 40 sec.

The delta of the Sacramento and San Joaquin rivers sits about 40-km farther away from the fault than Livermore, but at a similar location along the central portion of our ruptures.

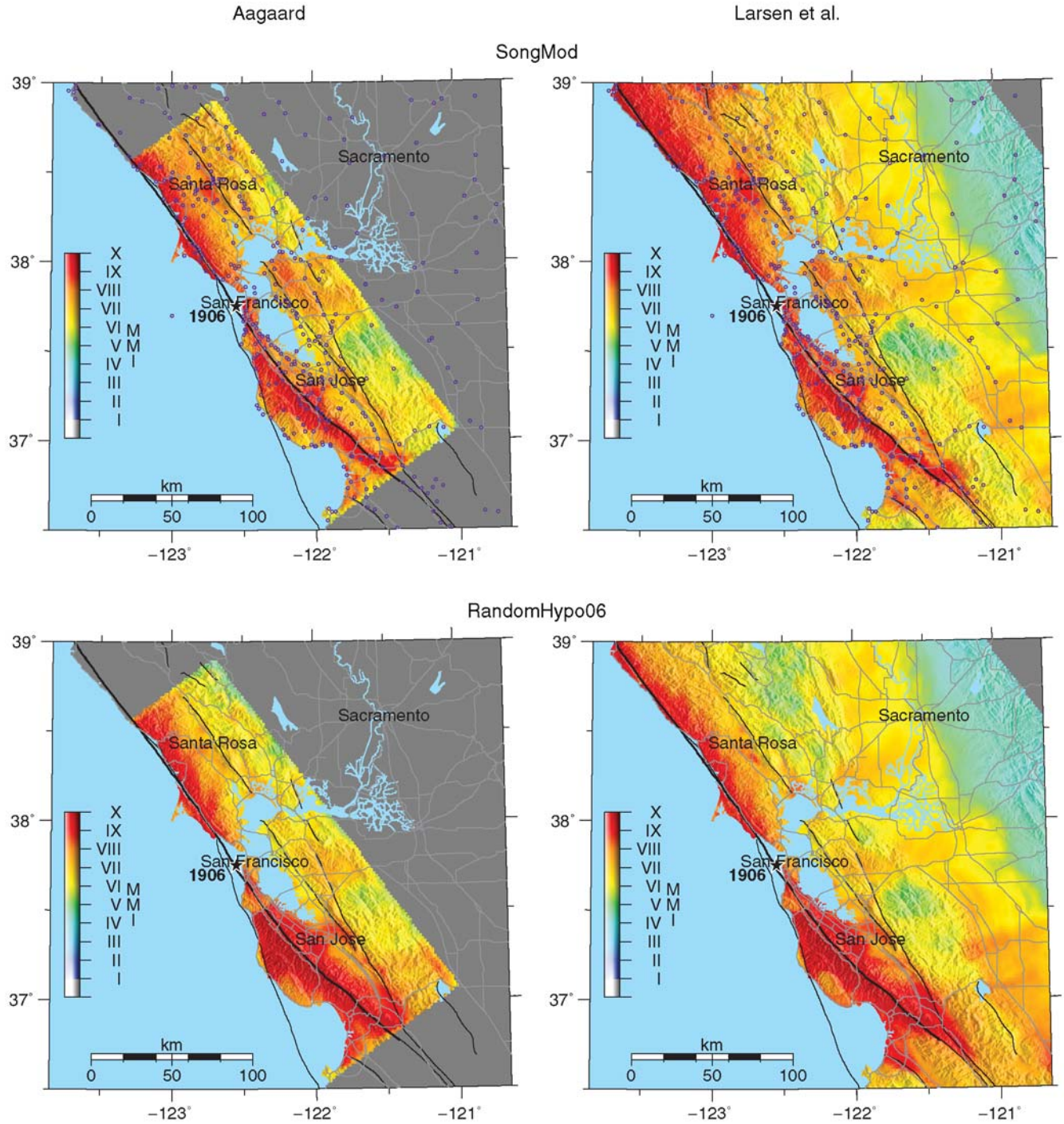

Figure 21. ShakeMaps covering the San Francisco Bay Area for Aagaard's ($T > 2.0$ sec, left) and Larsen *et al.*'s ($T > 1.0$ sec, right) SongMod and RandomHypo06 simulations. The thick black line delineates the rupture, and the black star identifies the epicenter. The ShakeMaps for SongMod are duplicates of those in Figures 5 and 6, and the open circles identify Boatwright and Bundock intensity sites. Greater slip along the San Francisco peninsula in the Random slip model increases the shaking intensities between San Francisco and San Jose in the RandomHypo06 simulations compared with the SongMod simulations.

Consequently, the ground motions in the delta region (e.g., site CT06013301000, Fig. 17) are strongly correlated with the rupture characteristics on this central portion. SongMod-HypoN, with its southward supershear rupture propagation and large slips north of San Francisco, radiates more energy away from the fault along this central portion than the other scenarios. As a result, the velocities in the delta exceed 0.6 m/sec with at least 90 sec of strong shaking. Velocities exceeding 0.2 m/sec with significant shaking lasting about 60 sec are generated at this location in the delta for Random-

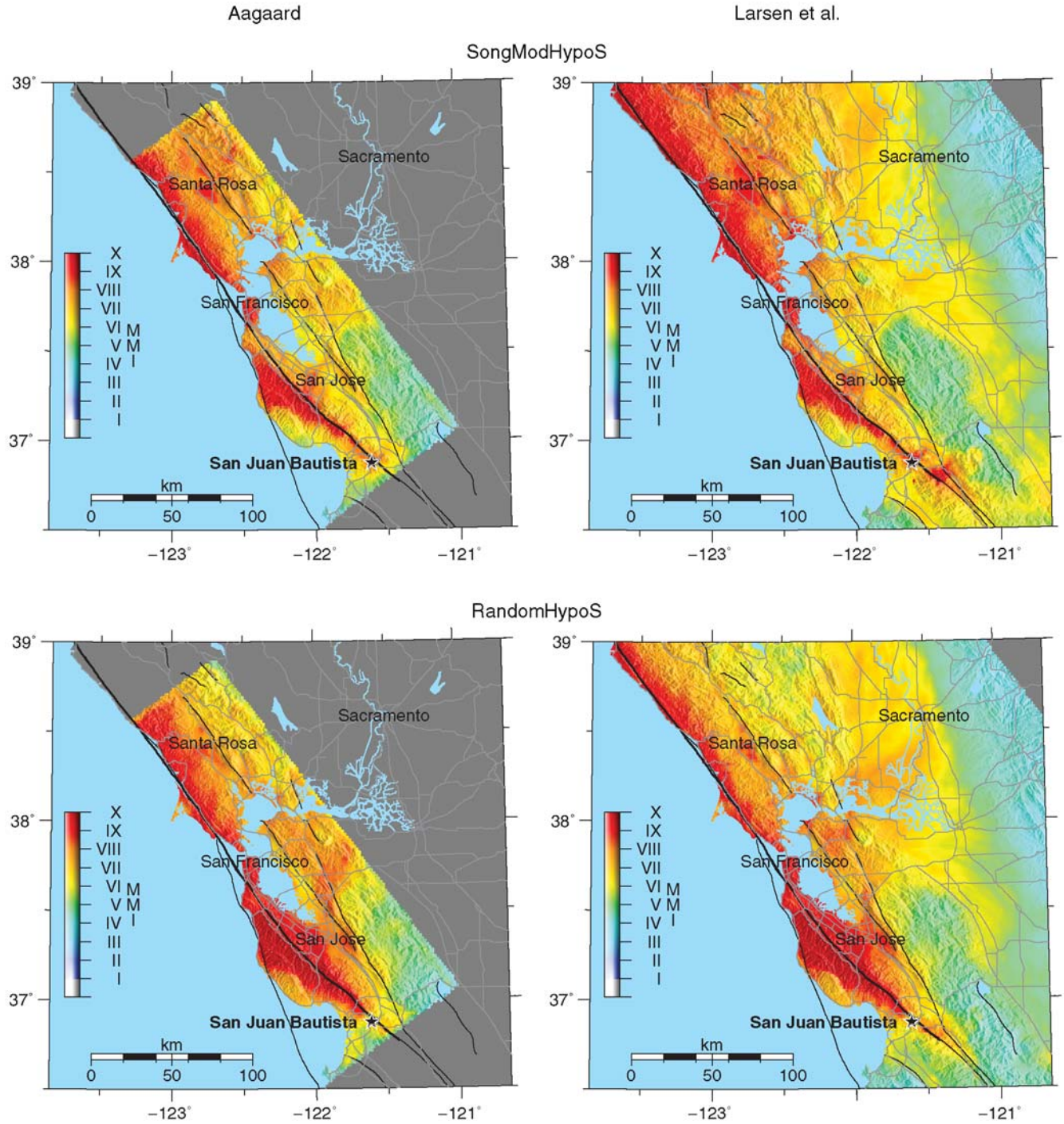

Figure 22. ShakeMaps covering the San Francisco Bay Area for Aagaard's ($T > 2.0$ sec, left) and Larsen *et al.*'s ($T > 1.0$ sec, right) SongModHypoS and RandomHypoS simulations. The thick black line delineates the rupture, and the black star identifies the epicenter. South-to-north rupture beginning near San Juan Bautista creates strong directivity towards San Francisco. The intensity of shaking along the San Francisco peninsula depends on the amount of slip in this region as illustrated by the greater intensities in RandomHypoS compared with those in SongModHypoS.

HypoN, SongModHypoC, and RandomHypoS, indicating that the local geology, in this case the western edge of the Great Valley basin, contribute to the large motions; as in the other locations, the variability in shaking cannot be attributed to the distribution of slip or hypocenter alone. The ground motions for the other scenarios are smaller, with peak velocities of about 0.1 m/sec.

Eureka sits north of the northern extent of rupture and is in the forward directivity direction for all of the northward-propagating ruptures. As a result, directivity effects control

the amplitude and duration of the waveforms at this location (site SF172, Fig. 18). For the SongMod, SongModHypoC, and SongModHypoS simulations, the ruptures begin far enough south so that the ruptures within a couple hundred kilometers of Eureka are virtually the same. That is, they all rupture toward the north with the same distribution of slip and same rupture speed. This leads to nearly identical waveforms across the three scenarios; the velocity waveforms consist of velocity pulses with peak amplitudes exceeding 1.2 m/sec and intense shaking lasting about 20 sec. Similarly, the waveforms for the RandomHypo06, RandomHypoC, and RandomHypoS simulations are nearly identical, but in this case the peak velocities are about 0.6 m/sec and the amplitudes exhibit a more pronounced decay over about 40 sec.

Intensity in Urban Area

The 1906 earthquake with a hypocenter offshore from San Francisco and a bilateral rupture directs energy away from the city of San Francisco and the most densely populated portion of the Bay Area. Consequently, in this respect it was nearly a best case scenario in terms of limiting ground shaking and damage for this major population center. The population density varies considerably over the region affected by earthquakes on the northern San Andreas fault. Some areas, such as the coastal areas north of San Francisco, are sparsely populated, whereas other areas, such as the city of San Francisco, are densely populated. Figure 4 highlights the urban areas in the nine-county (Alameda, Contra Costa, Marin, Napa, San Francisco, San Mateo, Santa Clara, Solano, and Sonoma) San Francisco Bay Area, which are home to 97% of the 7 million people living in the San Francisco Bay Area (2000 census). In order to gauge the impact of large San Andreas fault earthquakes on the current population, we want to characterize the shaking within these urban areas.

Figure 23 shows the fraction of urban area where the shaking intensity exceeds a given level, computed from Graves's simulations (the areas for the other simulations are very similar and display the same trends). The curves further to the right correspond to scenarios where the intensities are higher for a given fraction of the urban area. Note that the actual regions associated with these intensities may be different from one scenario to another. MMI values of VII and greater correspond to levels of shaking that can potentially cause moderate damage to modern structures.

SongModHypoS, with it southern epicenter near San Juan Bautista and slip from the 1906 earthquake, exposes the smallest fraction of the urban area to a given level of shaking. RandomHypo06 (random slip and 1906 epicenter) ranks next lowest, except at intensities above VIII, where it lies closer to the median. The 1906 earthquake, RandomHypoS (random slip with the San Juan Bautista epicenter), and RandomHypoC (random slip with the Bodega Bay epicenter) all yield about the same fractions of the urban area where the shaking exceeds a given level. In these three scenarios, 67%–73% of the urban area experiences an intensity of VII or greater and 22%–28% experiences an intensity of VIII or greater. SongModHypoN, SongModHypoC, and RandomHypoN cause shaking at these intensity levels over a much larger fraction of the urban area. For SongModHypoC (1906 slip and the Bodega Bay epicenter) 90% of the urban area experiences intensities of VII or greater, and more than 50% of the urban area experiences intensities of VIII or greater. Moving the epicenter further north (SongModHypoN) subjects about 25% of the urban area to intensities of IX or greater. This suggests that ruptures initiating north of San Francisco and propagating southward tend to cause the strongest shaking over the urban areas. Overall, we find that most scenarios cause stronger shaking over the San Francisco Bay urban area than the 1906 earthquake.

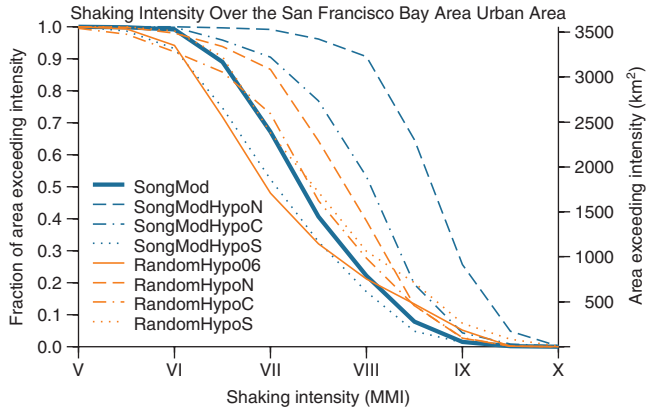

Figure 23. Comparison of fractions of the San Francisco Bay urban area exposed to given levels of shaking intensity for Graves's simulations of the 1906 earthquake (SongMod) and seven hypothetical scenarios. Many scenarios create stronger ground motions over the San Francisco Bay urban area than a repeat of the 1906 earthquake. North-to-south ruptures generate greater rupture directivity towards the urban area than south-to-north ruptures, resulting in more of the urban area experiencing higher shaking intensities.

Discussion

Our simulations reaffirm the importance of geologic structure in assessing seismic hazard in the San Francisco Bay Area. H. O. Wood (vol. I, p. 241 in Lawson, 1908) correctly correlated the character of the ground with the intensity of shaking, and H. F. Reid's analyses of the influence of basin geometry relative to the wavelength of seismic energy (vol. II, p. 56 in Reid, 1910) and of potential amplification due to internal reflections (vol. II, p. 54 in Reid, 1910) are consistent with our ground-motion simulation that yield increases in amplitude and durations of shaking associated with sedimentary basins, such as the Cupertino basin southwest of San Jose, the Livermore basin, the Cotati and Wind-

sor basins underlying Santa Rosa, and the Great Valley. The strong influence of the sedimentary basins clearly illustrates the need to better characterize the seismic velocity structure within these basins and the edges of these basins. McPhee *et al.* (2007) links strong shaking in Santa Rosa in the 1906 earthquake and two moderate earthquake in 1969 to its location along the northeastern edge of the Cotati Basin. Many studies of the 1989 Loma Prieta earthquake attributed locally strong shaking southwest of San Jose to the Cupertino basin (e.g., Frankel and Vidale, 1992; Holzer, 1994; Hartzell *et al.*, 2006), and we find the basin behaves similarly in our suite of earthquake simulations of large ruptures on the northern San Andreas fault.

Validation of the USGS 3D seismic velocity model using observations for the 1989 Loma Prieta earthquake (Aagaard *et al.*, 2008) suggests that the model is generally accurate (misfits less than 1 MMI unit) with two important exceptions. Seismic velocities assigned to the La Honda basin in the Santa Cruz Mountains and for the Great Valley Sequence, east of the Hayward fault in the Livermore–Concord area, are too low in the current velocity model, yielding intensities that are about 1–2 MMI units too high. Thus, our synthetic intensities calculated for the various 1906 rupture scenarios likely over predict the peak ground motions in these two regions. Additionally, our modeling of the 1989 Loma Prieta earthquake did not sample all parts of the model, especially north and east of the Bay Area where intensities from the 1989 earthquake were low and recordings sparse. Consequently, the uncertainty in our synthetic intensities is greater in these northern and eastern regions.

The Song simulations provide ground motions with a strict adherence to the Song *et al.* (2008) source model; however, the synthetic intensities from these simulations significantly over predict the Boatwright and Bundock intensities. On the other hand, the SongMod simulations provide a much better match to the Boatwright and Bundock intensities but include some significant deviations in the source parameters, notably a 30% reduction in the average slip. Song *et al.* (2008) combine both triangulation survey and teleseismic data to constrain the source. The quality and azimuthal coverage of the teleseismic data limit the ability of this data to constrain many of the source features. Consequently, the triangulation survey data largely control the distribution of slip. Although the average slip may be one of the more well-constrained parameters, there does appear to be some uncertainty in the average slip because the misfit in the geodetic displacements from our SongMod simulations are similar in magnitude to those from our Song simulations. The teleseismic waveforms associated with the Song *et al.* source model fit some of the recordings quite well (e.g., *SH* phase in Gottingen, Germany) but not others (e.g., *SV* phase in Puerto Rico). This suggests that, although the Song *et al.* source model may provide the best estimate of the 1906 rupture source with the currently available data, it may include some significant errors that could be contributing to our inability to match the Boatwright and Bundock intensities in the Song simulations.

In constructing the SongMod source, we significantly improve our fit to the Boatwright and Bundock intensities, which provide constraints on the synthetic intensities independent of the Song *et al.* source model. Unfortunately, there is some uncertainty associated with comparing intensities derived from our ground-motion simulations with those compiled by Boatwright and Bundock from damage reports. We use the ShakeMap PGV-to-MMI relationship (Wald *et al.*, 2005) to translate the peak velocities from our ground motions into shaking intensities. As noted earlier, there may be errors associated with applying this relation to ground motions for large events because it was developed using events up to magnitude 7.3 with very little data at peak velocities exceeding 1 m/sec (Wald *et al.*, 1999). We speculate that over prediction in the PGV-to-MMI relationship probably does not exceed 0.5 MMI units. Consequently, mean misfits in the range of 0.1–0.5 MMI units for the San Francisco Bay Area (where the seismic velocity is well constrained) for the SongMod model are likely consistent with the Boatwright and Bundock intensities, whereas mean misfits in the range of 0.4–0.8 MMI units for the Song simulation are probably not consistent.

These uncertainties associated with the Song *et al.* source model and comparing the synthetic and Boatwright and Bundock intensities suggest that we need to carefully assess the weight given to fitting the intensities versus adhering to the Song *et al.* source model. Song *et al.* argue that strain accumulation over the time span of the triangulation surveys, which would tend to decrease the observed angle changes, means the moment in their source model should be considered a lower bound. On the other hand, the triangulation surveys span intervals as long as 40 yr so the triangulation surveys potentially include afterslip and may overestimate the coseismic displacements. They also contain deformation associated with other processes as evident in the residuals for the Song simulation (Fig. 7). This raises the question of whether reducing the average slip by 30% from the Song source model in constructing the SongMod source is preferable to adjusting other source parameters. We could not produce a reasonable fit to the Boatwright and Bundock intensities by adjusting the rise time within limits compatible with empirical observations while maintaining the same magnitude and depth extent of slip as in the Song source model. Using trial and error, we were able to obtain a reasonable fit by extending the depth extent of slip to 15 km while doubling the rise time at depths greater than 12 km. We maintain the seismic moment of the Song source model with an accompanying increase in the mean misfit to the Boatwright and Bundock intensities of only 0.25 MMI units (the mean misfit in Aagaard's simulations increases from 0.08 MMI units to 0.33 MMI units). In other words, this source model provides ground motions very similar to the ones from the SongMod source model. The increased rise times at the down-dip extent of rupture could be associated

with the transition from unstable to stable sliding at the base of the seismogenic zone.

Song *et al.* (2008) chose a 12-km depth extent of rupture based on a previous study using the triangulation survey data by Matthews and Segall (1993), which constrained the slip in the 1906 earthquake near Point Arena to extend down to a depth of 15–20 km; both are equivalent because Matthews and Segall allow tapering in the depth variation of slip, whereas Song *et al.* assume uniform slip. The depth extent of seismicity varies considerably along the southern San Andreas fault (Nazareth and Hauksson, 2004). Rupture in the Loma Prieta earthquake, which occurred either on or in the immediate vicinity of the San Andreas fault, reached depths of about 16 km (Beroza, 1991; Wald *et al.*, 1991). These observations imply that the depth extent of slip at Point Arena in the 1906 earthquake might not be representative of the average depth extent over the entire rupture length. A source model that maintains a moment magnitude 7.9 event but allows the rupture to extend to a depth of 15 km with a longer rise time over this deepest portion of the rupture likely provides a better balance between matching the Boatwright and Bundock intensities and adhering to the Song *et al.* source model compared with the Song and SongMod source models. As noted in the previous paragraph, we tested such a source model, and it yields ground motions very similar to the SongMod simulations. Thus, our ground-motion modeling suggests that if the moment magnitude was closer to 7.9 than 7.8, then the rupture probably extended down to an average depth of about 15 km rather than the 12 km chosen for the Song *et al.* source model.

The average horizontal spectral accelerations from Graves's broadband ($T > 0.1$ sec) SongMod simulation generally fall within one sigma of the mean for the Campbell and Bozorgnia (2007) and Chiou and Youngs (2006) next-generation attenuation (NGA) relations. At periods less than 1.0 sec, we expect this agreement because the methodology for Graves's stochastic short-period simulations has been validated against the same data used to constrain the empirical relations from the NGA project. Both the synthetics and the two empirical relations exhibit only minor sensitivity to site conditions (V_s30 values) in this period range. This results from nonlinear effects that offset impedance amplification at high strains in the softer materials. At longer periods ($T > 1.0$ sec), the synthetics also agree with the empirical relations quite well at distances less than 10 km from the rupture for sites with V_s30 values less than 450 m/sec. The larger spectral accelerations for the synthetics at distances greater than 10 km at longer periods may be associated with the supershear rupture in our simulations of the 1906 earthquake; supershear rupture radiates significantly more energy away from the fault compared with subshear rupture. The NGA relations are constrained with very little data from both supershear ruptures and large events. At longer periods, the two empirical relations predict a greater sensitivity in horizontal spectral accelerations to the site conditions (V_s30 values) than our synthetic ground motions. The synthetic horizontal spectral accelerations are only about 25% smaller at stiffer soil sites ($V_s30 > 450$ m/sec), whereas the empirical relations predict a difference of about a factor of 2. We suspect this may be related to supershear rupture and directivity effects; however, more detailed analyses are needed to investigate the source of this difference in sensitivity and examine under what conditions and scenarios it might exist.

Kircher *et al.* (2006) estimated losses for a repeat of the 1906 San Francisco earthquake in 2006. They considered the impacts of two different ground-motion models for that earthquake, one calculated using response spectra developed from the Boatwright and Bundock (2005) ShakeMap (Boatwright *et al.*, 2006), and the other calculated using the median values of attenuation relations for a magnitude 7.9 earthquake. Because the population of the Bay Area has grown by a factor of 10 since 1906, even with modern building codes, the number of fatalities expected for a repeat of the earthquake would be comparable to those experienced in 1906 (Kircher *et al.*, 2006). The two calculations forecast property losses ranging from 90–120 billion dollars. Kircher *et al.* (2006) attribute the large property losses to the proximity of a large population to the San Andreas fault; 3.4 million residents live in the four counties lying directly along the San Andreas fault (Marin, San Francisco, San Mateo, Santa Clara).

Figure 23 indicates that the losses estimated by Kircher *et al.* (2006) may lie close to the lower bounds for large events on the San Andreas fault. Hypocenters further north with ruptures propagating southward towards the heavily urbanized San Francisco Bay tend to cause stronger shaking than the 1906 earthquake. For example, SongModHypoC with an epicenter at Bodega Bay generates shaking intensities of MMI VIII or higher over 53% of the urbanized bay area, compared to about 22% for a repeat of the 1906 earthquake. Similarly, RandomHypoS with an epicenter near San Juan Bautista and greater slip along the San Francisco peninsula than in 1906 predicts shaking intensities of MMI IX or higher over 7% of this urban area compared with just 1% for a repeat of the 1906 earthquake. The higher intensities for the limited number of hypothetical scenarios we consider suggest that a variety of large earthquakes on the northern San Andreas fault could cause greater damage compared with a repeat of the 1906 earthquake. Furthermore, any of the earthquakes in our suite of scenarios would have a severe economic impact with losses comparable to, if not exceeding, those estimated for a repeat of the 1906 earthquake.

Our simulations suggest that strong shaking in the Sacramento–San Joaquin Delta region may persist for over 60 sec, posing a hazard to the levees and other infrastructure located there. Water for two-thirds of California's population passes through the delta (California Department of Water Resources, 2006). This region, once a sea level marsh, now encompasses approximately 3000 km^2 of reclaimed land and is heavily used for agricultural purposes. Pumping since the 1800s has lowered the groundwater table and produced farmland. Subsidence associated with consolidation of sediments

and the decomposition of peat has caused much of the western and central parts of the delta to be 5–8 m below sea level. A 1800-km levee system now protects this region (California Department of Water Resources, 2006). Constructed primarily of unconsolidated sediments, the levees are susceptible to liquefaction and failure from strong ground motions. Sudden failure of one or more levees would cause immediate flooding. Depending on the severity, levee failure could paralyze California's water supply and have catastrophic economic and social consequences. Hence, it is important to assess historic and scenario ground motions in this region. The probability of an event similar to our scenario producing the strongest shaking in the delta, SongModHypoN, is relatively small. The Working Group on California Earthquake Probabilities (2003) estimated a 4.7% probability of a 1906-like event along the San Andreas fault during the 30-yr period between 2002 and 2031. This suggests that the 30-yr likelihood of a such an event initiating on the northern segment of San Andreas fault with a specific rupture model capable of producing high-amplitude ground motions in the delta is probably no greater than about one percent.

Conclusions

Using up-to-date information on the source characteristics of the 1906 earthquake and 3D geologic structure of central and northern California, our simulations of the 1906 earthquake successfully explain the variability of shaking exhibited in the Boatwright and Bundock (2005) ShakeMap. Furthermore, the ground-motion time histories across our five modeling groups portray a consistent image of how the amplitude and duration of shaking vary across the region. In San Francisco, near the epicenter, a strong double-sided fault-parallel velocity pulse with a peak magnitude of about 0.5 m/sec dominates the motion and the strong shaking lasts only about 15 sec. Rupture directivity towards Eureka, which is north of the northern end of the rupture, generates velocity pulses with peak magnitudes exceeding 1 m/sec in several of the scenarios but limits the duration of intense shaking to about 20 sec. The source characteristics combined with the complex geologic structure such as sedimentary basins leads to 30–35 sec of strong shaking in locations such as San Jose and Santa Rosa.

We also considered a set of seven scenarios to investigate the variability in shaking we might expect in future large earthquakes on the northern San Andreas fault. The suite of scenarios include variations in the hypocenter (three additional locations) and the distribution of slip and rupture speed (an additional slip model with subshear rupture). The scenarios demonstrate that in many cases the ground motions in the San Francisco Bay urban area would be more intense than what was experienced in the 1906 earthquake, implying significant higher losses than the 90–120 billion dollars estimated by Kircher *et al.* (2006) for a repeat of the 1906 earthquake. For the cases of a north-to-south rupture with the same slip as the 1906 event, over 50% of the San Francisco Bay urban area experiences a shaking intensity of at least MMI VIII, compared with about 20% for a repeat of the 1906 earthquake. The north-to-south ruptures also expose the levees in the delta of the Sacramento–San Joaquin rivers to stronger shaking with durations longer than 60 sec.

Our simulations show that in order to accurately characterize the seismic hazard in the San Francisco Bay region, we need to account for both the complex 3D geologic structure and variations in earthquake source characteristics, such as the hypocenter, rupture speed, and distribution of slip. This study and our study of the Loma Prieta earthquake (Aagaard *et al.*, 2008) demonstrate that we have the principal tools necessary for such an analysis in the form of current computational resources and the 3D geologic and seismic velocity models. Thus, we are in a position to use 3D simulations to more accurately characterize the seismic hazard in the San Francisco Bay Area at periods greater than 1.0 sec by developing suites of scenarios based on the earthquake probabilities for 2002–2031 (Working Group on California Earthquake Probabilities, 2003) and future updates to the probability forecast.

Acknowledgments

David Wald and John Boatwright provided many helpful comments and suggestions over the course of this study. We thank Howard Bundock for generating preliminary plots of shaking intensities using ShakeMap that facilitated comparisons among the simulations. Seok Goo Song, Greg Beroza, and Paul Segall generously responded to our questions and concerns about their source model for the 1906 earthquake. Reviews by Tom Hanks, Larry Hutchings, Jeanne Hardebeck, and Martin Mai led to significant improvements in the manuscript. Larry Baker provided technical support for Aagaard's simulations using the USGS Menlo Park Beowulf cluster. Aagaard and Harmsen *et al.* were funded by the Earthquake Hazard Program of the U.S. Geological Survey. Graves was supported by funding from the USGS External Grants Program (06HQGR0132) and the Southern California Earthquake Center (SCEC). The SCEC is funded by National Science Foundation Cooperative Agreement EAR-0106924 and USGS Cooperative Agreement 02HQAG0008. The Graves simulations were run at the University of Southern California's Center for High Performance Computing and Communications (www.usc.edu/hpcc, last accessed February 2008). Larsen's and Petersson *et al.*'s work was performed in part under the auspices of the U.S. Department of Energy by University of California, Lawrence Livermore National Laboratory (LLNL) under Contract Number W-7405 -Eng-48. This is LLNL Contribution Number UCRL-JRNL-228005. Many of the figures were generated using Generic Mapping Tools (Wessel and Smith, 1998) and low-pass filtering of the waveforms was performed using SAC2000 (Goldstein *et al.*, 2003).

References

Aagaard, B. T., and T. H. Heaton (2004). Near-source ground motions from simulations of sustained intersonic and supersonic fault rupture, *Bull. Seismol. Soc. Am.* **94,** no. 6, 2064–2078.

Aagaard, B. T., T. M. Brocher, D. Dolenc, D. Dreger, R. W. Graves, S. Harmsen, S. Hartzell, S. Larsen, and M. L. Zoback (2008). Ground-motion modeling of the 1906 San Francisco earthquake, part I: Valida-

tion using the 1989 Loma Prieta earthquake, *Bull. Seismol. Soc. Am.* **98,** no. 2, 989–1011.

Aagaard, B. T., J. F. Hall, and T. H. Heaton (2001). Characterization of near-source ground motions with earthquake simulations, *Earthq. Spectra* **17,** no. 2, 177–207.

Anooshehpoor, A., T. H. Heaton, B. P. Shi, and J. N. Brune (1999). Estimates of the ground accelerations at Point Reyes station during the 1906 San Francisco earthquake, *Bull. Seismol. Soc. Am.* **89,** no. 4, 845–853.

Beresnev, I., and G. Atkinson (2001). Subevent structure of large earthquakes: a ground-motion perspective, *Geophy. Res. Lett.* **28,** no. 1, 53–56.

Beroza, G. C. (1991). Near-source modeling of the Loma Prieta earthquake: evidence for heterogeneous slip and implications for earthquake hazard, *Bull. Seismol. Soc. Am.* **81,** no. 5, 1603–1621.

Boatwright, J., and H. Bundock (2005). Modified Mercalli intensity maps for the 1906 San Francisco earthquake plotted in ShakeMap format, *U.S. Geol. Surv. Open-File Rept. 2005-1135*, available at http://pubs.usgs.gov/of/2005/1135/ (last accessed February 2008).

Boatwright, J., and H. Bundock (2008). The distribution of modified Mercalli intensity in the 18 April 1906 San Francisco earthquake, *Bull. Seismol. Soc. Am.* **98,** no. 2, 890–900.

Boatwright, J., H. Bundock, and L. C. Seekins (2006). Using modified Mercalli intensities to estimate acceleration response spectra for the 1906 San Francisco earthquake, *Earthq. Spectra* **22,** (special issue II), S279–S295.

Bolt, B. A. (1968). The focus of the 1906 California earthquake, *Bull. Seismol. Soc. Am.* **58,** no. 1, 457–471.

Boore, D. M. (1977). Strong-motion recordings of the California earthquake of April 18, 1906, *Bull. Seismol. Soc. Am.* **67,** no. 3, 561–577.

Borcherdt, R. D., and J. F. Gibbs (1976). Effects of local geological conditions in the San Francisco Bay region on ground motions and the intensities of the 1906 earthquake, *Bull. Seismol. Soc. Am.* **66,** no. 2, 467–500.

Brocher, T. M. (2005). Empirical relations between elastic wavespeeds and density in the Earth's crust, *Bull. Seismol. Soc. Am.* **95,** no. 6, 2081–2092.

Brocher, T. M. (2008). Compressional and shear-wave velocity versus depth relations for common rock types in Northern California, *Bull. Seismol. Soc. Am.* **98,** no. 2, 950–968.

Brune, J. N. (1970). Tectonic stress and spectra of seismic shear waves from earthquakes, *J. Geophys. Res.* **75,** 4997–5009.

California Department of Water Resources (2006). Delta facts (fact sheet), available at www.publicaffairs.water.ca.gov/newsreleases/2006/delta/factsheet.pdf (last accessed February 2008).

Campbell, K. W., and Y. Bozorgnia (2007). Tech. Rept. 2007/02, Campbell-Bozorgnia NGA ground motion relations for the geometric mean horizontal component of peak and spectral ground motion parameters, Pacific Earthquake Engineering Research Center, University of California, Berkeley, California.

Chiou, B. S. J., and R. R. Youngs (2006). Interim report for USGS review, Chiou and Youngs PEER-NGA empirical ground motion model for the average horizontal component of peak acceleration and pseudo-spectral acceleration for spectral periods of 0.01 to 10 seconds, Pacific Earthquake Engineering Research Center, University of California, Berkeley, California.

Day, S. M. (1982). Three-dimensional simulation of spontaneous rupture: the effect of nonuniform prestress, *Bull. Seismol. Soc. Am.* **72,** no. 6, 1881–1902.

Frankel, A., and J. Vidale (1992). A three-dimensional simulation of seismic waves in the Santa Clara Valley, California, from a Loma Prieta aftershock, *Bull. Seismol. Soc. Am.* **82,** no. 5, 2045–2074.

Goldstein, P., M. Dodge, D. Firpo, and L. Minner (2003). Signal processing and analysis tools for seismologists and engineers, in *The IASPEI International Handbook of Earthquake and Engineering Seismology*, Academic Press, London.

Graves, R. W. (1996). Simulating seismic-wave propagation in 3-D elastic media using staggered-grid finite-differences, *Bull. Seismol. Soc. Am.* **86,** no. 4, 1091–1106.

Graves, R. W., and A. Pitarka (2004). Broadband time history simulation using a hybrid approach, in *13th World Conference on Earthquake Engineering Conference Proceedings*, Vancouver, Canada, 1–6 August, paper no. 1098.

Guatteri, M. P., M. Mai, G. C. Beroza, and J. L. Boatwright (2003). Strong ground-motion prediction from stochastic-dynamic source models, *Bull. Seismol. Soc. Am.* **93,** no. 1, 301–313.

Hartzell, S., S. Harmsen, R. A. Williams, D. Carver, A. Frankel, G. Choy, R. C. Jachens, T. M. Brocher, and C. M. Wentworth (2006). Modeling and validation of a 3D velocity structure for the Santa Clara Valley, California, for seismic-wave simulations, *Bull. Seismol. Soc. Am.* **96,** no. 5, 1851–1881.

Hisada, Y. (2001). A theoretical omega-square model considering spatial variation in slip and rupture velocity, part II: Case for a two-dimensional source model, *Bull. Seismol. Soc. Am.* **91,** no. 4, 651–666.

Holzer, T. H. (1994). Loma Prieta earthquake professional papers, strong ground motion and ground failure, *U.S. Geol. Surv. Profess. Pap. 1551*, available at http://pubs.usgs.gov/pp/pp1551/ (last accessed February 2008).

Jachens, R., R. Simpson, R. Graymer, C. Wentworth, and T. Brocher (2006). Three-dimensional geologic map of northern and central California: a basin model for supporting earthquake simulations and other predictive modeling (abstract), *Seism. Res. Lett.* **77,** no. 2, 270.

Kagawa, T., K. Irikira, and P. G. Somerville (2004). Differences in ground motion and fault rupture process between the surface and buried rupture earthquakes, *Earth Planets Space* **56,** no. 1, 3–14.

Kircher, C. A., H. A. Seligson, J. Bouabid, and G. C. Morrow (2006). When the Big One strikes again: estimated losses due to a repeat of the 1906 San Francisco earthquake, *Earthq. Spectra* **22,** (Special Issue II), S297–S339.

Larsen, S., and C. A. Schultz (1995). Tech. Rept. UCRL-MA-121792, Elas3d: 2D/3D elastic finite-difference wave propagation code, Lawrence Livermore National Laboratory, 19 pp.

Lawson, A. (Editor) (1908). *The California earthquake of April 18, 1906: Report of the State Earthquake Investigation Commission*, Carnegie Institution of Washington, Washington, D.C..

Liu, P., and R. J. Archuleta (2002). The effect of a low-velocity surface layer on simulated ground motion (abstract), *Seism. Res. Lett.* **73,** no. 2, 267.

Lomax, A. (2005). A reanalysis of the hypocentral location and related observations for the great 1906 California earthquake, *Bull. Seismol. Soc. Am.* **95,** no. 3, 861–877.

Mai, P. M., and G. C. Beroza (2002). A spatial random field model to characterize complexity in earthquake slip, *J. Geophys. Res.* **107,** no. B11, 2308, doi 10.1029/2001JB000588.

Matthews, M. V., and P. Segall (1993). Statistical inversion of crustal deformation data and estimation of the depth distribution of slip in the 1906 earthquake, *J. Geophys. Res.* **98,** 12,153–12,163.

McPhee, D. K., V. E. Langenheim, S. Hartzell, R. J. McLaughlin, B. T. Aagaard, R. C. Jachens, and C. McCabe (2007). Basin structure beneath the Santa Rosa Plain, northern California: implications for damage caused by the 1969 Santa Rosa and 1906 San Francisco earthquakes, *Bull. Seismol. Soc. Am.* **97,** 1449–1457.

Nazareth, J. J., and E. Hauksson (2004). The seismogenic thickness of the southern California crust, *Bull. Seismol. Soc. Am.* **94,** no. 3, 940–960.

Nilsson, S., N. A. Petersson, B. Sjögreen, and H. O. Kreiss (2007). Stable difference approximations for the elastic wave equation in second order formulation, *SIAM J. Numer. Anal.* **45,** no. 5, 1902–1936.

Piatanesi, A., E. Tinti, M. Cocco, and E. Fukuyama (2004). The dependence of traction evolution on the earthquake source time function adopted in kinematic rupture models, *Geophys. Res. Lett.* **31,** L04609, doi 10.1029/2003GL019225.

Reid, H. (Editor) (1910). The mechanics of the earthquake, in *The California Earthquake of April 18, 1906: Report of the State Earthquake Investigation Commission*, Vol. **2**, Carnegie Institution of Washington, Washington, D.C..

Somerville, P. G. (2003). Magnitude scaling of the near fault rupture directivity pulse, *Phys. Earth Planet. Interiors* **137,** no. 1–4, 201–212.

Somerville, P. G., K. Irikura, R. Graves, S. Sawada, D. Wald, N. Abrahamson, Y. Iwasaki, T. Kagawa, N. Smith, and A. Kowada (1999). Characterizing crustal earthquake slip models for the prediction of strong ground motion, *Seism. Res. Lett.* **70,** no. 1, 199–222.

Song, S., G. C. Beroza, and P. Segall (2008). A unified source model for the 1906 San Francisco earthquake, *Bull. Seismol. Soc. Am.* **98,** no. 2, 823–831.

Thatcher, W., M. Grant, and M. Lisowski (1997). Resolution of fault slip along the 470-km-long rupture of the great 1906 San Francisco earthquake and its implications, *J. Geophys. Res. Solid Earth* **102,** no. B3, 5353–5368.

Wald, D. J., D. V. Helmberger, and T. H. Heaton (1991). Rupture model of the 1989 Loma Prieta earthquake from the inversion of strong-motion and broadband teleseismic data, *Bull. Seismol. Soc. Am.* **81,** no. 5, 1540–1572.

Wald, D. J., H. Kanamori, D. V. Helmberger, and T. H. Heaton (1993). Source study of the 1906 San Francisco earthquake, *Bull. Seismol. Soc. Am.* **83,** no. 4, 981–1019.

Wald, D. J., V. Quitoriano, T. H. Heaton, H. Kanamori, C. W. Scrivner, and C. B. Worden (1999). TriNet "ShakeMaps": rapid generation of instrumental ground motion and intensity maps for earthquakes in southern California, *Earthq. Spectra* **15,** no. 3, 537–556.

Wald, D., B. Worden, V. Quitoriano, and K. Pankow (2005). ShakeMap manual: technical manual, users guide, and software guide (Version 1.0). U. S. Geol. Surv., available at http://pubs.usgs.gov/tm/2005/12A01/ (last accessed February 2008).

Ward, S. N. (2000). San Francisco Bay Area earthquake simulations: a step toward a standard physical earthquake model, *Bull. Seismol. Soc. Am.* **90,** no. 2, 370–386.

Wentworth, C. M., G. R. Fisher, P. Levine, and R. C. Jachens (1995). The surface of crystalline basement, Great Valley and Sierra Nevada, California: a digital map database, *U.S. Geol. Surv. Open-File Rept. 95-96*.

Wessel, P., and W. H. F. Smith (1998). New, improved version of the Generic Mapping Tools released, *EOS* **79,** 579.

Wills, C. J., M. Petersen, W. A. Bryant, M. Reichle, G. J. Saucedo, S. Tan, G. Taylor, and J. Treiman (2000). A site-conditions map for California based on geology and shear-wave velocity, *Bull. Seismol. Soc. Am.* **90,** no. 6B, S187–S208.

Working Group on California Earthquake Probabilities (2003). Earthquake probabilities in the San Francisco Bay region: 2002–2031, *U.S. Geol. Surv. Open-File Rept. 03-214*.

Yaji, Y. (2004). Source rupture process of the 2003 Tokachi-Oki earthquake determined by joint inversion of teleseismic body wave and strong ground motion data, *Earth Planets Space* **56,** 311–316.

Zoback, M. L. (2006). The 1906 earthquake and a century of progress in understanding earthquakes and their hazards, *GSA Today* **16,** 4–11.

U.S. Geological Survey
MS977, 345 Middlefield Rd.
Menlo Park, California 94025
(B.T.A., T.M.B., M.L.Z.)

Seismological Laboratory
University of California, Berkeley
215 McCone Hall
Berkeley, California 94720
(D.D., D.D.)

URS Corporation
566 El Dorado St.
Pasadena, California 91101
(R.W.G.)

U.S. Geological Survey
MS966, P.O. Box 25046
Golden, Colorado 80225
(S.H., S.H.)

Lawrence Livermore National Laboratory
Box 808, L-103
Livermore, California 94551-0808
(S.L.)

Computer Applications and Research Department, Computations Directorate
Lawrence Livermore National Laboratory
Box 808, L-550
Livermore, California 94551-0808
(K.M.)

Center for Applied Scientific Computing, Computations Directorate
Lawrence Livermore National Laboratory
Box 808, L-550
Livermore, California 94551-0808
(S.N., N.A.P., B.S.)

Atmospheric, Earth and Energy Department, Energy and Environment Directorate
Lawrence Livermore National Laboratory
Box 808, L-205
Livermore, California 94551-0808
(A.R.)

Manuscript received 12 March 2007